TIME-RESOLVED AND THREE-DIMENSIONAL STUDY OF DISLOCATION-PARTICLE INTERACTIONS IN ALUMINUM AND COPPER ALLOYS

BY

GRACE LIU

DISSERTATION

Submitted in partial fulfillment of the requirements
for the degree of Doctor of Philosophy in Materials Science and Engineering
in the Graduate College of the
University of Illinois at Urbana-Champaign, 2011

Urbana, Illinois

Doctoral Committee:

Professor Ian McLean Robertson, Chair
Professor Pascal Bellon
Professor Jian-Min Zuo
Professor Duane Douglas Johnson

ABSTRACT

Dislocation-particle interactions in three alloys systems, Al-Cu, Al-Mg-Sc, and Cu-Co have been investigated using *in situ* straining experiments inside the transmission electron microscope, *post mortem* analysis, and electron tomographic reconstructions. Specifically, diffraction-contrast electron tomography was developed during the course of this work as a 3D imaging technique for crystalline systems such that the dislocation and defect arrangement could be fully characterized and spatially-resolved. Micrographs imaged using two-beam and kinematical bright-field and weak-beam dark-field conditions were acquired over an angular range then used to reconstruct the tomograms. Supplemental advances to the technique include: Visualization of dislocations in color based on Burgers vector or other relevant characteristics; determination of the specimen coordinate system in the tomogram; and overcoming the $\mathbf{g} \cdot \mathbf{b}$ invisibility condition by dual-axes tomography.

In the Al-Cu system, which contained Al_2Cu plate-shaped particles residing on $\{001\}_{Al}$ habit planes, *in situ* straining experiments revealed glide of lattice dislocations in the coherent side of the particle-matrix interface. The confined dislocations escaped the interface by cross-slip after reaching one end of the Al_2Cu plate or by shearing the particle, as observed during *post mortem* analysis. Dislocations bypassed the particles by shear at multiple locations along their length, suggesting that a shearing site becomes more unfavorable with each dislocation passage such that adjacent slip systems must be activated in order to continue shear. When highly deformed, the inter-particle region was shown by electron tomography to be populated with a complex configuration of lattice dislocations pinned at both ends on a particle interface as well as debris created from dislocation-

dislocation interactions.

In the Cu-Co system, semicoherent Co-rich octahedral particles normally unshearble by lattice dislocations were observed to be sheared by small twins emanating from the Cu matrix. This new deformation behavior was attributed to the high strain rates associated with twinning and a small increase in interfacial energy associated with shearing of Co particles, which has the same stacking as the Cu matrix. Interactions with lattice dislocations, on the other hand, exhibited similar behavior during *in situ* and *post mortem* observations as the Al-Mg-Sc system, which contained Al_3Sc particles. In the semi-coherent regime, between 40 nm and up to around 200 nm for Al_3Sc and 100 nm for Co, an initial elastic interaction from the misfit strain field gave way to a novel bypass mechanism involving the creation of half-loops attached on one side to the particle interface via bowing and cross-slip while locally pinned at on the particle interface. Bypass of such a particle also involved interfacial dislocations, which increased the complexity of the particle-matrix interface and impeded subsequent bypass of the same particle. In all cases, multiple interactions with lattice dislocations resulted in the evolution of defect structures around a particle over time and the interactions examined were more complex than single dislocation-single particle interactions depicted in classical theoretical models.

To M.C. and C.F., who have provided both
good humor and unwavering support

ACKNOWLEDGEMENTS

I am extremely grateful to my advisor, Professor Ian Robertson, for his guidance, support, and wisdom. It has been an absolute privilege working with you—I have learned invaluable lessons in research as well as in life. Thank you.

It is also my distinct pleasure to acknowledge Professor Pascal Bellon, Professor Jim Zuo, Professor Duane D. Johnson and Professor Carl Altstetter for serving on my preliminary and doctoral committees. I truly appreciate all your comments, input and discussions.

I am indebted to my colleagues in the IMR Group, past and present, who have helped me in countless ways throughout my graduate career. The group activities and outings were especially memorable. Thanks, everyone!

Thanks are also due to the staff at the Center for Microanalysis of Materials, Frederick Seitz Materials Research Laboratory, for the many hours of toil to keep the instruments up and running; and for putting up with my many requests.

In addition, I owe my gratitude to my family, who has served as a foundation in everything I do; and to my parents-in-law, who have shown me great kindness and made me feel welcome. And finally, I am sincerely grateful to my best friend and husband, Willie Wu, who has been a source of great encouragement and support. I couldn't have done it without you.

TABLE OF CONTENTS

CHAPTER 1

INTRODUCTION

Precipitates or second phase particles serve as a primary source of strengthening for many engineering alloys by acting as barriers to mobile lattice dislocations. Plasticity, and therefore the mechanical properties of these materials can be closely correlated with the interaction between dislocations and the precipitates. However, as previous theoretical, simulation, as well as experimental results suggest, there exists an extensive range of bypass mechanisms from which matrix dislocations can select in order to overcome these obstacles. Although a plethora of mechanisms have been proposed, not all have been verified by experimental observation. An additional motivation lies in the development of predictive creep and particle-strengthening models, which have the potential to greatly expedite the time to market of high-performance alloys subjected to extreme operating environments. In order to provide physically-based inputs for these models, details of the fundamental processes occurring during dislocation-particle interactions must be identified and understood.

One difficulty that has persistently hindered a straightforward interpretation of experimental data for dislocation-particle interactions lies in the limitations of a conventional transmission electron micrograph: Its static nature precludes time-resolved observation of the interactions. And because a micrograph is a two-dimensional projection of the imaged volume, depth information is lost. To overcome these challenges, the present study investigates dislocation-particle interactions in three alloy systems possessing distinct particles by using (1) *in situ* straining experiments to capture the dynamics of the

interactions; (2) *post mortem* analyses to characterize the microstructure; and (3) a novel application of electron tomography to recover spatial-resolution of the interactions. By combining these approaches, both the evolution and three-dimensional arrangement of the microstructure can be obtained, granting new insights into the mechanisms of dislocation-particle interactions.

CHAPTER 2

BACKGROUND

The field of particle-strengthening alloys is both vast and historical. This chapter will first review the topics and knowledge relevant to the study of dislocation-particle interactions in terms of theory, experimental observations, and computer modeling. Secondly, the principles of tomographic reconstructions will be examined in the context of diffraction-contrast electron tomography, which has been an integral technique in this study. Together, these topics underscore the importance of continued research in the behavior of particle-strengthened materials by using existing, as well as new, techniques in order to further our understanding of these materials.

2.1 Particle Strengthened Alloys

Many engineering alloys contain metals such as aluminum, iron, copper, chromium, magnesium, nickel, titanium…etc. in specific compositions in order to produce the desired physical properties. Aluminum and copper are among the most useful, serving as the base metal for a large number of engineering alloys. The abundance of aluminum coupled with the characteristics of aluminum alloys such as their low weight, high degree of strengthening, corrosion resistance, and electrical and thermal conductivity render them one of the most versatile engineering materials with applications in aerospace, automotive, sports and marine equipment…etc. [1-2]. For aerospace alloys, the addition of Sc to aluminum is particularly important due to the formation of an equilibrium thermally stable $L1_2$ phase (Al_3Sc) which functions as a potent strengthener by grain boundary pinning and

facilitates the manufacturing of ultra fine-grained aluminum alloys [3-4]. Common additions to aluminum such as copper constitute a unique alloy series; for example, Al-Cu-based alloys are designated the 2xxx series and Al-Zn-based alloys are designated the 7xxx series.

Copper alloys, on the other hand, often contain zinc (brasses), lead, tin (bronzes), nickel…etc. and are prized for qualities such as electrical conductivity, ductility and solderability. Applications of copper alloys are extensive, including casings, hardware, electrical and construction equipment…etc. Several standards of copper alloy nomenclature exist, with the UNS (unified numbering system) being the most widely accepted in North America; for example, C1xxxx-C4xxxx for brasses, C5xxxx for bronzes, and C7xxxx for nickel silvers [1]. Since many of these aluminum and copper alloys derive their mechanical properties from strengthening with a dispersion of particles, further understanding the fundamental processes operating during dislocation-particle interactions can lead to physically-based material inputs for improving the accuracy of alloy models.

2.2 Theory of Particle Strengthening

Particle strengthening has been used historically in many alloy systems and achieves strengthening by the presence of a dispersion of obstacles to dislocation movement. These obstacles come about through a second phase precipitation process involving additive elements and the matrix or between multiple additive elements. For example, the δ phase (Al_3Li) in an Al-Li alloy and the γ phase ($Ni_3(Al, Ti, Nb)$) in a Ni superalloy [1]. The degree of strengthening obtained is dependent on a number of factors such as the metallic system involved, the volume fraction, size and shape of the particles,

and the nature of the interface between the particles and the matrix [5-6]. These interfaces are generally described as being coherent, semi-coherent, or incoherent. Fig. 2.1 shows a schematic of each type of interface with the matrix lattice on the left, and the particle lattice on the right. For a coherent interface, Fig. 2.1(a), the atomic planes are continuous across the interfacial plane. In general, small particles forming from a supersaturated solid solution are expected to have this type of interface since the difference in lattice parameter between the particle phase and the matrix can be accommodated by lattice distortions, which in turn causes coherency strain around the particle [7]. For a particle phase which has a lattice parameter close to that of the matrix, the particle coherency can be maintained up to larger particle sizes and the total interfacial energy is small, approximately 0 to 200 mJ/m^2 [8]. A semi-coherent interface, Fig. 2.1(b), is associated with particles that have grown larger in size such that lattice distortions alone cannot accommodate the misfit between the particle phase and the matrix. For isotropic precipitates, i.e. spherical in shape, the distribution of misfit dislocations in the interface is relatively homogenous; but for particles of an anisotropic geometry such as elongated plates, misfit dislocations can be preferentially located at high-growth rate interfaces. As the misfit strain increases, the spacing between interfacial dislocations decreases up to approximately $\varepsilon \approx 0.25$ with interfacial energy in the range of roughly 200 to 500 mJ/m^2 [6, 8]. An incoherent interface, Fig. 2.1(c), corresponds to non-continuous atomic planes between the matrix and the particle phase and is associated with large particles beyond a critical size or with particles introduced by methods such as metal powder oxide dispersion strengthening [9]. The lattice parameters in each corresponding atomic plane may differ by more than 25% and the interfacial energy ranges ~500 to 1000 mJ/m^2 [8].

Additionally, the interaction between dislocations and particles can be influenced by the temperature. In the following sections, the mechanisms commonly understood to operate for elevated temperatures and low (including room) temperatures will be described. While previous experimental and computer simulations work for low temperature interactions will be addressed in detail in Sections 2.3 and 2.4, the review for high-temperature interactions will be more succinctly summarized since the results in this thesis are primarily concerned with room-temperature interactions.

2.2.1 At Elevated Temperatures

At elevated temperatures, the increased diffusion rate of vacancies enables an edge dislocation to move out of its slip plane by a process known as climb. Although room-temperature climb has been reported for special cases (e.g., along nanolayered interfaces) at room temperature [10-11], climb and other diffusion-controlled processes are usually only activated at temperatures greater than half the melting point of the material. Fig. 2.2 presents a schematic of (positive) climb where a vacancy (broken circle) diffuses to the extra half-plane, Fig. 2.2(a), and is absorbed into the dislocation core, moving the dislocation up one plane. Conversely, negative climb occurs when a vacancy is emitted by the dislocation core and the dislocation moves down one plane, Fig. 2.2(b) [6, 12]. The ability of a dislocation to bypass a particle via climb at elevated temperatures has historically been closely associated with progressive deformation under a constant stress, known as creep. Fig. 2.3 shows an example of steady-state creep, which operates predominantly at high temperatures, for aluminum under a stress of 2.07×10^7 Pa at different temperatures (424 K, 478 K, and 531 K) by plotting the creep strain against the

temperature-compensated time parameter θ, defined as

$$\theta = te^{-\Delta H/RT} \qquad \text{(Eqn. 2.1.)}$$

where t is the time of creep exposure. The overlapping of data points from different temperatures onto one curve was interpreted to mean that a single rate-controlling step predominates at all three temperatures—in this case by the process of dislocation climb [13].

Subsequently, however, three different models were proposed to either modify or replace the purely climb-controlled creep behavior predicted previously. Figure 2.4 shows schematically the rate-limiting bypass steps in each of these models: (a) detachment-controlled, (b) dissociation-controlled, and (c) (modified) climb-controlled. In all three cases, dislocations are depicted to be moving from left to right. The first of these, detachment-controlled creep, was developed to account for departure-side pinning of dislocations as they bypass an incoherent dispersion of particles, Fig. 2.4(a) ①-③. The model assumes an attractive interaction between the dislocation and the particle and only the rate-controlling step of thermally-assisted dislocation detachment is considered [14]. The dissociation-controlled creep model (Fig. 2.4(b)), on the other hand, proposes the dissociation of lattice dislocations into interfacial dislocations as the rate-controlling step during bypass. The dissociation reaction is analogous to dislocations interacting with a grain boundary and has a corresponding threshold stress dependent on the particle size, the inter-particle spacing and the type of dissociation taking place [15]. Lastly, the modified climb-controlled creep model, Fig. 2.4(c), was developed for the bypass of coherent particles where dislocation climb rather than detachment was assumed to be the rate-

limiting step. The model incorporates elastic interaction by using modulus and lattice mismatch to derive the rate of climb [16]. However, when calculated values based on these three models are compared with experimental data, there appears to be only limited agreement in the trend but not in the magnitude or creep rate (as a function of applied stress) [17]. The disagreement between the predicted creep behavior and that obtained experimentally highlights the lack of a comprehensive theoretical model that is capable of accurately capturing dislocation-particle interactions at elevated temperatures.

2.2.2 At Room Temperature

Without thermal activation, dislocation climb is not expected to operate during low and room temperature interactions. For particles of sufficiently small size and high coherency, a lattice dislocation stays on its original slip plane and enters the particle, creating a new interface by displacing particle above the slip plane by |**b**|, as shown schematically in Fig. 2.5. The newly created interface has an associated interfacial energy that is dependent on the crystal structure and relative orientation of the matrix with the particle phase; and when the dislocation exits the particle on the other side, an additional interface is created with total new area = $2\pi r\boldsymbol{b}$ where r is the particle radius. The extra work that the lattice dislocation does while cutting the particle is referred to as chemical strengthening and contributes to an increase in the flow stress by

$$\tau_{chem} = 2G\left(\frac{\gamma_s}{Gr}\right)^{\frac{3}{2}}\left(\frac{fr}{\boldsymbol{b}}\right)^{\frac{1}{2}} \qquad \text{(Eqn. 2.2)}$$

where γ_s is the interface surface energy, G is the shear modulus, and f is the volume fraction of particles [5, 7].

When the matrix and particle have different lattice stacking, however, the shearing of particles also creates a layer of atoms whose stacking is shifted by the glide of the lattice dislocation through the particle and is known as order strengthening. For example, the shearing of the precipitate phase Al_3Sc, which has a $L1_2$ crystal structure, creates such a miss-stacking in an Al-Mg-Sc alloy, which has a face-centered cubic crystal structure [18]. The schematic in Fig. 2.6(a) shows the creation of an antiphase boundary (APB) inside the particle with original stacking "ABABAB..." by the passage of a dislocation. The atomic bonds between "A" and "B" atoms are now "A-A" or "B-B," which are higher-energy configurations and collectively constitute the antiphase boundary energy γ_{APB}. The increase in flow stress in this case is

$$\tau_{ord} \cong 0.7G\left(\frac{\gamma_{APB}}{G\boldsymbol{b}}\right)^{\frac{3}{2}}\left(\frac{fr}{\boldsymbol{b}}\right)^{\frac{1}{2}} \qquad \text{(Eqn. 2.3).}$$

Note that in this case, only the early stages of precipitation are considered since at latter stages, particle shearing becomes less likely due to the larger volume that a lattice dislocation must penetrate [7]. Particle-shearing can also be accompanied by a different type of miss-stacking in the slip plane, Fig. 2.6(b), which shows the dissociation of a perfect lattice dislocation "BC" on the (111) plane followed by shearing of the particle to create a superlattice (intrinsic or extrinsic) stacking-fault. Proposed mechanisms of the particle-shearing include Shockley superpartial dislocations forming from dissociation inside the particle (and spanning a superlattice stacking-fault), the interaction of two perfect dislocations at the particle-matrix interface, and the sweeping up of a previously-formed APB by a Shockley dislocation loop through expansion [7, 19-21]. Unless the average particle size is very small and the volume fraction is large, in terms of the efficacy of

strengthening both chemical and order strengthening are expected to be less effective than that from impenetrable particles.

The earliest studies which sought to build a theoretical model for particle strengthening in metal alloys were those by Mott & Nabarro and Orowan [22-24] in the 1940's. Of these, Orowan considered the case of non-deformable particles and postulated the formation of residual dislocation loops around the particles [5-6, 25], which is presented schematically in Fig. 2.8(a). The dislocation bows between obstacles, then the interaction force between the bowing segments causes them to come together to create a loop around the obstacle and the line dislocation can continue to glide. A second dislocation in an identical slip system will experience the combined effect of the loop and the particle. Although multiple loops can form, this bypass process must be limited to low stresses. The bowing of dislocations around the particles gives rise to an increase in the flow stress by

$$\tau_B \cong \frac{G\boldsymbol{b}}{(L-2r)} \qquad \text{(Eqn. 2.4)}$$

where L is the average inter-particle distance (measured center-to-center) [26-27]. If another lattice dislocation on the slip plane were to bypass the same particle, the effective particle radius (now with an Orowan loop around it) would be larger than it was initially; and bypass must occur by multiple-Orowan looping to form concentric loops around the particle but cannot be sustained beyond a few of such loops [28-29].

Although climb is not feasible, lattice dislocations moving at room temperature can change slip planes by cross-slip of screw-character segments. This is illustrated schematically for the face-centered cubic lattice in Fig. 2.7, where a dislocation with a Burgers vector **b** resides on the (111) plane (Fig. 2.7(a)). The screw segment where the

line direction is parallel to the Burgers vector, "S," then cross-slips onto the conjugate plane, $(1\bar{1}1)$, as shown in Fig. 2.7(b)-(c). Further expanding the slipped region, the dislocation double cross-slips back onto a parallel (111) plane, Fig. 2.7(c)-(d). Known as the Hirsch mechanism [30], a lattice dislocation may bypass a particle by cross-slip in a similar fashion. Fig. 2.8(b) shows how an edge dislocation can bow around a particle, acquiring screw character before (double) cross-slip of these segments self-annihilate to leave behind an interstitial prismatic loop and a jog on the original line dislocation. Fig. 2.8(c) shows how a comparable bypass process takes place for a pure screw dislocation—the initial location of cross-slip behind the particle results in the creation of two prismatic loops on the side of the particle and the original dislocation line contains no jog at the end of bypass.

There have been proposed modifications for the Hirsch mechanism [28, 31-33], including a combined Orowan and prismatic looping, shown schematically in Fig. 2.8(d), where a previously bypassed particle with an Orowan loop around it is bypassed again by another lattice dislocation. The Orowan loop cross-slips around the particle, forming two prismatic loops before a second Orowan loop is formed around the particle and the second prismatic loop is swept up by the dislocation to leave a jog. Ashby and Humphreys [28, 34] argued that this type of bypass alternates between Orowan looping and prismatic looping because the stress required for the latter is only slightly lower. Humphreys and Hirsch [29] and Humphreys and Stewart [35] reported that for hard SiO_2 particles in α-brass, Orowan looping always occurs prior to cross-slipping of either the Orowan loops themselves or via the dislocation bypass (which formed prismatic loops around the particles). As will be described in greater detail in Section 2.3, this interpretation may be

attributed to the incoherency of the particles and does not necessarily indicate that the critical shear stress is controlled by the Orowan mechanism. For a particle that has undergone bypass via the Hirsch mechanism, Fig. 2.8(e), a row of prismatic loops forms behind the particle and when a lattice dislocation again bypasses the particle, it leaves an additional prismatic loop in the row and a jog in the segment that continues glide [28, 34].

2.3 Experimental Observations of Room Temperature Interactions

The advent of transmission electron microscopy (TEM) enabled direct observation of dislocation and deformation microstructures in the 1950's and 60's [36]. It was also at this time that the investigation of dislocation-particle interactions begin in earnest and saw much advancement made in both interaction theory and its formulation [29, 37-43] because they could be compared directly with experimental results. This section will focus first on the techniques employed in studying dislocation-particle interactions in the transmission electron microscope, followed by a selective summary of relevant experimental work.

2.3.1 Observation Techniques

One of the standard techniques in use is *post mortem* analysis, which involves the observation and characterization of the microstructure after it has undergone deformation and/or some other processes which stimulated microstructural evolution. The static nature of this technique is both an advantage and a limitation—while detailed analyses could be performed on the defect structures present by using various imaging conditions, how the microstructure evolved to this point and how it will evolve if deformation were to continue cannot be recorded directly but must be inferred from other data. Fig. 2.9 shows an

example of *post mortem* analysis which compares a Cu-2.8%Co alloy containing coherent particles before (Fig. 2.9(a)) and after dynamic exploding wire loading (Fig. 2.9(b)). The *post mortem* structure shows the coarsening of the Co particles as well as the development of an extensive dislocation network [44].

In order to characterize dislocations and other defects, additional analysis is often performed. One of the most useful is $|\mathbf{g} \cdot \mathbf{b}|$ analysis, which makes use of the invisibility, or $|\mathbf{g} \cdot \mathbf{b}| = 0$, criterion—when the lattice displacement lies parallel to the reflecting plane, the dislocation image becomes invisible (for a screw dislocation). For a mixed character or edge, dislocation, the image is only nearly-invisible since complete invisibility requires $\mathbf{g} \cdot \mathbf{b} \times \mathbf{u} = 0$, which is much more difficult to satisfy. Fig. 2.10(a)-(c) illustrates this principle with a network of dislocation arrays in a face-centered cubic lattice imaged using three different diffraction vectors, $\mathbf{g} = \bar{1}11$, $\mathbf{g} = \bar{1}1\bar{1}$, and $\mathbf{g} = 00\bar{2}$, respectively. It can be seen that in Fig. 2.10(a) and (c), the horizontal array is visible under $\mathbf{g} = \bar{1}11$ but not under $\mathbf{g} = 00\bar{2}$. Analogous observations could be made for each of the dislocation arrays and by tabulating the values of the dot product of **g** with all possible **b** (in this case $\pm\frac{a}{2}\langle 110\rangle$), the Burgers vectors of each dislocation can be determined. An abridged table of $\mathbf{g} \cdot \mathbf{b}$ values is presented for reference in Fig. 2.11; for clarity, the 111-type reflections are shaded in red, the 002-type reflections in blue, and the 220-type reflections in yellow. For the example given above, the horizontal array of dislocations have a Burgers vector of $\mathbf{b} = \pm a/2[1\bar{1}0]$, or $\pm$**BA** in the Thompson tetrahedron notation [45]. Fig. 2.12 presents an exploded Thompson's tetrahedron, which annotates the slip systems in a face-centered cubic lattice (Fig. 2.12(b)): double English letters for perfect dislocations (Burgers vectors named as

beginning-to-end); one English and one Greek letter for partial dislocations (same convention); and single Greek letter for slip plane. The $(\bar{1}1\bar{1})$ plane is designated "α," the $(1\bar{1}\bar{1})$ plane "β," the $(\bar{1}\bar{1}1)$ plane "γ," and the (111) plane "δ." For convenience and ease of discussion, dislocations in this work will often be referred to by their Burgers vectors or the corresponding Thompson notations interchangeably.

Another key technique employed in studying dislocation-particle interactions is performing *in situ* experiments inside the TEM. This experimental method provides an opportunity to determine how dislocation motion is influenced by the presence of lattice defects such as other dislocations, precipitates, grain boundaries etc. [46]. The earliest *in situ* studies made use of the electron beam: Hirsch *et al.* [47] observed the motion of dislocations in an Al thin foil due to beam heating in 1956 and Pashley and Presland [48] used the electron beam to irradiate a gold foil for 100 seconds (Fig. 2.13(a)) and 1000 seconds (Fig. 2.13(b)) in 1961. In Fig. 2.13, the small black-white contrast dots are loops produced by irradiation; and it can be seen that with increasing irradiation dosage, the size and density of loops has increased. For the study of dislocation-particle interactions, *in situ* experiments allow the movement of dislocations bypassing particles in the sample to be recorded and analyzed. This is a technique that has been used extensively in this work and the captured videos will be represented by selected freeze frames in Ch.4. Whereas *post mortem* observation is static, *in situ* straining captures the dynamics of microstructural evolution but in general lacks detailed characterization, especially since defect structures can be become annihilated through subsequent interactions. Thus, the prudent use of both techniques to complement and inform the data gathered is essential in obtaining a complete

characterization of the materials and processes being studied. Sections 2.5 and 2.6 will discuss another method which augments these techniques with spatial resolution.

2.3.2 Summary of Results

Ever since Kelly and Nicholson unified precipitation strengthening as a single field [39], much experimental work has been conducted. Early work focused primarily on theoretical formulations for the strengthening mechanisms and the creation of defects and dislocations as by-products of dislocation-particle interactions [28, 30, 41]. From the 1970's on, the bypass of a particle by lattice dislocations at room temperature was believed to be primarily controlled by the particle size: These "classical" mechanisms predict that when a particle is small, dislocations sheared them; and at a larger sizes, the bypass mechanism transitions to Orowan looping [5-6] with the transition radius corresponding to the intersection of the curves representing strengthening due to Orowan looping and cutting [39]. While this is still accepted in general, copious experimental work has since shown it to be only a subset of a vast array of possible dislocation-particle interactions [17, 34, 49-50]. Humphreys and Hirsch, for example, observed both classical as well as non-classical behavior for SiO_2 particles in a Cu matrix [29]. Fig. 2.14(a) shows the bypass of several particles with large Orowan loops interspersed with prismatic loops created by the Hirsch mechanism (compare with Fig. 2.8(d)-(e)). However, for larger particle sizes and higher strains, full prismatic loops were not formed. Instead, a more complex structure developed involving the creation of partial shear loops, Fig. 2.14(b), which could then cross-slip around the original glide prism, a schematic of which is shown in Fig. 2.14(c). With continued deformation, these loops can expand out and eventually interact with similar

structures from neighboring particles. These interactions can quickly lead to the production of dislocation tangles in the inter-particle regions—indicating the importance of taking into account parameters such as strain rate and strain history—an area that is not well addressed by the classical mechanisms.

In addition, historically only isotropic, spherical particles have been considered in the models. For non-spherical (such as rod- or plate-shaped) semi-coherent particles, however, the problem is more complex. A precipitate with an asymmetric geometry, for instance, can be semi-coherent with the matrix to different degrees along different facets. A number of studies have been conducted on post-mortem deformed samples to determine the dislocation-particle interactions. Donnadieu *et al*. [51], for example, conducted post-deformation TEM and HREM observations on 6xxx series aluminum alloys containing nanosized precipitates which showed that bypass by screw segment cross-slip rather than Orowan looping was more common. Russell and Ashby [49], however, maintained that for {111} platelet particles in Al-Cu, looping bypass of the particles reminiscent of the Orowan mechanism takes place and that no shearing of the particles was detected. With repeated bypass, the loops stacked up along the particle interface and can collapse to form a dislocation wall.

Other experimental work explored the stability the Orowan loops after bypass. Fig. 2.15 shows experimental observation of dislocation-particle interactions in Nimonic PE16 Ni superalloy containing γ-particles [52], Fig. 2.15(a), and an Al-Li 8090 alloy containing δ-particles during *in situ* TEM straining (Fig. 2.15(b)) and *post mortem* analysis ((Fig. 2.15(c)) [53]. The contour of the dislocation which has bypassed the particles is superimposed with a dashed line for clarity in Fig. 2.15(b) and subsequent *post mortem*

observation revealed particle shearing (black lines on the particles in Fig. 2.15(c) by Orowan loops of diameter at least 200Å around the δ-precipitates, above the classical transition between shearing and Orowan bypassing. Instead of particle-shearing below a critical precipitate radius, a mixed reaction occurred involving "delayed shearing" of large precipitates by the Orowan loops when the applied stress reached a critical value. For both of these alloys, Orowan looping occurred initially but with increasing stress the particles were themselves sheared by the Orowan loops. Other studies [53-54] have also found the shearing/looping models to be insufficient in fully characterizing the interaction between glide dislocations and particles. The fact that classical bypass was observed alongside more complicated structures experimentally illustrates the range and complexity of dislocation-particle interactions and highlights a need to encapsulate these observations in more realistic models.

2.4 Computer Modeling of Room Temperature Interactions

The increase in computer processing power offered an alternative avenue for the study of dislocation-particle interactions. Numerical as well as computer models have been used extensively to characterized these interactions in recent years and have the potential to greatly expedite and enhance alloy design, testing, and the time to market. These simulations often rely on the shearing/looping models and thus ignore dynamical effects or details of the interactions, leading to limited applicability across wide length scales. In large part, the studies are specific to a particular alloy system while focusing on a limited length scale [51, 55-56]. Yashiro et al. [57] for example, developed a discrete dislocation

dynamic model for the cutting of cuboidal γ' precipitates in Ni superalloys which showed a partial cutting of the precipitates by dislocations when forming an Orowan loop. While the models performed well for their material systems, it remains difficult to obtain general conclusions or insight on similar systems (e.g., for the same alloy of a slightly different composition or microstructure).

Some computer simulations have also revealed new details previously unaccounted for in classical theory, which have the ability to inform the interpretation of experimental results. For example, Srolovitz and co-workers investigated dislocation particle interactions at room temperature using dislocation dynamics computer simulations [54], Fig. 2.16. Fig. 2.16(a) shows the interaction between a hard spherical particle and an edge dislocation at h = 0 where h, the intersection height of the dislocation, is positive above the slip plane and negative below the slip plane and R is the particle radius. The interaction is equivalent to Orowan looping. In the interaction between a hard spherical particle and a screw dislocation at h = 0.5R (Fig. 2.16(b)), however, the loop that formed initially cross-slips locally and pinches off into two smaller loops lying on the cross-slipped planes. And in Fig. 2.16(c), the interaction between a misfitting spherical particle and an edge dislocation at h = 0.5R shows the creation of two non-glide loops from double cross-slipping around the particle. Because cross-slip occurs immediately upon interaction, an Orowan loop was prevented from forming. The computer model demonstrates that the interaction that takes place when a lattice dislocation bypasses a particle can depend on the intersection height, h, and cross-slip is favored over Orowan looping when the intersection of the slip plane with the particle is not near the middle. Theoretical calculations

containing persistent Orowan loops have also shown that the strongly repulsive interaction between an Orowan loop and a dislocation would result in unreasonably strong work hardening [28, 58-59]

The Hirsch mechanism has also been investigated by using molecular dynamics simulation between a hard particle and an edge dislocation [60], Fig. 2.17. The dislocation undergoes cross-slip at bowed-out segments followed by double cross-slip (Fig. 2.17(c)) leaving prismatic loops behind and in front of the particle, Fig. 2.17 (d)-(e). As predicted by the Hirsch mechanism, a row of interstitial prismatic loops form behind the particle. However, the jog on the original segment is dragged some distance before detaching as a vacancy loop, Fig. 2.17(e), and with successive bypass the loops in front become a dislocation tangle extending close to the particle interface. Fig. 2.18 presents snapshots from an atomistic simulation between a hard particle under hydrostatic stress. Shear loops are generated at the particle-matrix interface, Fig. 2.18 (a)-(b), and through multiple cross-slip events, Fig. 2.18(c), can become prismatic loops which interact with each other at or very close to the interface, Fig. 2.18(d) [61-62]. What Figs. 2.17 and 2.18 illustrate is that the region surrounding a particle can quickly become a pinning site for dislocations and interaction debris. Certainly, the elastic interactions predicted by classical theory is shown to be insufficient in realistically portraying and predicting the complexity of dislocation-particle interactions reported by experimental observations and for computer simulations.

2.5 Principles of Electron Tomography

Since its inception in the 1950's, electron microscopy has become a potent tool for the characterization and analysis of materials. Yet the inherent limitation of a micrograph

as the two-dimensional projection of a three-dimensional (3D) specimen volume means that depth information in the electron beam direction is lost. For the analysis of dislocation-particle interactions, for instance, the spatial relationship between defect structures and the particle such as inclination or slip plane cannot be discerned easily. Some early attempts in recovering the depth information used stereographic imaging, where two images separated by about 10^{o} to 14^{o} are recorded and viewed simultaneously through a stereographic viewer [63]. Alternatively, the images can be superimposed, one colored red and the other blue to form an anaglyph and viewed using red-blue glasses. In either case, however, these methods are limited to the perception of depth in one fixed viewing direction and any recovery of depth information is difficult to quantify even with prior knowledge about the microstructure.

In recent years, there has been a renewed interest in overcoming these limitations via a new technique known as electron tomography. Used in the life sciences for nearly 50 years for 3D imaging of biological macromolecules, it involves acquiring multiple images of a region of interest at a range of viewing angles or depths followed by reconstructing the volume to produce a 3D representation of the region [64-66]. Fig. 2.19(a)-(c) shows three general types of tomography: (a) Computed tomography (CT of CAT scan) for medical imaging, (b) electron tomography for subcellular structure imaging, and (c) single-particle reconstruction which involves multiple occurrences of a molecular or particle in different orientations. The main difference between them lies in the relative orientation between the imaging source and the specimen. For a CT scan, the rigid source-detector array rotates around a stationary axis whereas for electron tomography the source is stationary and parallel and the sample is titled about an axis normal to the beam. The source-sample

configuration shown in Fig. 2.19(b) is the most relevant to this work and the term "electron tomography" will be used in subsequent references for this configuration. Some examples of the capability of depth extraction and visualization via electron tomography as used in the life sciences are presented in Fig. 2.19(d) and (e). The cell image presented in Fig. 2.19(d) is a segmentation slice—essentially a cross-section taken at an arbitrary depth—from a tomographic reconstruction of *Pyrodictium* where the outer cell wall is highlighted in red and various interior structures are visible. Alternatively, the reconstruction can be visualized in 3D, Fig. 2.19(e), as a rendered isosurface tomogram. The model shows two vesicles (in white), one of which contains two types of macromolecules (orange and blue) surrounded by carbon film (in gray) [64]. Application of electron tomography in the physical sciences, however, poses some unique challenges compared with the established technique as used in the life sciences. This section will briefly introduce the principles behind tomographic reconstruction, its theoretical requirements and limitations; and finally, challenges and imaging methods for achieving 3D visualization of defect structures using diffraction-contrast tomography.

2.5.1 Procedure & Requirements of Electron Tomography

Electron tomography utilizes the Fourier transform, which provides a representation of the sample volume by a series of trigonometric basis functions, in back-projection algorithms in order to reconstruct the volume. For the purposes of this work, these algorithms are embedded in the reconstruction software (see Chapter 3) and not dealt with directly. Essentially, the 3D Fourier transform of the volume of interest can be sampled by collecting its 2D projections in the microscope. With a sufficient number of projections

over the available angular range, a full description of the object can be obtained. And through algorithms such as weighted back-projection (WBP) or simultaneous iterative reconstruction (SIRT), which apply an inverse Fourier transform to the projections in the data set, a three-dimensional real-space reconstruction of the original object can be produced. Fig. 2.20(a) shows the sampling of Fourier space by the 2D projections. Ideally, projections over 180° tilt range, as seen in Fig. 2.20(a), can fully sample the object's Fourier space but in practical application the tilt range is often severely limited (typically 70^{o} total) due to: (1) The objective pole piece gap of the microscope; (2) the thickness and width of the specimen holder, which must tilt within this gap; and (3) specimen shadowing at higher tilts either due to the sample holder or other regions of the specimen itself. This non-uniform sampling of Fourier space results in a "missing wedge" (Fig. 2.20(b)) of projections which can produce elongation artifacts in the undersampled projection directions. Other collection schemes have been developed to more fully sample the 3D Fourier space; two of these are shown in Fig. 2.20(c) for a double-axes tilt scheme and in Fig. 2.20(d) for a tilt-rotate scheme resulting in conical sampling [64]. The application of these collecting geometries will be discussed in greater detail in Ch.3.

Additionally, the images used in the projections should satisfy the projection requirement, which states that the signal must be a monotonic function of some physical property such as atomic number (Z) or sample thickness. Fig. 2.21 presents some examples of imaging methods which satisfy the projection requirement: (a) An *acidophilum* cell imaged under mass-thickness contrast with bright-field TEM. The cell image is low in contrast and intensity but the Au nanoparticle markers to the left side of the image show strong contrast due to its mass difference with the substrate. (b) Pd_6Ru_6 nanoparticles in a

silica support imaged under Z-contrast with high-angle annular dark-field (HAADF) scanning transmission electron microscopy (STEM). The nanoparticles are bright against the substrate due to its higher Z. In general, diffraction-contrast imaging does not satisfy this requirement since local image intensities depend on a variety of interacting parameters such as strain field, foil thickness, magnitude of deviation from Bragg diffracting condition, foil bending…etc. An example of an imaged formed using diffraction-contrast (bright-field TEM) is presented in Fig. 2.21(c), where a few dislocations can be seen against an Al matrix. The image contrast is strong compared with Fig. 2.21(a)-(b) and is highly dynamic across the whole image, which compounds the difficulty of image series alignment. Section 2.6.2 will address the issues involved in making diffraction-contrast images amenable to electron tomography.

2.5.2 Resolution of Tomograms

Due to the incomplete sampling of Fourier space, the resolution of the tomogram is in general poorer than that of the original micrographs. For a specimen tilted along a single axis, X, the back-projection reconstruction resolution in the direction parallel to the tilt-axis, d_x, is equal to the resolution of the original micrographs. The resolution in the non-depth direction perpendicular to the tilt axis, d_y, is given by Eq. 2.5, known as the Crowther criterion [67]:

$$d_y = \frac{\pi D}{N} \qquad \text{(Eqn. 2.5)}$$

where D is the diameter of the volume being reconstructed and N is the number of projections acquired. The resolution in the depth direction (parallel to the optic axis), d_z, is

further reduced by an elongation factor, E_{yz}, when the maximum tilt range, ±α, is limited to less than ±90^o [68].

$$d_z = d_y E_{yz} = d_y \sqrt{\frac{\alpha + \sin\alpha\cos\alpha}{\alpha - \sin\alpha\cos\alpha}} \qquad \text{(Eqn. 2.6)}$$

Fig. 2.22 shows the dependence of the tomogram resolution on the angular tilt range and N. Assuming a tilt range of 80^o with a tilt increment of 1^o, the best theoretical resolution obtainable is approximately 10 nm. In many cases, other factors such as alignment errors can lead to the effective resolution being somewhat lower.

Using a double-tilt sample holder, in which the specimen can be tilted in both the X- and Y-directions, or a tilt-rotate holder, in which the sample can be rotated as well as tilted, allows for greater sampling of the specimen's Fourier space. Instead of the "missing wedge" of a single-tilt holder, it will instead be a pyramid or cone of missing information, respectively (see Fig. 2.20(c) and (d)). The SIRT algorithm can also enhance the resolution of the tomogram by employing calculated differences between the reconstruction and the projections to further refine the data points. In these situations, the above resolution calculations do not apply, but Midgley *et al.* propose a rule of thumb based of their experience; for objects where D > 100 nm, the 3D resolution is roughly D/100 [69].

The effect of the angular tilt range on the resolution can be visualized in Fig. 2.23(a), where a synthetic 2D object ("phantasm") has been reconstructed using several tilt ranges represented by half angles ±α, with projections taken every 1° along that range. The middle column was produced using direct back-projection reconstructions and the right column by weighted back projection reconstructions. As the angular tilt range sampled increases, the

blurring in the under-sampled direction greatly decreases and the resolution of specimen detail increases (also compare with Fig. 2.22). The effect of different values of N is illustrated in Fig. 2.23(b), where the phantasm has been reconstructed using varying numbers of projections spaced evenly across a tilt range of ±90°. The trend, like with maximum tilt range, is straightforward: the greater the number of projections taken (i.e., the smaller the angular spacing between projections), the better the tomogram resolution in the depth direction and the higher the fidelity of the reconstruction [69].

2.6 Extension of Electron Tomography for Defect Imaging

Even though electron tomography is a standard technique in the life sciences, direct extension of it for the imaging of crystalline materials have not been straight forward due to some unique challenges. The following sections will address these issues and more importantly, demonstrate how they can be overcome such that electron tomography can be used to obtain spatial information about the volume of interest.

2.6.1 Practical Challenges

- Maintaining Image Contrast

Recording dislocations and other crystal defects in the transmission electron microscope necessitates the use of diffraction-contrast imaging. Common techniques such two-beam bright-field (BF), centered dark-field (CDF) and weak-beam dark-field (WBDF) all rely on the strain field of the object satisfying the Bragg condition in order to produce contrast. The simplest way to accomplish this goal is to adhere to a single Kikuchi band for all micrographs that make up the tilt-series such that the dominant contributing factors to

contrast, **g** and **s**, the diffracting vector and the Bragg deviation parameter respectively, are maintained. Fig. 2.24(a) demonstrates the effect of varying values of **s** on the image contrast: From left to right, **s** = 0, **s** > 0, and **s** >> 0, respectively. The geometry of the foil can also influence contrast, the effect of which is stronger at thinner parts of the sample. One of these effects, thickness fringes (Fig. 2.24(b)), result from oscillations in the transmitted and diffracted wave intensities with depth into the foil. As the foil thickness increases, left to right in Fig. 2.24(b), anomalous absorption gradually reduces the intensity of the fringes. Another foil geometry-induced contrast comes from bend extinction contours, Fig. 2.24(c), where the concave/convex bending of the foil causes the areas satisfying the Bragg condition to appear as a dark band. For both of these foil-related phenomena, maintaining constant contrast in their vicinity is difficult and should be avoided. When imaging a region containing sheet-like defect such as stacking-faults or precipitates, the phase change between the incident and diffracted waves causes fringe contrast. These displacement fringes, seen in Fig. 2.24(d) for plate particles, can also become invisible due to overlapping faults, "A."

- Tilting the Specimen

The range of tilt angles used for electron tomography of biological specimens is typically at least $\pm 70°$ [65-66]. In the normal experimental setup for crystalline materials, however, this range is often drastically restricted due to practical limitations such as the pole piece gap in the TEM, specimen stage thickness and width, and, to a lesser extent, the "shadowing" produced by the specimen itself. These limitations can be somewhat mitigated by the reduction in the thickness and width of the TEM stage but it is not

uncommon for double-tilt TEM stages to have only $\pm 35°$ of primary (X- or α-) tilt and $\pm 20°$ of secondary (Y- or β-) tilt. It is important to note that in such instances, the number of micrographs, N, should be maximized by acquiring images every 1° of primary tilt. While it is possible to reconstruct a tomogram with approximately 70° angular tilt range [50], a larger range, if it can be managed, is certainly desirable.

In the case of a thin-profile stage, a larger primary tilt range is often possible only at the expense of having no secondary tilt. Commercial tomography stages with large tilt range of $\pm 70°$ or more, such as Fischione's 2000-series or several of Gatan's 900 models, are also available. For diffraction contrast imaging, the suitability of a specimen will depend on whether a two-beam condition exists at near-zero tilt. If not, either a double-tilt stage with smaller tilt-range needs to be used or a change of sample is required. If the condition is reasonably satisfied, the Kikuchi band can be made parallel to the primary axis of tilt by rotating the sample itself. This is also the case for (single) tilt-rotate stages, except the operation can be performed inside the microscope and with greater precision.

2.6.2 Imaging Methods

For the TEM and STEM, a variety of imaging methods exists: two-beam bright-field/center dark-field TEM, kinematical bright-field TEM, weak-beam dark-field TEM, HAADF STEM, energy-filtered TEM…etc. It has already been mentioned that diffraction-contrast imaging does not strictly satisfy the projection requirement, which calls for the image contrast to be a linear function of a physical property of the sample. However, for the study of dislocation networks and deformation substructures in crystalline materials,

those techniques employing diffraction contrast are particularly well-suited. The challenge lies in minimizing contrast variations across tilt series images such that the fidelity and resolution of the reconstruction is not significantly affected.

The primary difference between the imaging techniques lies in the type and resolution of information they yield and the ease of producing a tomogram. For instance, STEM typically has a slightly lower resolution than does weak-beam dark-field TEM at around 0.2 nm or below [70]; but has significant advantages both in the ease of acquisition (being less sensitive to strain-contrast) and image contrast [36]. Also, in areas of densely overlapped dislocation structures, weak-beam dark-field, which images dislocations close to the dislocation core and has a narrower image, is more suitable. This is illustrated by the micrographs presented in Fig. 2.25: (a) and (c) weak-beam dark-field and (b) and (d) two-beam bright-field images of a sparsely vs. densely dislocated region. The best imaging technique will therefore depend on the complexity and scale of the defect structures balanced with the ease and time of tilt series acquisition. Throughout this work, in particular Section 4.4, a number of imaging methods were employed based on these considerations.

2.7 Figures

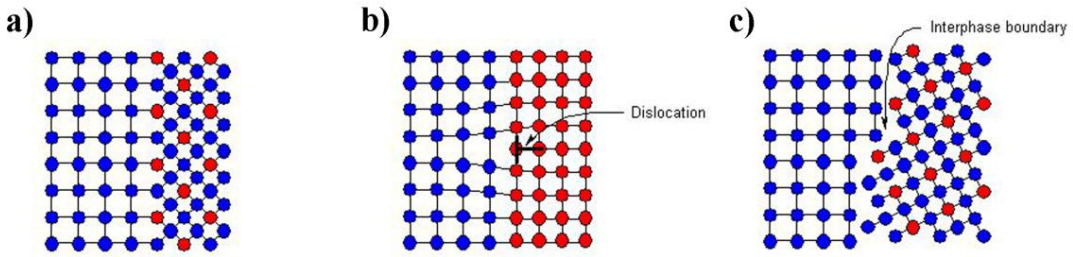

Fig. 2.1. The interface between the matrix material (left lattices) and the precipitate particle (right lattices). (a) A coherent interface, where lattice planes are well-matched on both sides; (b) a semi-coherent interface, with partial lattice matching and interfacial dislocations; and (c) an incoherent interface, where no lattice matching remains [9].

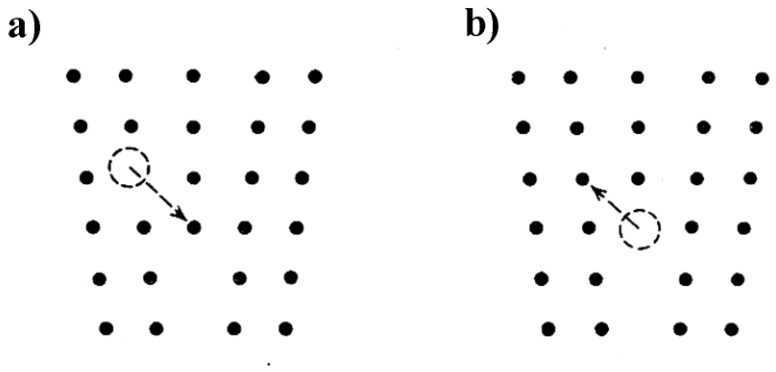

Fig. 2.2. (a) Diffusion of a vacancy to an edge dislocation resulting in (b) positive dislocation climb up one lattice spacing [6, 12].

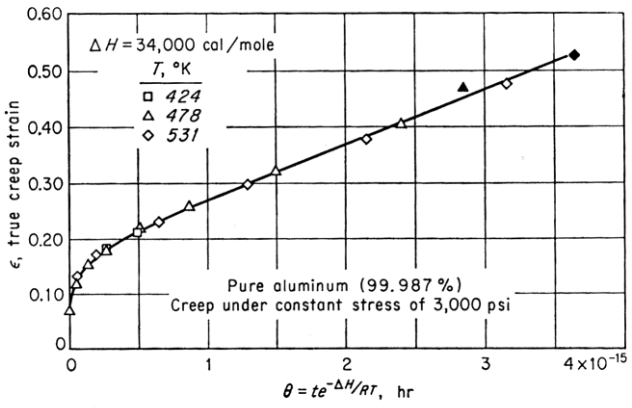

Fig. 2.3. An example of steady-state creep for pure Al where creep strain is plotted against the temperature-compensated time parameter θ [13].

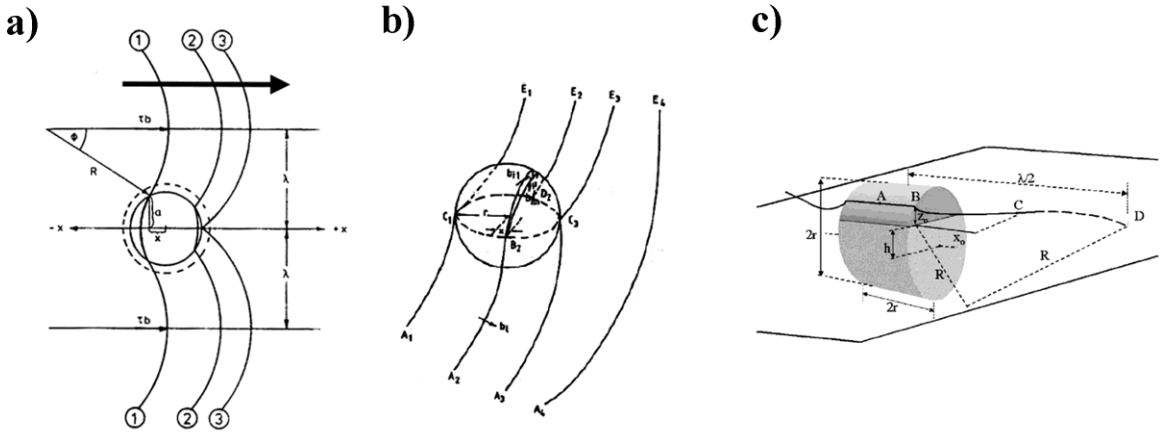

Fig. 2.4. Schematics of the rate-limiting steps in three creep models: (a) Detachment-controlled creep model focusing on thermally-activated dislocation detachment from the particle [14]; (b) dissociated-controlled creep model focusing on dislocation dissociation in the particle interface [15]; and (c) climb-controlled creep model focusing on the rate of dislocation climb [16].

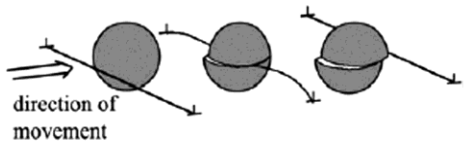

Fig. 2.5. Schematic of a dislocation line shearing a precipitate particle along the slip plane intersection. The particle is displaced by |b|. After [5].

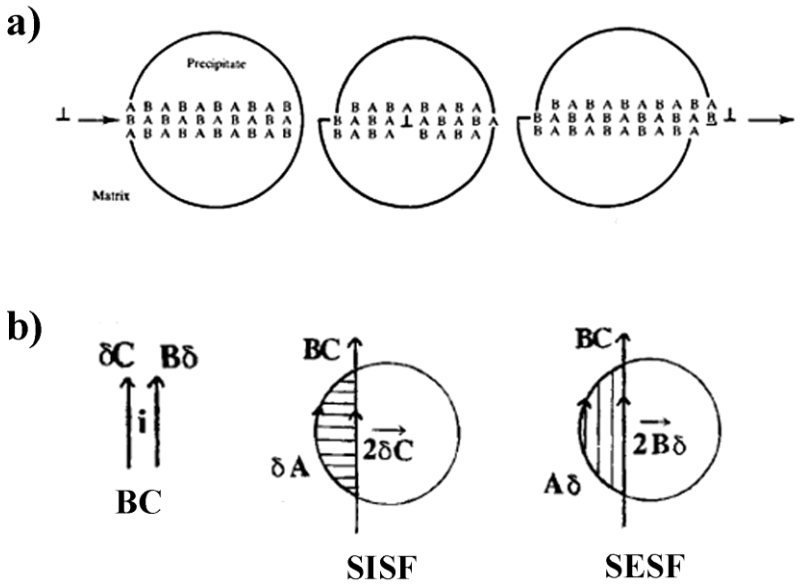

Fig. 2.6. Lattice miss-stacking created by particle shear: (a) Antiphase boundary in a particle with stacking "AB" sheared by an edge dislocation [7]; and (b) Superlattice stacking-fault (left: intrinsic, right: extrinsic) sheared by super Shockley partials [19].

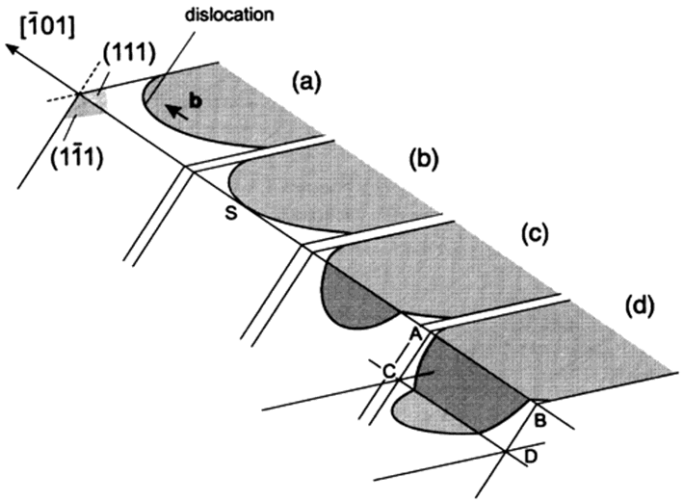

Fig. 2.7. Cross-slip of a dislocation with a Burgers vector of b = $a/2[\bar{1}01]$ in the face-centered cubic crystal system. (a)-(b) The dislocation segment with screw character, S, cross-slips (c) from the (111) plane onto the conjugate $(1\bar{1}1)$ plane. (d) The same segment double cross-slips back onto a parallel (111) plane [5].

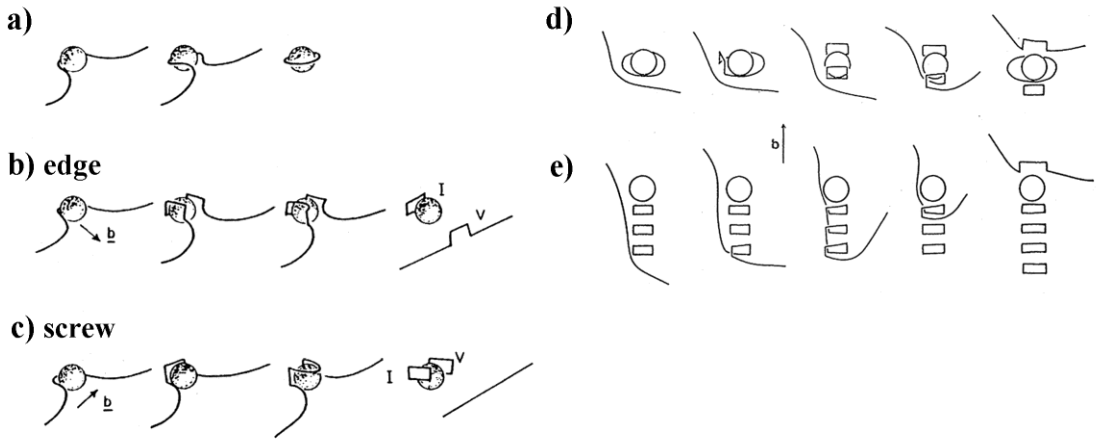

Fig. 2.8. Dislocation-particle bypass mechanisms involving the creation of loops. (a) The Orowan mechanism and the Hirsch mechanism with (b) an edge and (c) a screw dislocation, leaving prismatic loops with cross-slipped segments out of the slip plane. (d)-(e) Bypass of particles already looped. After[28] and [29, 34].

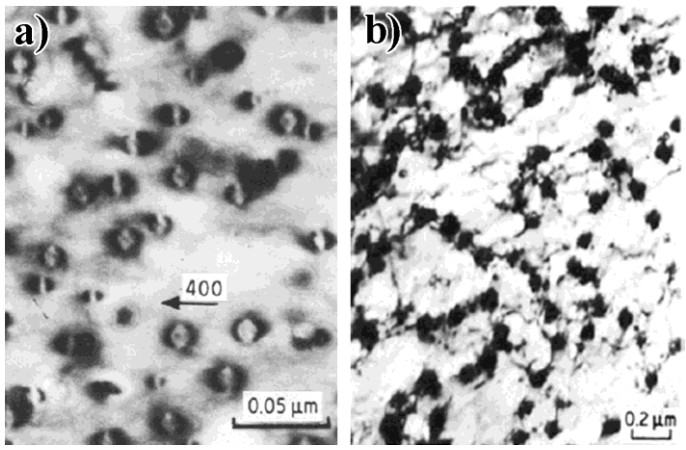

Fig. 2.9. An example of *post mortem* analysis comparing (a) as-aged Cu-2.8%Co (650^{o}C for 150 min) showing coherency contrast Co particles with (b) after dynamic exploding wire loading showing coarsening of the Co particles and high dislocation density. After [44]

.

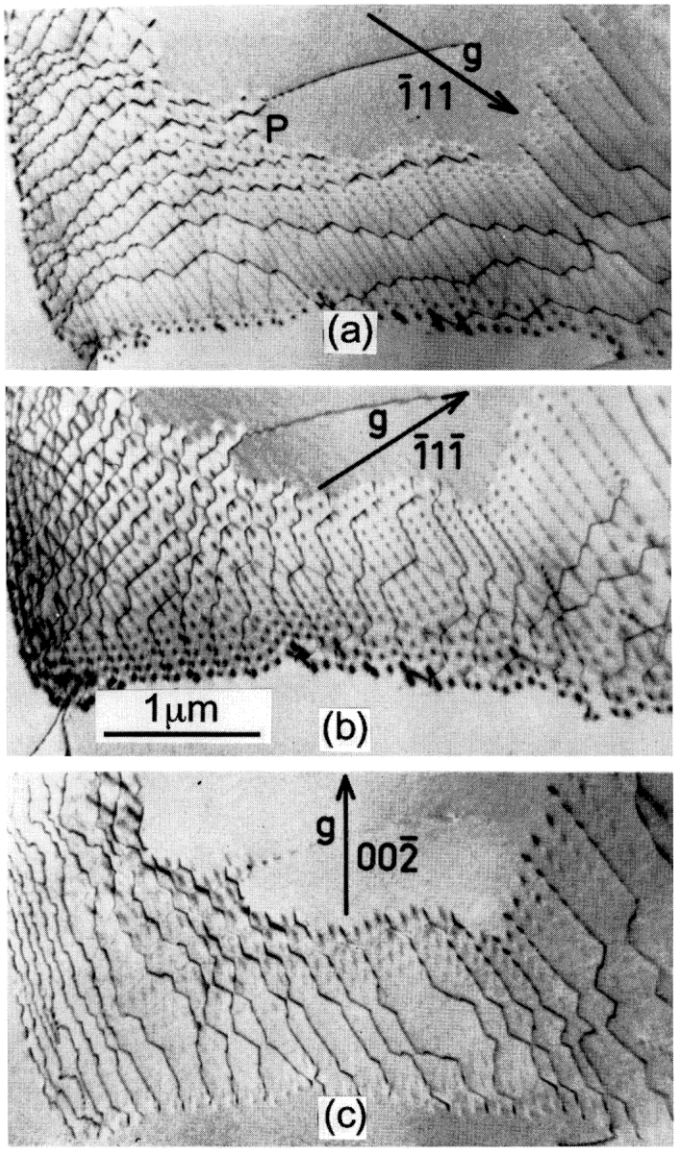

Fig. 2.10. An example of |g · b| analysis, a customary technique used during *post mortem* examination. The region containing the dislocation network is imaged using a number of diffraction vectors, g. When |g · b| = 0, dislocations are invisible [5, 71].

Reflection	Possible Burgers vector (times $a/2$)					
	$\pm[110]$	$\pm[1\bar{1}0]$	$\pm[101]$	$\pm[10\bar{1}]$	$\pm[011]$	$\pm[01\bar{1}]$
111	±1	0	±1	0	±1	0
$\bar{1}\bar{1}\bar{1}$	∓1	0	∓1	0	∓1	0
$\bar{1}11$	0	∓1	0	∓1	±1	0
$1\bar{1}\bar{1}$	0	±1	0	±1	∓1	0
$1\bar{1}1$	0	±1	±1	0	0	∓1
$\bar{1}1\bar{1}$	0	∓1	∓1	0	0	±1
$11\bar{1}$	±1	0	0	±1	0	±1
$\bar{1}\bar{1}1$	∓1	0	0	∓1	0	∓1
200	±1	±1	±1	±1	0	0
$\bar{2}00$	∓1	∓1	∓1	∓1	0	0
020	±1	∓1	0	0	±1	±1
$0\bar{2}0$	∓1	±1	0	0	∓1	∓1
002	0	0	±1	∓1	±1	∓1
$00\bar{2}$	0	0	∓1	±1	∓1	∓1
220	±2	0	±1	±1	±1	±1
$\bar{2}\bar{2}0$	∓2	0	∓1	∓1	∓1	∓1
$2\bar{2}0$	0	±2	±1	±1	∓1	∓1
$\bar{2}20$	0	∓2	∓1	∓1	±1	±1
202	±1	±1	±2	0	±1	∓1
$\bar{2}0\bar{2}$	∓1	∓1	∓2	0	∓1	±1
$20\bar{2}$	±1	±1	0	±2	∓1	±1
$\bar{2}02$	∓1	∓1	0	∓2	±1	∓1
022	±1	∓1	±1	∓1	±2	0
$0\bar{2}\bar{2}$	∓1	±1	∓1	±1	∓2	0
$02\bar{2}$	±1	∓1	∓1	±1	0	±2
$0\bar{2}2$	∓1	±1	±1	∓1	0	∓2

Fig. 2.11. Values of g · b for three common g-vector families in the FCC system where perfect dislocations have a Burgers vector b = $a/2\langle110\rangle$. The 111-type reflections are shaded in red, the 002-type reflections in blue, and the 220-type reflections in yellow. After [72].

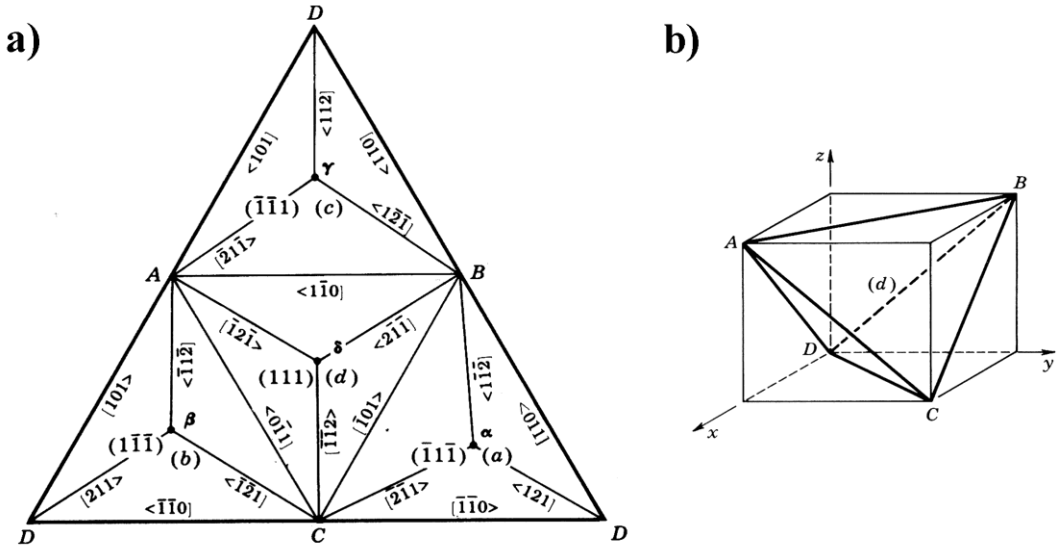

Fig. 2.12. (a) A Thompson's tetrahedron used in representing slip systems in the FCC lattice, opened at corner D. (b) The closed tetrahedron oriented in a unit cell [25, 45]. The Thompson notation for perfect dislocation "AB" is b = $a/2[\bar{1}10]$, with possible slip planes "γ" $(\bar{1}\bar{1}1)$ and "δ" (111) and dissociated partials (on δ) "Aδ" $a/6[\bar{1}2\bar{1}]$ + "δB" $a/6[\bar{2}11]$.

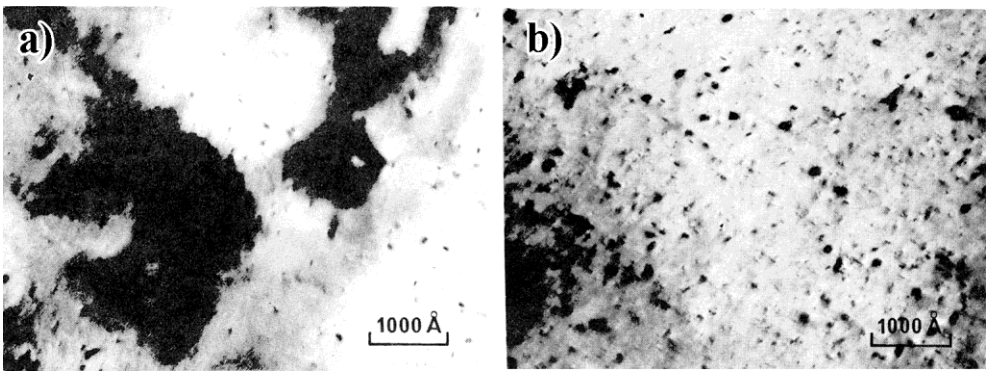

Fig. 2.13. An early study utilizing *in situ* observation in the microscope. (a) A single-crystal Au foil in the (111)-orientation irradiated by the electron beam after 100 sec. and (b) 1000 sec. [48, 73].

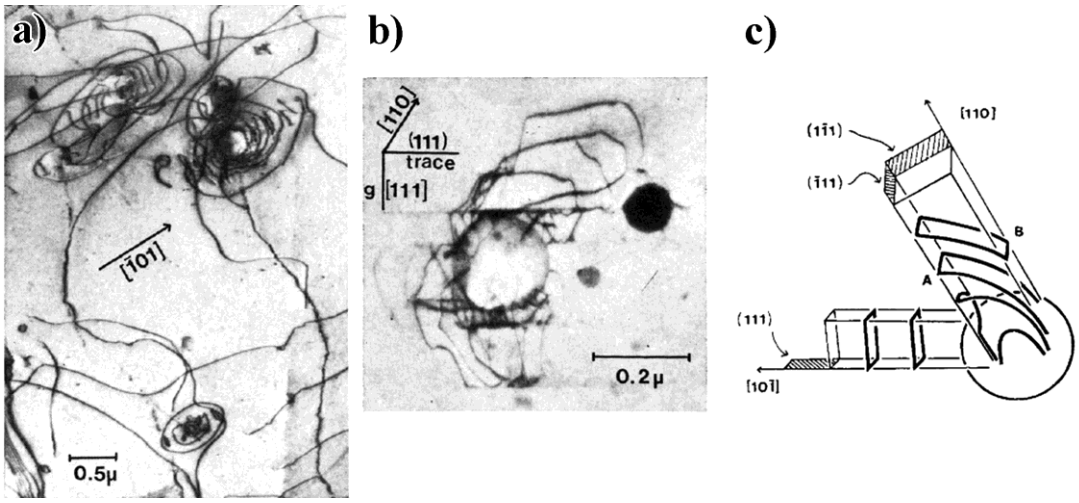

Fig. 2.14. Experimental observation of dislocation-particle interactions in α-brass containing SiO_2 particles showing both (a) classically predicted behavior (see Fig. 2.8(d)-(e)) involving Orowan looping and prismatic loop punching and (b) non-classical behavior involving the creation of partial shear loops. (c) is a schematic of (b)[34-35].

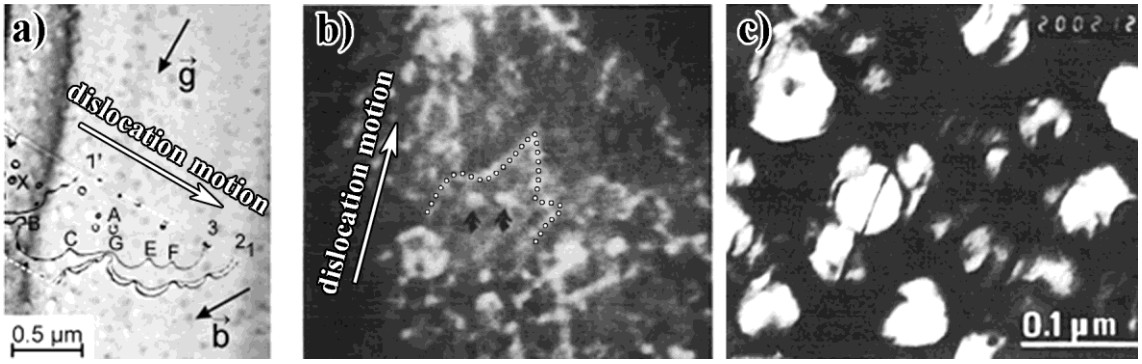

Fig. 2.15. Experimental observation of dislocation-particle interactions in (a) Nimonic PE16 Ni superalloy containing γ-particles [52] and (b) Al-Li 8090 alloy containing δ-particles *in situ* and (c) *post mortem* [53]. Orowan looping occurred initially but with increasing stress the particles were themselves sheared by the Orowan loops; compare with Fig. 2.8(d).

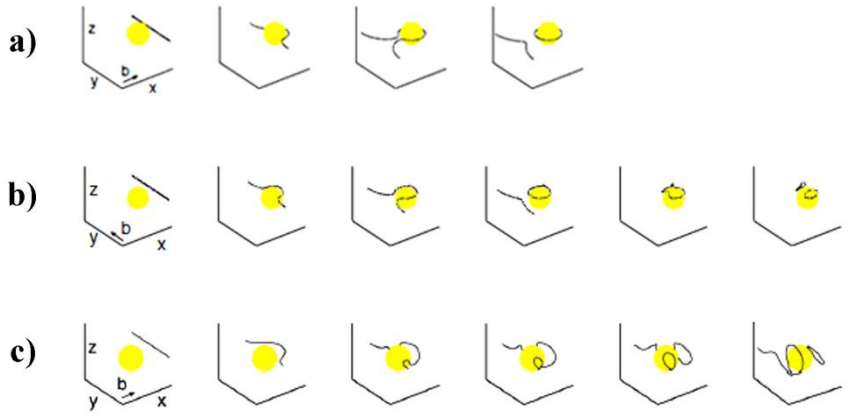

Fig. 2.16. Dislocation dynamics simulation between a (a) hard spherical particle and an edge dislocation at h = 0; (b) hard spherical particle and a screw dislocation at h = 0.5R; and (c) misfitting spherical particle and an edge dislocation at h = 0.5R where h, the intersection height of the dislocation, is positive above the slip plane and negative below the slip plane and R is the particle radius [54].

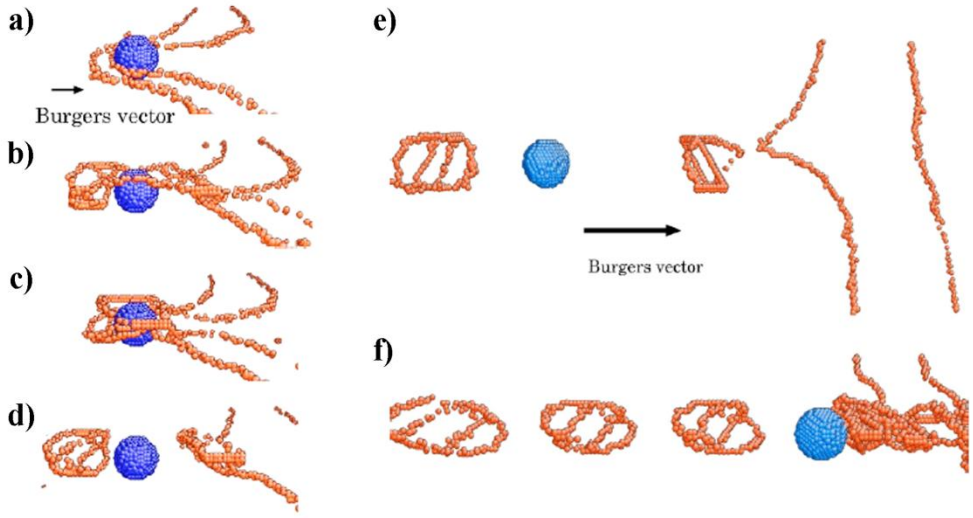

Fig. 2.17. Snapshots from a molecular dynamics simulation between a hard particle and an edge dislocation. (a)-(b) The dislocation undergoes cross-slip at bowed-out segments followed by (c) double cross-slip leaving behind prismatic loops (d) behind and (e) in front of the particle as predicted by the Hirsch mechanism [30]; but with successive bypass the loops in front form a dislocation tangle [60]

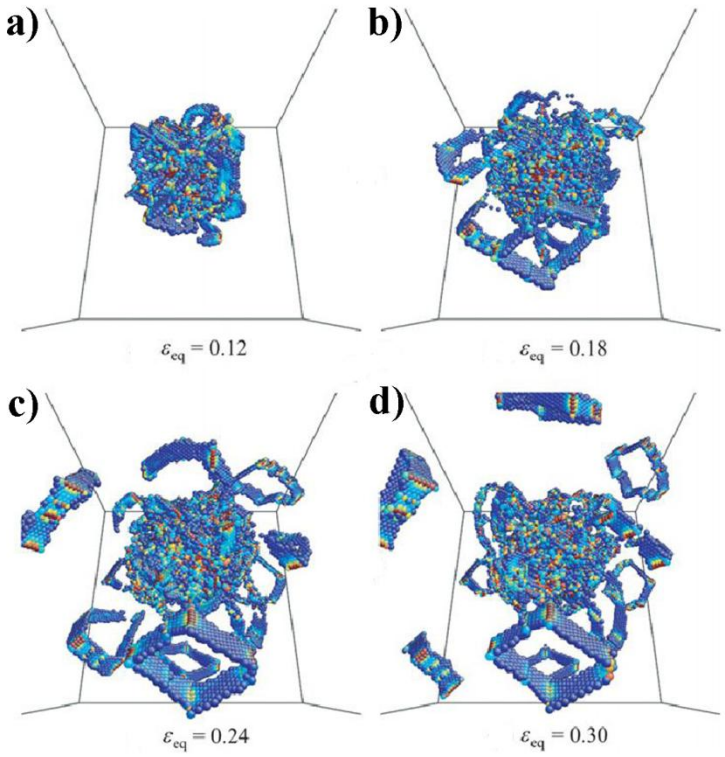

Fig. 2.18. Snapshots from an atomistic simulation between a hard particle under hydrostatic stress; only atoms with a potential above -3.33eV are shown. (a)-(b) Shear loops are generated at the particle-matrix interface and through (c) multiple cross-slips, become (d) prismatic loops which interact with each other at or very close to the interface [61-62].

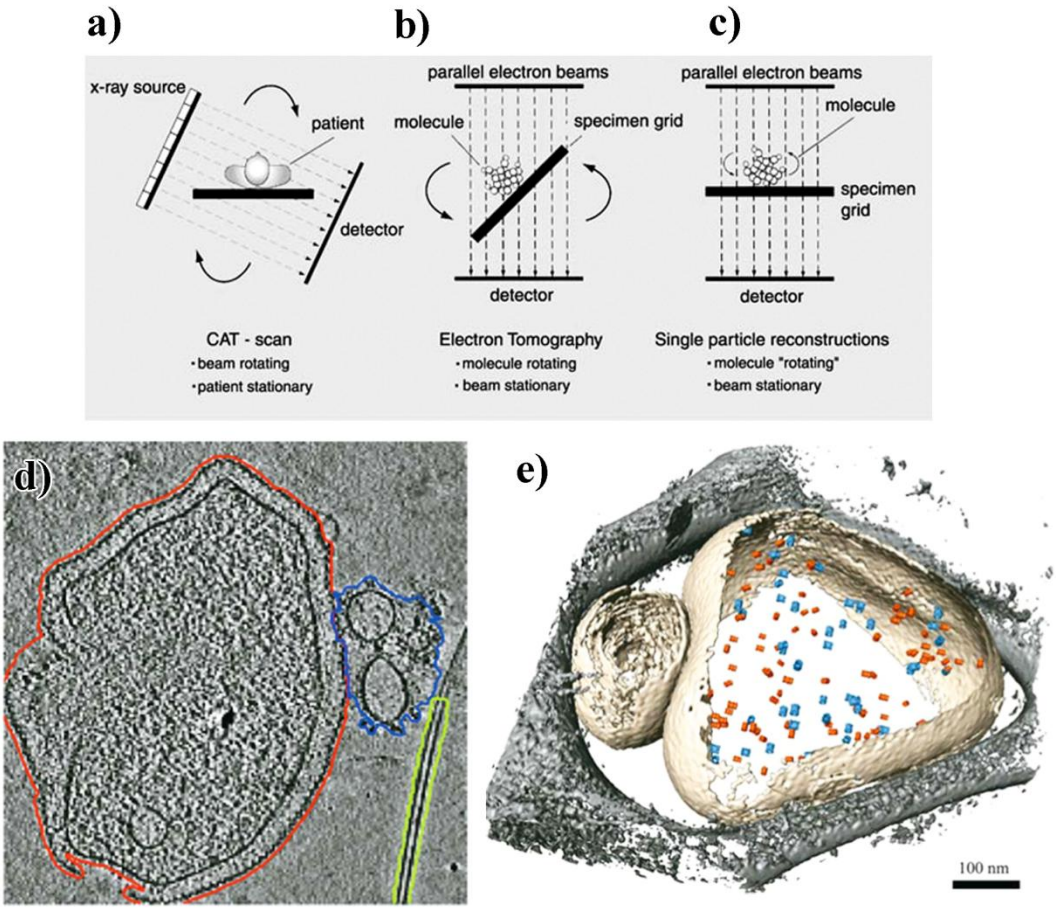

Fig. 2.19. (a)-(c) A schematic of the three main types of tomography: (a) Computed tomography ("CT" or "CAT" scan), (b) electron tomography, and (c) single-particle reconstruction. (d)-(e) Examples of cellular structures produced by electron tomography: (d) Segmentation from a tomogram of *Pyrodictium* and (e) a colored isosurface tomogram of two vesicles surrounded by carbon film. After [64].

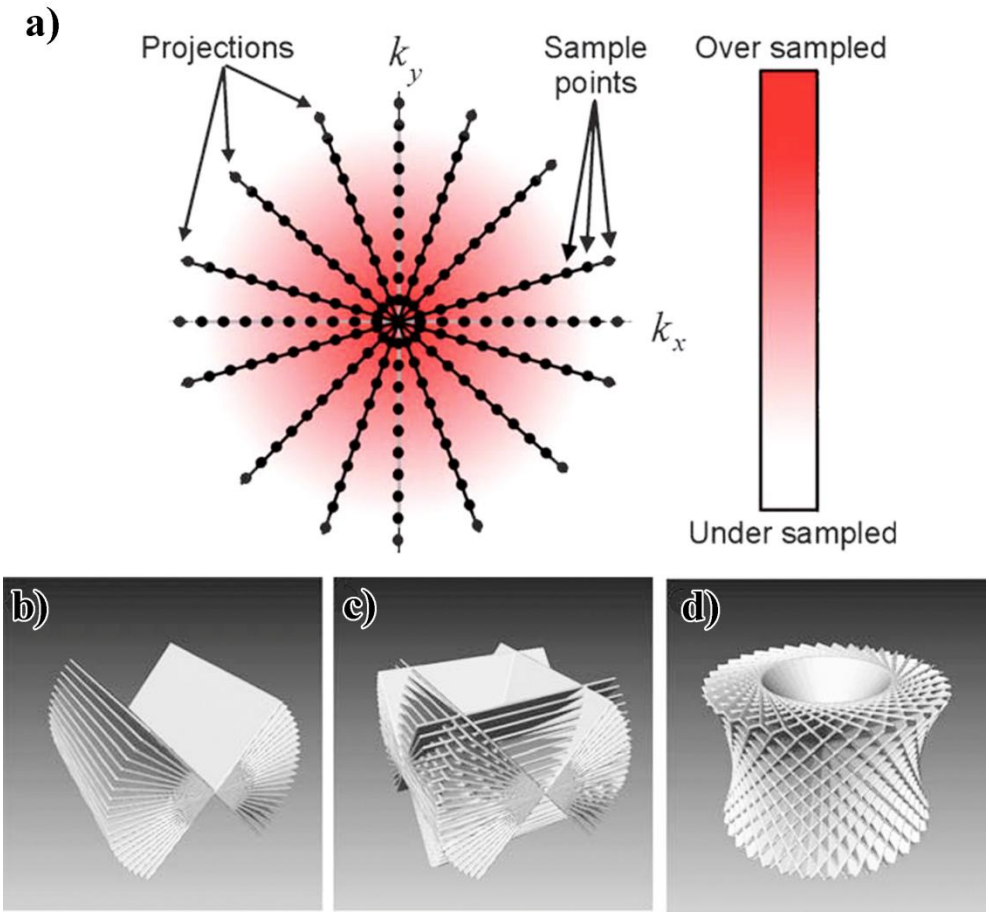

Fig. 2.20. (a) A schematic of the data sampling in Fourier space at different projections, illustrating oversampling at low frequencies and undersampling at high frequencies [74]. (b) The limit on tilt range restricts the available projections in single-axis mode to a fan-shaped sampling, (c) in dual-axes mode to a double-fan intersection, and in tilt-rotate mode to a conical sampling [64].

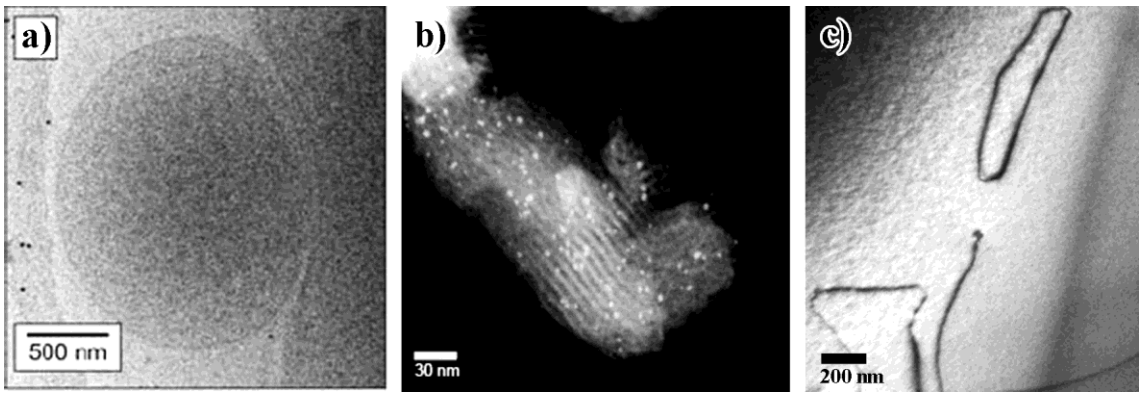

Fig. 2.21. Satisfying the projection requirement for tomographic tilt series images: (a) a *Thermoplasma acidophilum* cell imaged under mass-thickness contrast (bright-field TEM), (b) Pd_6Ru_6 nanoparticles in an MCM-41 mesoporous silica support imaged under Z-contrast (HAADF STEM) [64, 69], and (c) dislocation segments imaged under diffraction contrast (bright-field TEM).

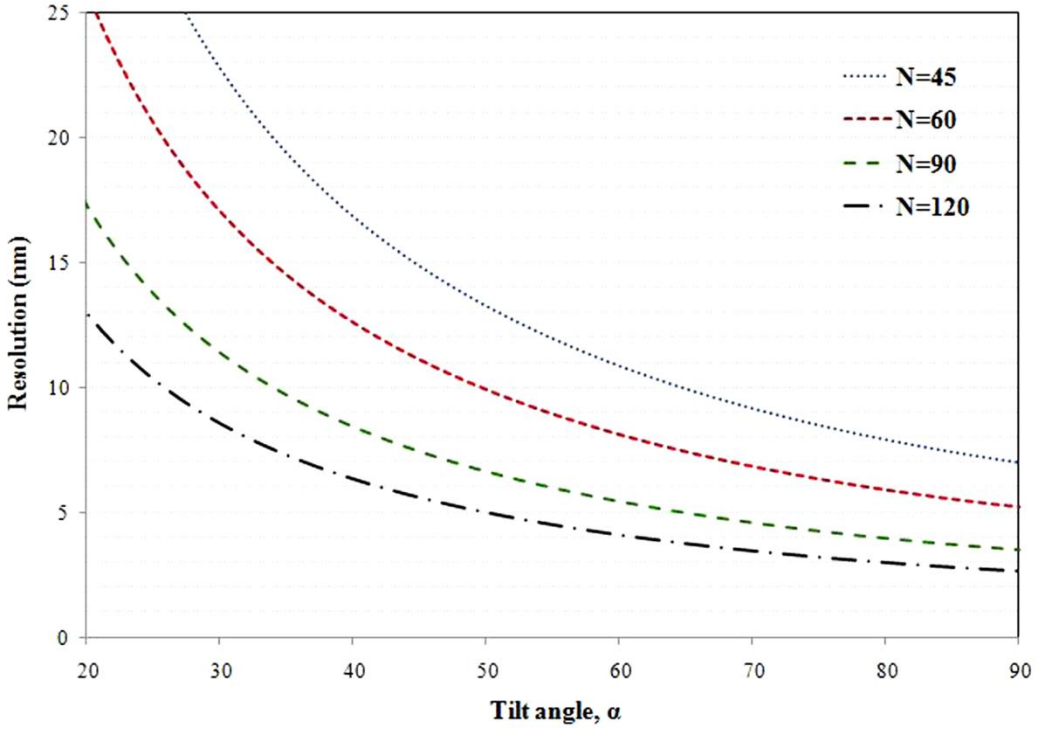

Fig. 2.22. Theoretical Z-resolution of a tomogram as a function of available tilt (half) angle, α, while varying the number of tilt series images, N. For typical tilt limit of ±40^{o} and tilt increment of 1^{o}, the best resolution obtainable is approximately 10 nm.

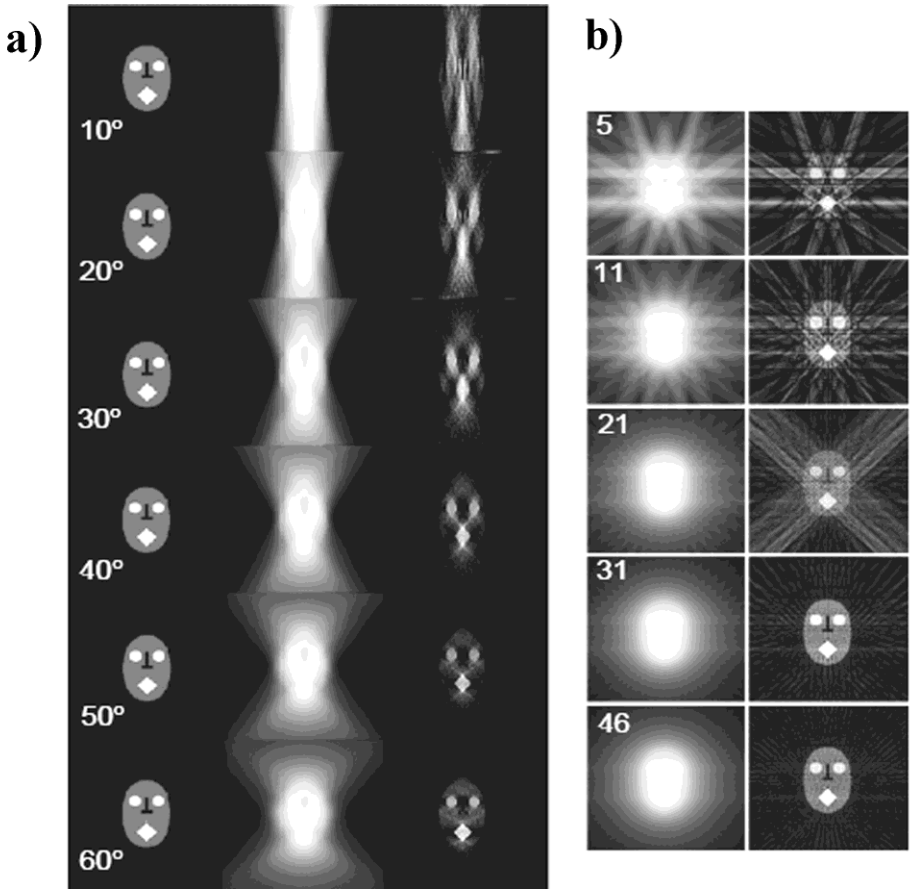

Fig. 2.23. A simulated dataset ("phantasm") illustrating the effect of (a) increasing tilt range shown in half-angle α (middle column: direct back-projection reconstructions; right column: weighted back projection reconstructions) and (b) increasing number of images acquired for α = 90° [69].

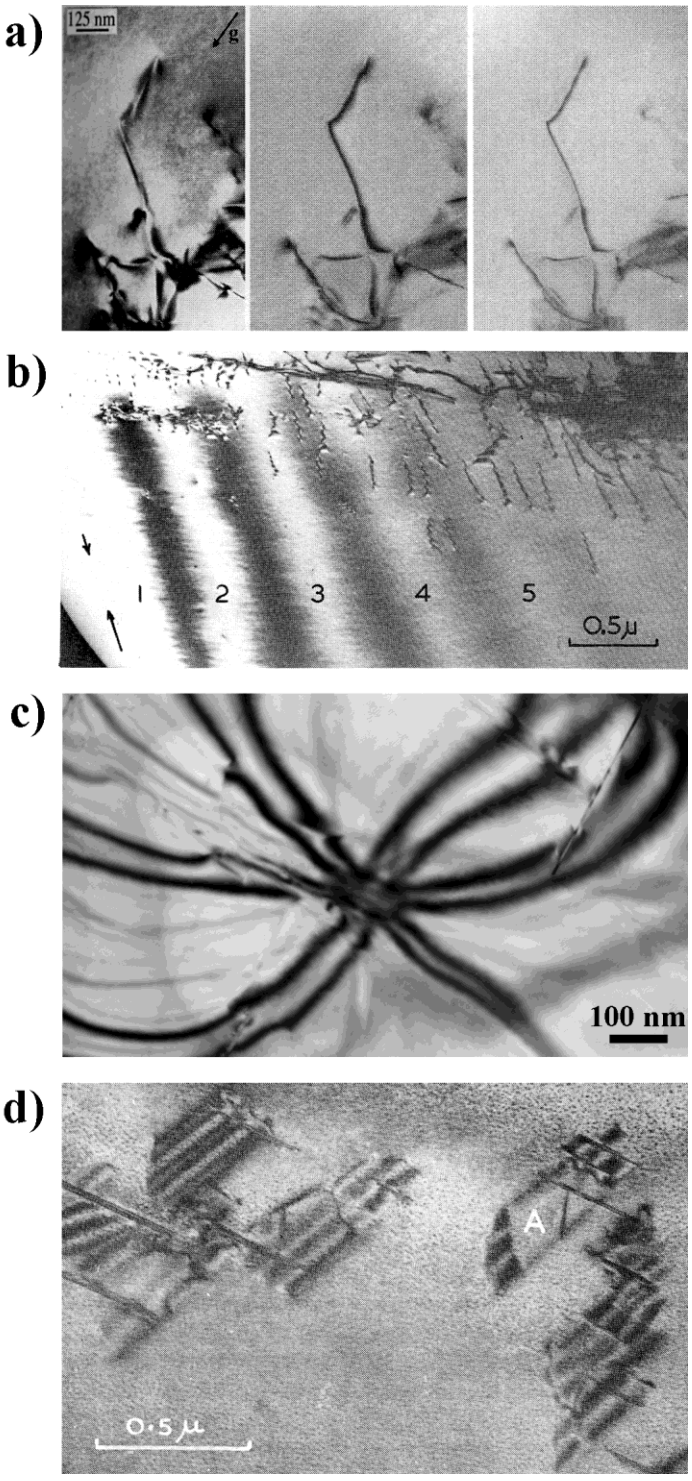

Fig. 2.24. Sources of contrast variation in diffraction-contrast imaging: (a) Variation in the Bragg deviation parameter, s (from left to right, s = 0, s > 0, s >> 0, respectively) [36], (b) thickness fringes near the electropolished hole, (c) bend contours, and in the case of plate-particles, (d) displacement fringes along the interface [73].

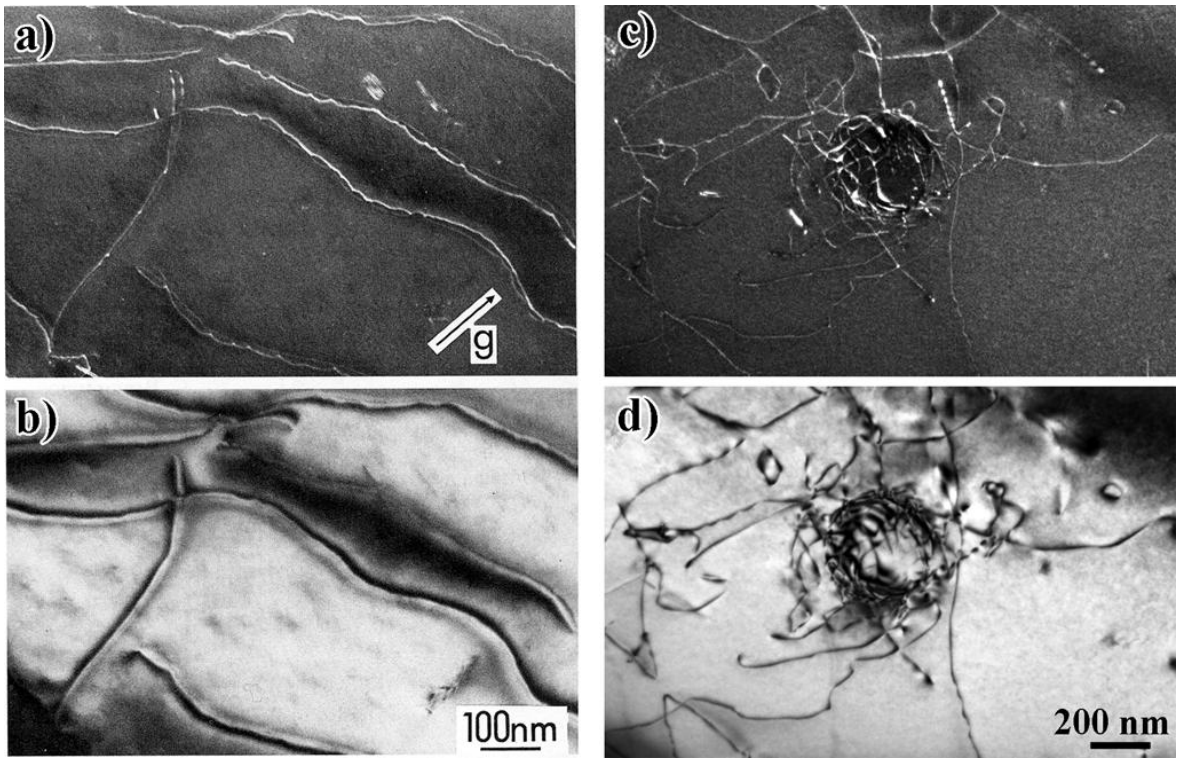

Fig. 2.25. A comparison of dislocation images formed using (a and c) weak-beam dark-field and (b and d) strong-beam (bright-field, $S_g > 0$) conditions in a Cu alloy [36], (a and b), and an Al_3Sc particle in an Al-Mg-Sc alloy surrounded by a network of lattice dislocations, (c and d).

CHAPTER 3

EXPERIMENTAL METHODS

This chapter is primarily concerned with two broad categories: the preparation of various alloys for post mortem or *in situ* TEM observation; and experimental and analysis methodologies for the interpretation and representation of results, including electron tomography. In the case of Al-4Cu and Cu-Co, a range of heat-treatments were carried out in order to determine conditions which produced particles most amenable to TEM imaging. All samples were mechanically thinned then jet-polished to achieve local electron transparency.

3.1 Sample Preparation for Transmission Electron Microscopy

3.1.1 Preparation of Al-Cu

Bulk Al-4%Cu and Al-4.5%Cu in the as-received condition were subjected to various heat treatments to optimize the precipitate density, size and coherency. A range of annealing temperatures (190^{o}C to 250^{o}C) and times (3 hrs to 10 hrs) were tested. The effect of varying the heat treatment temperature and hold time can be seen in the micrographs presented in Fig. 3.1. The average density of particles increased with annealing temperature whereas with increasing annealing time, the maximum particles size was increased. It was found that solutionizing at 493^{o}C followed by a salt-brine quench and annealing at 220^{o}C for 4.5 hours produced the most desirable microstructure. After heat treatment, slices ~400 μm thick were cut using a Buehler Isomet diamond saw as standard 3 mm-diameter discs, or *in situ* TEM straining bars measuring 10 mm x 3 mm or

11.5 mm x 2.5 mm. For the straining bars, approximately 300 μm-thick slices were cut from a rectangular bar with the appropriate cross-sectional dimensions, then super-glued to a grooved brass block where peg holes were drilled on either end, as shown in Fig. 3.2. The glue was dissolved with acetone and samples of both geometries were thinned to electron transparency by twin-jet polishing in an electrolyte of 25% nitric acid and 75% methanol at -28^{o}C and an applied voltage of 17V.

3.1.2 Preparation of Al-Sc and Al-Mg-Sc

As-received bulk Al-0.3Sc and Al-4Mg-0.3Sc were solutionized and heat- treated in an air furnace in order to obtain semi-coherent Al_3Sc particles. For the Al-Mg-Sc system, Mg remains in solution while Al_3Sc precipitates in the matrix. Homogenization for Al-Sc was carried out at 635^{o}C for 24 hrs followed by annealing at 450^{o}C for 5 to 5.5 days. Al-Mg-Sc samples were solutionized at 575^{o}C for 6 hrs, then annealed at 280^{o}C for 8 hrs. Bulk samples were reduced to smaller dimensions by cutting with a Buehler Isomet diamond saw and mechanical polishing with sand paper of progressively finer grit count. Electron transparency was achieved by twin-jet polishing in a 33% nitric acid and 67% methanol electrolyte at -28^{o}C and an applied voltage of 6V. The typical microstructure after heat treatment is presented in the micrographs shown in Fig. 3.3. The precipitate composition for each system is Al_3Sc, which has a $L1_2$ crystal structure and maintains semi-coherency with the aluminum matrix. TEM discs and straining bars were made in a similar manner as the Al-Cu samples, see section 3.1.1 and Fig. 3.2.

3.1.3 Preparation of Cu-Co

Cu-Co alloys of varying compositions (0.5 wt.% Co, 1.0 wt.% Co and 3.0 wt.% Co) were arc-melted from pure-metal pellets of 99.999% Cu and 99.9% Co. The arc-melting unit consisted of a custom-built vacuum chamber (see Fig. 3.4 (a)) with a water-cooled crucible and a tungsten electrode powered by a Miller high-frequency power supply operating at 200 Amps under 14 kPa of Argon gas. A range of heat treating conditions were explored, with an anneal at 800^{o}C for 5 hours following homogenization at 1000^{o}C being optimal. Fig. 3.5 presents the variation in microstructure as a result of varying annealing conditions—particle size and interfacial network complexity increase with longer annealing time and particle density increases with increasing annealing temperature accompanied by a slight decrease in *particle size.* 200 μm-thick slices were cut using a Hansvedt electro discharge machine and further thinned to around 150 μm using sand paper before jet-polishing in a 25% phosphoric acid and 75% water electrolyte at room temperature and an applied voltage of 10V. 3 mm diameter TEM foils and *in situ* straining bars were made following the same procedures as for the aluminum alloys (see previous sections). A number of discs were further thinned with a Gatan PIPS ion mill in order to obtain a larger electron-transparent region.

3.2 Conventional Imaging of Dislocation-Particle Interactions

3.2.1 Transmission Electron Microscopy

Imaging of the defect microstructures was performed on several instruments, all located within the Frederick Seitz Materials Research Laboratory at the University of Illinois, Urbana-Champaign: A JEOL 4000EX TEM operating at 200 or 300kV, a JEOL

2010 (LaB_6 filament) TEM operating at 120kV or 200kV, a JEOL 2100 (LaB_6 filament) TEM operating at 200kV, and a Philips CM12 TEM operating at 120kV. Although the displacement threshold for aluminum is around 180kV, effects of radiation damage from the electron beam were considered minimal due to the limited exposure time. Diffraction-contrast imaging techniques used included standard two-beam bright-field and centered dark-field techniques as well as weak-beam dark-field imaging for resolving more complex dislocation arrangements. High-resolution imaging was carried out using a JEOL 2010 (field-emission) TEM operating at 200kV. Micrographs and diffraction patterns were recorded using one of two methods. For recording with negatives, Kodak SO-163 electron image film was used, and were developed and fixed in a dark room following the TEM session. For digital recording, a Gatan MatScan 1k x 1k progressive-scan CCD camera was used in conjunction with the Digital Micrograph software on the JEOL 2010 (LaB_6) instrument and a Gatan UltraScan 2k x 2k CCD was used on the JEOL 2100 instrument.

3.2.2 In Situ *Straining Experiments in the TEM*

The capability to observe material responses to external stimuli such as an applied stress in real time inside the microscope requires the use of specially-designed TEM stages. The general configuration of these stages include a motor located at the back of the stage which drives a crosshead onto which one end of the straining bar is fixed, see Fig. 3.6(b)-(c). The crosshead speed is displacement-controlled via a control box and the bar is pulled in tension to induce dislocation motion in the electron transparent region. Movie capture for *in situ* experiments was performed using the MatScan CCD though a streaming feed to a video-capture software. Post-processing of videos often involved clipping, compressing

and adjusting the contrast levels and frame rates followed by re-encoding in the VirtualDub AVI video-editing software.

3.3 Three-Dimensional Imaging using Electron Tomography

One of the major components in this work has been the development of electron tomography to spatially resolve defect structures under diffraction-contrast imaging conditions. Section 2.6 outlined a number of practical difficulties which have hindered implementation of transmission electron tomography as a routine analysis tool. This section will describe a set of proven experimental practices which has become an established methodology for the application of electron tomography to investigate defect interactions in crystalline materials.

3.3.1 Tilt Series Acquisition

Images for tomographic tilt series were acquired with a JEOL 2010 (LaB_6 filament) TEM equipped with a high-resolution pole-piece with a gap width of approximately 5 mm. Using a JEOL Double-Tilt Analytical Stage (Fig. 3.6(a)), the standard maximum X-tilt range is -35^o to 35^o with the specimen translates and Z-height both near default positions. Since the through-thickness resolution of the reconstructed tomogram depends strongly on the angular tilt range (see Section 2.5), the acquisition angle was maximized by aligning the desired Kikuchi band with the X-tilt direction of the goniometer, as shown in Fig. 3.7, through manually rotating the sample until suitable alignment was achieved. The imaging condition was finalized by establishing the diffraction conditions, **g**-vector and the deviation parameter, **s**, through minimal use of the Y-tilt.

Alternatively, a custom-built Tilt-Rotate Stage (Fig. 3.8(a)-(b)) capable of an X-tilt range exceeding $\pm 53^{o}$ was also used. The rotational freedom for the sample was $\pm 90^{o}$ in-plane, essentially enabling alignment to any Kikuchi band present; but does not have Y-tilt capability. The rotation of the sample was controlled by two "chopsticks" which extended or retracted independently along the stage rod-axis, moving the sample—mounted inside a graphite "puck" holder (Fig. 3.8(c))—by variable capacitance output from a Kleindiek control box and a National Instruments Labview graphic-user interface. Detailed operations of the stage and peripheral equipment can be found in Appendix 1. Although the angular tilt range was greatly expanded compared to the JEOL Double-Tilt Analytical Stage, the lack of secondary, or Y-tilt of the Tilt-Rotate Stage ultimately placed severe restrictions on whether a tilt series could be acquired from a particular sample.

A completed tilt series typically consisted of 60 to 80 images recorded at uniform intervals of 1^{o} or 2^{o} X-tilt. The recording of dislocations and other crystal defects utilized diffraction-contrast imaging techniques such as kinematical bright-field (BF), centered dark-field (CDF) and weak-beam dark-field (WBDF). In all cases, contrast variations across tilt series images were minimized by maintaining the same magnitude of **s**. The three tilt series images presented in Fig. 3.9 demonstrate a common source of contrast variation—crystal bend contours—as the X-tilt value changes. Even though Fig. 3.9(a)-(c) were all imaged using the same **g**-vector, there is an extra dark band across the upper-center portion of Fig. 3.9(b) and across the lower-left corner of Fig. 3.9(c) when compared with Fig. 3.9(a). Proximity to a zone axis (multiple beam condition), crystal bending and increasing/decreasing sample thickness can all have significant influence on the image contrast which, for the angular range required, could not be avoided entirely. The

following sections will address methods to overcome these effects in producing the final 3D reconstruction.

3.3.2 Image Alignment and Reconstruction

After acquisition of the images that form the tilt series, they were aligned such that the jerky transitions between each image were minimized. Two computer programs were employed for aligning and reconstructing the image stack: *EM3D ver. 2.0*, by the McMahan Laboratory, Stanford University [75]; and *TomoJ ver. 2.12*, a plugin for *ImageJ* [76-77] image processing software, by Messaoudi et al. [78], Université Pierre et Marie Curie. EM3D utilizes the matching of fiducials, which are markers assigned to locations of significant contrast change from neighboring pixels, to align one image to the next in the sequence. A screen capture of a tilt series being aligned in EM3D is presented in Fig. 3.10(a), where the fiducials used for alignment are shown as asterisks in yellow and the fiducial number in red. It was found that although this operation could be performed automatically by the software, the resulting stack alignment was often poor. Some degree of semi-manual reassignment of the fiducials was usually necessary to induce sufficient transitional smoothness.

For image stacks with high contrast variations, pre-processing of the images could be performed to render fiducials or landmarks recognizable across all tilt series images. In TomoJ, for instance, the available options included: removal of saturated pixels, subtraction of background noise, increase in contrast, and image filtering. For most datasets, these processes were simply not necessary as the alignment was satisfactory; but were carefully verified to not alter the data represented when used. The goal was to produce a set of

images with consistent contrast, especially for features of interest, such that the majority of images in the dataset were well-aligned with each other. For recalcitrant datasets, full-manual alignment was performed with TomoJ by repositioning an image to a "best-fit" with the previous image via red/green image superposition, as shown in Fig. 3.10(b). As the current image (colored red) is manually repositioned over the previous image (colored green), overlapped regions appear black. The best fit is achieved when nearly no regions colored green or red can be seen.

Following alignment, the stack was back-projected (see Section 2.5.3) to yield a reconstructed tomogram that is a volumetric representation of the sample as imaged by the TEM. Such a volume consisted of 3D data points with varying intensities, representing the defect structures, as shown in Fig. 3.11 for quenched-in stacking-fault tetrahedra in Au. At this stage, spatial information could already be inferred from the volume; for instance the qualitative defect density of one region compared to adjacent regions, clustering of certain types of defects, whether two defect structures are located on the same slip plane…etc. Ultimately, however, spatial details could not be wholly resolved due to the loss of Z-direction resolution from the missing-wedge as discussed in Section 2.5.4. Sections 3.3.4 and 3.3.5 will describe techniques developed to overcome this challenge, and steps taken to obtain full 3D distribution of dislocations from the volume of interest.

3.3.3 Determining Crystal Orientation

While a reconstruction of the volume is useful in that spatial information is recovered, there still remains a need to correlate the reconstruction to the specimen's crystallographic directions and planes in order to analyze and interpret the data. This was

accomplished by recording pairs of images and diffraction patterns at known crystallographic zone axes repeated at a minimum of three zone axes. Since the reciprocal lattice vectors captured in the diffraction patterns are normal to the real-space planes in the micrographs, real-lattice directions are parallel to reciprocal lattice vectors bearing the same index. The method to identify crystallographic directions in three dimensions is an extension of this idea. Persistent features were identified in each image and with one designated as a reference point, the distances between the reference and each of the remaining points were determined, the ratios between these distances were calculated, and the angles made by the vectors connecting the markers were measured and tabulated. Utilizing a procedure similar to constellation matching, the tomogram was rotated until a match with the projected vector ratios and angles was found. The lattice directions indicated in the corresponding diffraction pattern are now parallel to their projections on the viewing plane. Thus, it is possible to position the real space coordinate system in the tomogram. To determine the accuracy of the proposed method, the coordinate system as determined by the proposed approach was compared with known specific directions in an image. Stacking-fault tetrahedra provided an effective reference system since they are three-dimensional vacancy defects formed from {111} planes with the plane intersections lying along <110> directions. Consequently, it is possible to introduce a coordinate system from images of stacking-fault tetrahedra.

A field of stacking-fault tetrahedra was created in Au [50] by quenching from 400^{o}C and annealing at 1040^{o}C. Images of tetrahedra from different beam directions but with the same diffraction condition are shown in Fig. 3.12(a)-(c). The change in the projected shape as the viewing direction changed is obvious. Images, along with

diffraction patterns, were acquired at beam directions near the [011] zone, the [001] zone, and the $[0\bar{1}1]$ zone, respectively; and the coordinate system introduced in the form of a Thompson tetrahedron into the tomogram, Fig. 3.12(d)-(e). From comparison of the directions with the Thompson tetrahedron and those of the projected images, it was determined that the accuracy of positioning the Thompson tetrahedron in the tomogram was less than 5^{o}, which considering the errors associated with the method is reasonable. Moreover, it is sufficient for the intended purpose of identifying slip planes and line directions of dislocation structures.

3.3.4 Data Visualization & Representation in 3D-Traced Models

While tomograms are capable of approximately representing dislocations as lines with varying thicknesses, viewing along all directions were often necessary in extracting crucial information such as active slip planes and line directions. As described in more detail in Section 2.5.4, the tomogram resolution in the X- and Y-directions has an upper limit equal to the resolution of the micrographs. Assuming a maximum half-angle of 40^{o}, the nominal resolution in the Z-direction is equivalent to the X-Y resolution reduced by an elongation factor of 2.4[64]. With a resolution limit of approximately 5-6 nm for a (**g**, 3**g**), **g** = 020 pseudo weak-beam dark-field image, the Z-resolution is estimated to be $\geq$ 14 nm [79-80]. In order to enhance the tomogram's effective resolution, a technique was developed to produce a dislocation structure model by tracing, in 3D, the dislocation lines in the tomogram using prior knowledge about dislocations and dislocation image formation using diffraction-contrast imaging conditions. The finished model contained all the spatial

information of the tomogram without suffering from the reconstruction artifacts. Furthermore, by using the molecular visualization software *Chimera ver. 1.5*.3, developed by the Resource for Biocomputing, Visualization, and Informatics, University of California, San Francisco [81-83], the model could elucidate and emphasize relevant fundamental processes for understanding dislocation-particle interactions in alloy systems.

The 3D tracing of dislocation lines was done by placing linked spherical markers in the tomogram, usually first from a nearly Z-normal view. The tomogram was then rotated to near X- and Y-normal views and the current marker was repositioned accordingly, repeating for all markers in the same group and finally, for all other dislocations or defects present. The accuracy of this preliminary trace was verified constantly by checking for spatial consistency from multiple vantage points. Toolsets in Chimera were also used to construct visualization tools highlighting salient features and morphologies in the dislocation structure model: color of dislocations based on Burgers vector, location, or type (e.g. interfacial or matrix, and perfect or partial), opacity of objects to elucidate spatial relationships…etc. An example of these capabilities is presented in Fig. 3.13 for dislocation structures created near a crack tip in Si [84].

3.3.5 Dual-Axes Electron Tomography

When using diffraction-contrast imaging in conjunction with electron tomography, a notable challenge is that some defects are excluded from the reconstruction as only one diffraction vector is used to acquire the image. Dislocations satisfying the $|\mathbf{g} \cdot \mathbf{b}| = 0$ criterion, for example, would be invisible and therefore not represented in the final

tomogram. To remedy this problem, dual-axes electron tomography was developed such that information from two **g**-vectors is encompassed in one final dislocation model.

An example illustrating the effectiveness of this method is presented in Fig. 3.14 for matrix dislocations and Co-rich particles in a Cu-Co system. Unlike previous dual-axes tomographic studies where subcellular structures were reconstructed from two *orthogonal* tilt series [85-87], the tilt axes for a crystalline specimen are often not orthogonal—in this case, $\mathbf{g_1} = \bar{2}20$ and $\mathbf{g_2} = 0\bar{2}0$, which are 45^o apart. Note that tomographic reconstruction programs written for biological applications such as EM3D assume the two tilt axes are 90^o apart and dual-axes data from non-orthogonal series cannot be reconstructed by the programs directly. Thus the first and second tilt series were reconstructed separately to make individual tomograms then combined to produce the dual-axes tomogram by manually superimposing the two volumes together using the Chimera software. The dual-axes tomogram was used to construct a dislocation structure model as described in Section 3.3.4, shown in Fig. 3.13(c). Those dislocations visible only under $\mathbf{g_1}$ are colored in blue; those visible only under $\mathbf{g_2}$ are colored orange; and those visible under both $\mathbf{g_1}$ and $\mathbf{g_2}$ are colored green. If $\mathbf{g_2}$ alone was used to obtain a single-axis tomogram, only the dislocations in orange and green would be represented—and all those colored blue would be missing. It can be seen that given prudent selection of **g**-vectors, dual-axes tomography can ensure that all relevant microstructural features are recorded and represented in the model.

3.4 Figures

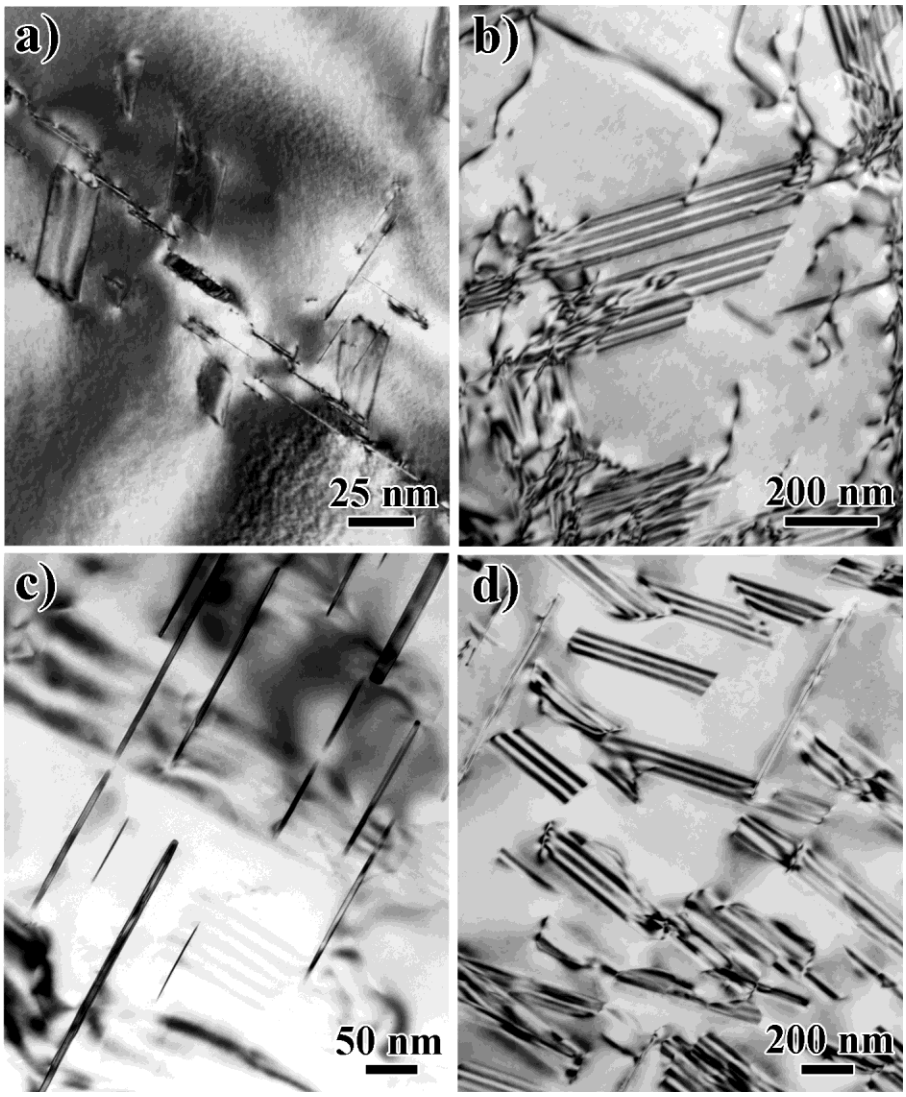

Fig. 3.1. Microstructure as a function of annealing temperature and hold time for Al-Cu: (a) Al-4%Cu annealed at 190°C for 7 hrs; (b) Al-4.5%Cu annealed at 220°C for 4 hrs; (c) Al-4%Cu annealed at 190°C for 10 hrs; and (d) Al-4%Cu annealed at 220°C for 5 hrs.

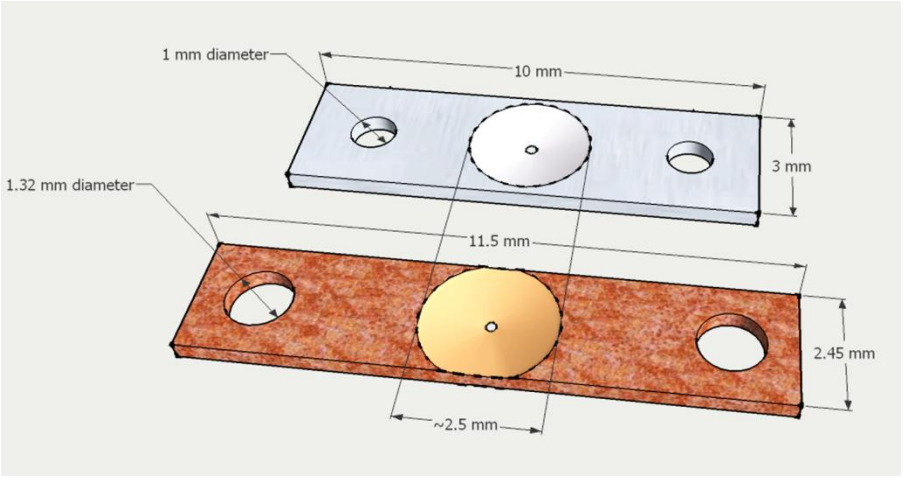

Fig. 3.2. ***In situ*** **TEM straining bar geometries. Top: for a custom-built room-temperature TEM straining stage; Bottom: for a standard room- or high-temperature TEM straining stage manufactured by Gatan, Inc.**

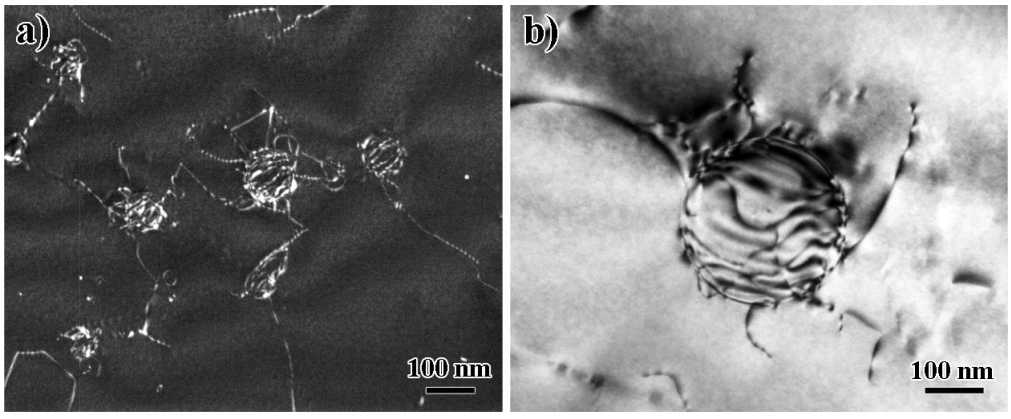

Fig. 3.3. Microstructure of (a) Al-0.3Sc solutionized at 635^{o}C for 24 hrs and annealed at 450^{o}C for 5 days, and (b) Al-4Mg-0.3Sc solutionized at 575^{o}C for 6 hrs and annealed at 280^{o}C for 8 hrs.

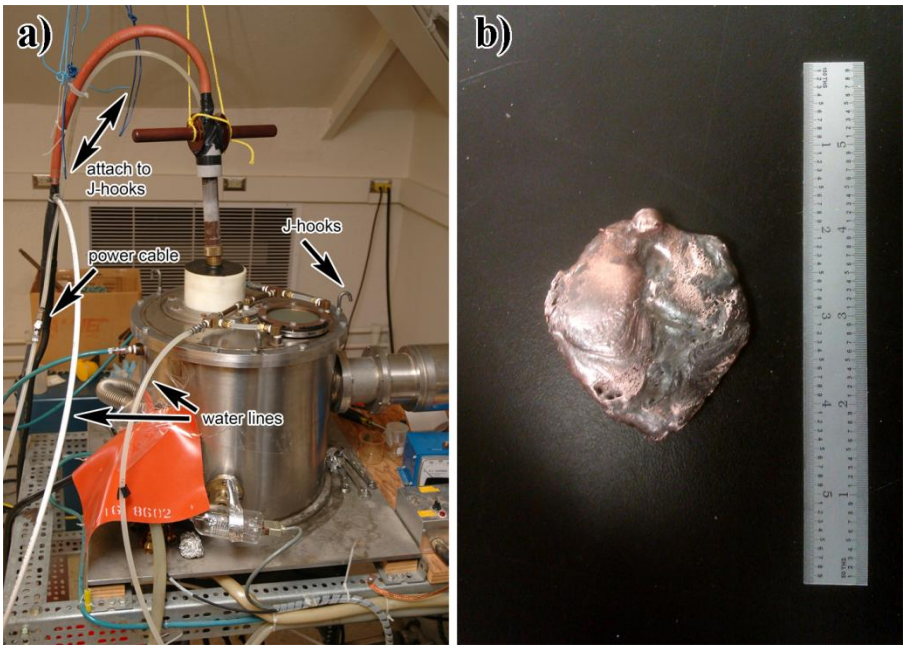

Fig. 3.4. External view of the arc-melter unit, (a); and the typical dimensions of an arc-melted custom alloy ingot, (b).

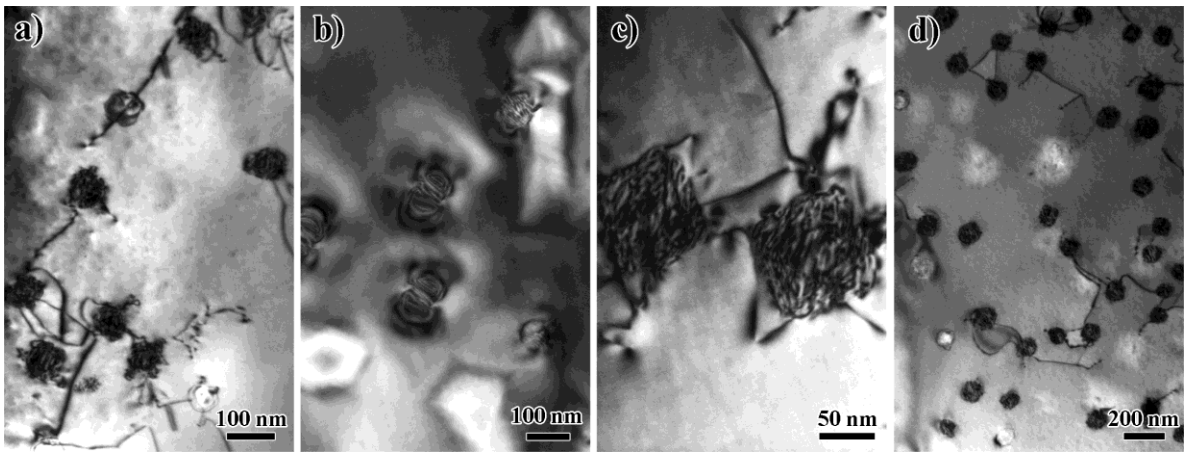

Fig. 3.5. Microstructure of Cu-3%Co homogenized and annealed for (a-b) 5h at 800^{o}C, where some local regions had semicoherent particles while other regions retained coherent particles; (c) 10h at 800^{o}C, with particles being larger accompanied by complex interfacial structure; and (d) 5h at 850^{o}C, with higher particle density compared to (a) and (b).

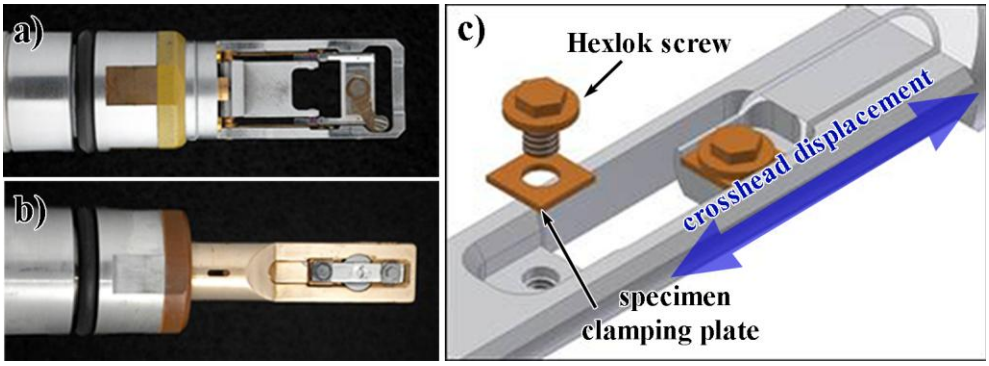

Fig. 3.6. (a) JEOL Double-Tilt Analytical Stage. (b) Gatan *in situ* straining stage with heating capability [88]. (c) Schematic drawing of an *in situ* straining stage, showing the configuration of the recessed bay housing the straining bar and crosshead pegs onto which the bar is affixed. See also Figs. 3.2 and 3.8 for comparison.

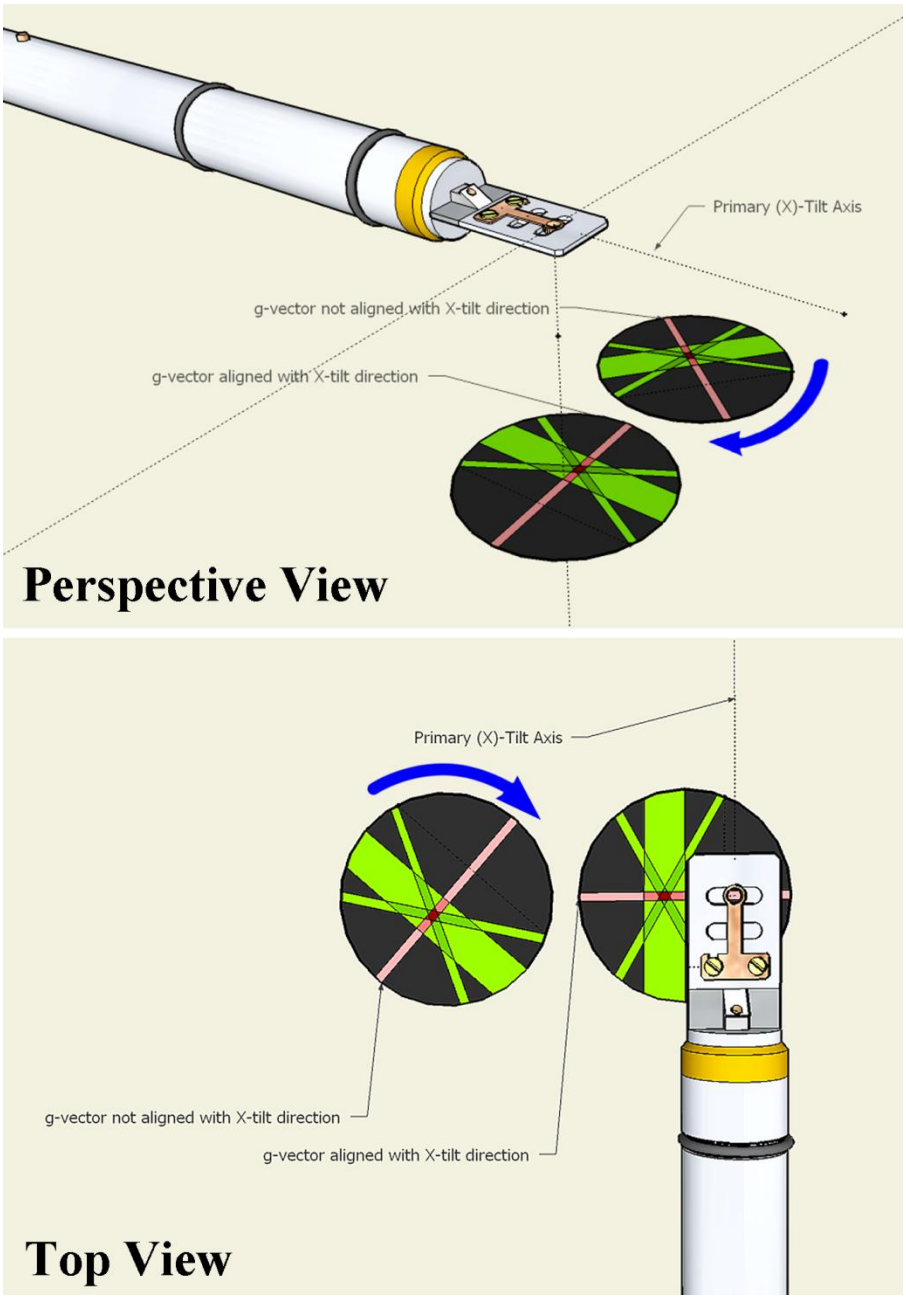

Fig. 3.7. Aligning the Kikuchi band (colored red) with the TEM goniometer's X-tilt direction. Note that as X-tilt is increased or decreased, traversing along the Kikuchi band, both the diffracting vector, g, and the deviation parameter, s, should remain constant.

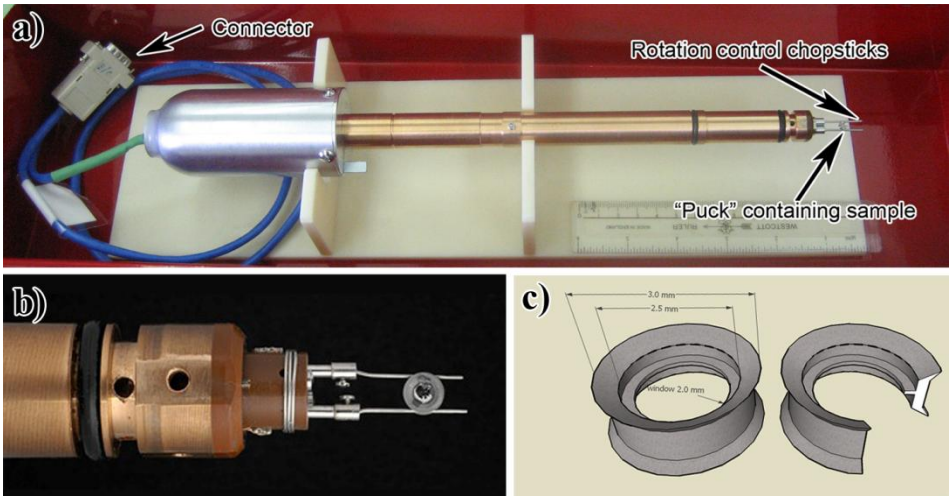

Fig. 3.8. (a) A custom-built thin-tip Tilt-Rotate Stage capable of high tilts. (b) The electron beam is aligned with the stage's zero position and equivalent but opposite displacement of the "chopsticks" rotate the sample, mounted in a graphite toroid "puck," (c). For details on their operation, see Appendix B.

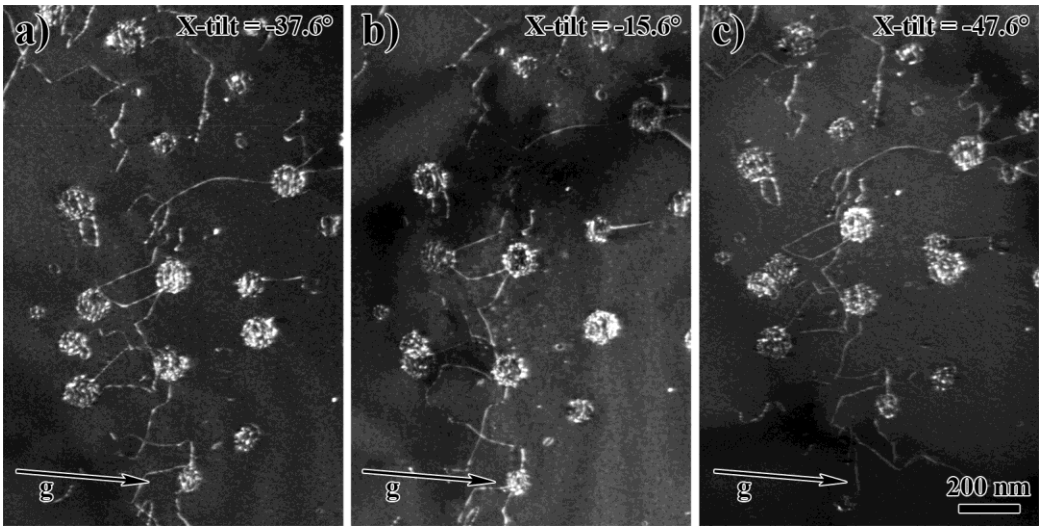

Fig. 3.9. Three images from a tilt series of a complex dislocation network around particles in Al-0.3Sc, demonstrating typical contrast variations with the same g at different tilt angles: (a) Reference image, showing uniform background contrast; compared with (b), showing multi-beam effects near a zone axis and (c), showing crystal bend contours. Contrast variations greater than that between (a, b) and (a, c) are often detrimental to the resolution of the tomogram.

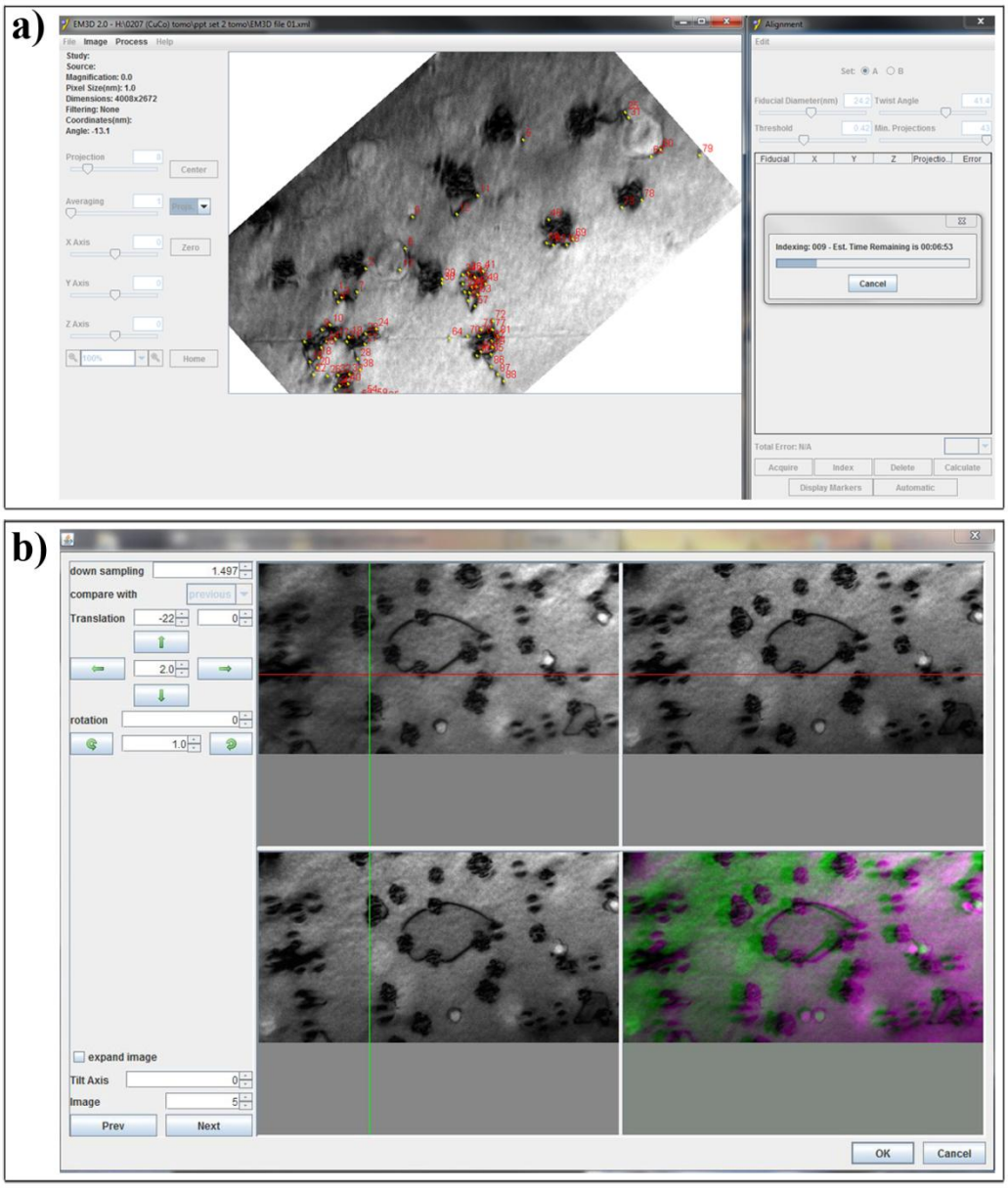

Fig. 3.10. (a) The alignment of a tilt series using EM3D software [75], where fiducials are shown as asterisks. By changing the *Fiducial Diameter* and *Threshold* settings, tolerances to contrast variations could be adjusted, relocating some existing fiducials. (b) Full-manual alignment of a tilt series using TomoJ [78], where an image is aligned with the previous image in the sequence using red/green superposition.

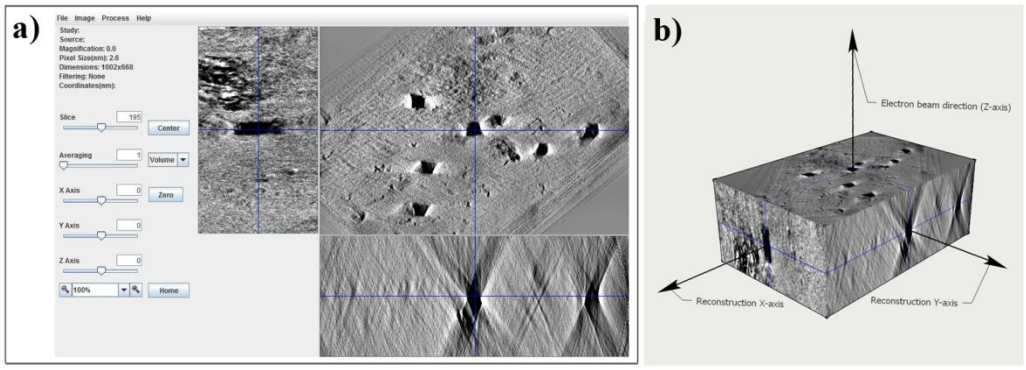

Fig. 3.11. (a) Weighted back-projection of the aligned tilt series produces a reconstructed volume using EM3D. In this case, the same quenched-in stacking-fault tetrahedra in Au foil as shown in Fig. 3.12. Clockwise from upper right are reconstructed volume slices: X-Y, X-Z, and Y-Z, respectively. (b) Schematic of the reconstructed slab.

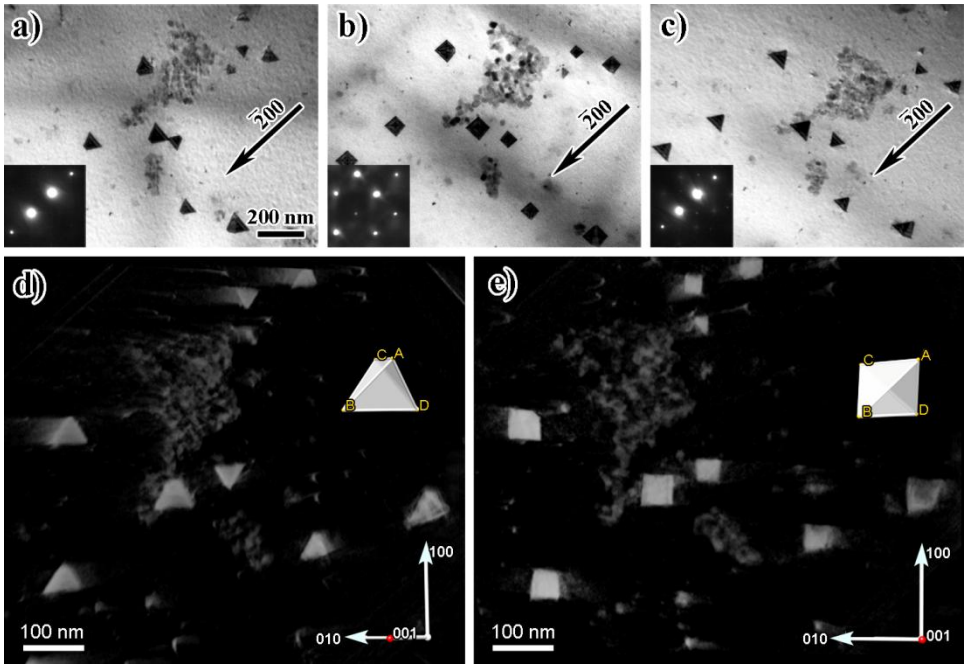

Fig. 3.12. (a-c) Change in the projected image of stacking fault tetrahedra in Au for the same diffraction vector but different beam directions. Beam directions are near [011], [001] and [0$\bar{1}$1] for images (a), (b) and (c), respectively. (d-e) select snapshots of the tomographic reconstruction of the tetrahedra, showing the projected shape along with a Thompson tetrahedron inserted based on a constellation matching method. The [001] direction, marked with a red dot on the coordinate axes, is coming out of the page at approximately 45^{o} in (d) and 90^{o} in (e). [50]

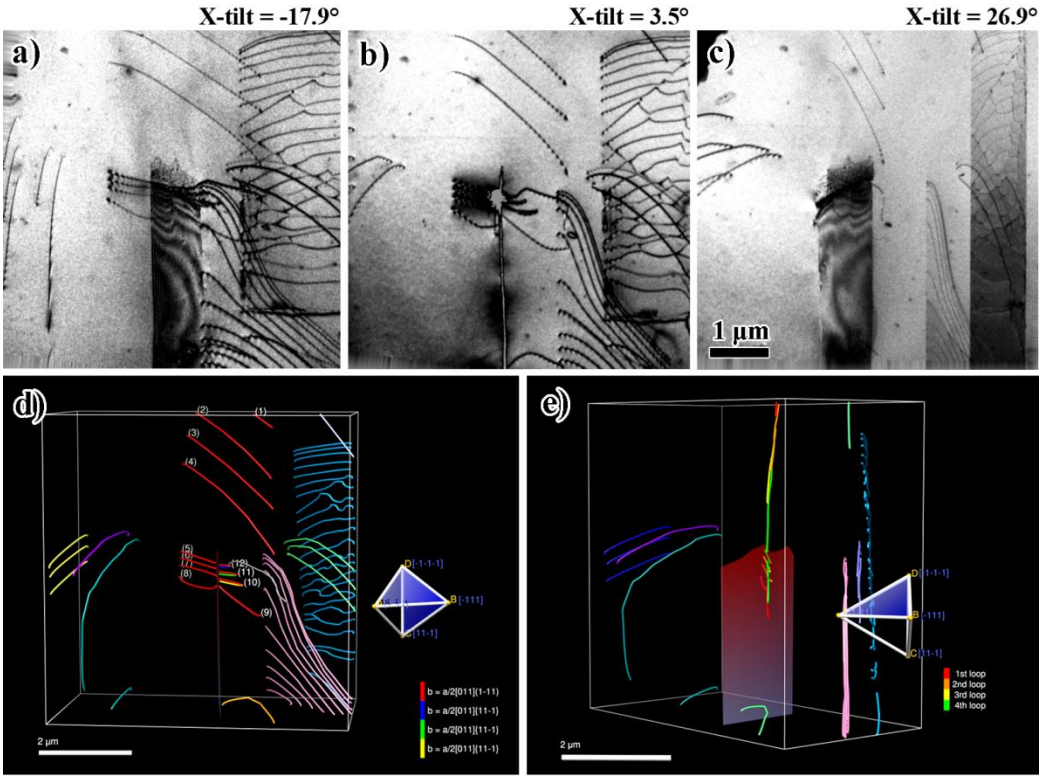

Fig. 3.13. Visualization capabilities in traced dislocation structure models for dislocations surround a crack in Si [84]. (a-c) Select images of the tilt series from which a reconstruction and traced dislocation model were produced. (d) A near-[001] view of the dislocation model, colored by slip-plane. Initially on the $(1\bar{1}1)$ plane, the crack-tip dislocations (colored red) have cross-slipped segments now residing on parallel $\{11\bar{1}\}$ planes (colored blue, green, and yellow). (e) A $[\bar{1}12]$ view, where the $(1\bar{1}1)$ plane is edge-on as clearly shown by the embedded Thompson tetrahedron; slip-planes on which individual dislocations reside can be unambiguously determined.

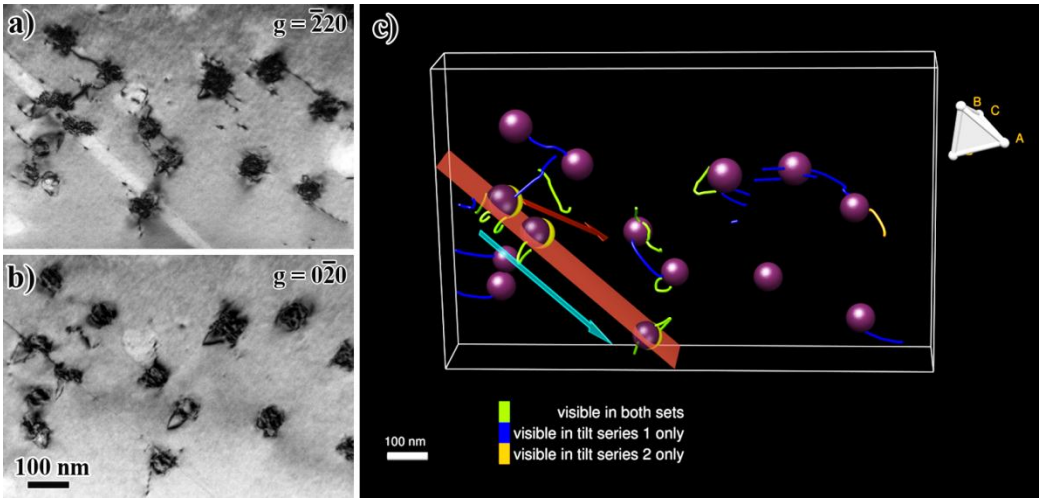

Fig. 3.14. Overcoming $|\mathbf{g} \cdot \mathbf{b}| = 0$ invisibility by dual-axes electron tomography. Tilt series were acquired from two different g-vectors, (a) $\mathbf{g}_1 = \bar{2}20$ and (b) $\mathbf{g}_2 = 0\bar{2}0$, which were then used to produce (c) the dual-axes dislocation structure model encompassing all dislocations imaged using $\mathbf{g}_1$ and $\mathbf{g}_2$.

CHAPTER 4

RESULTS

Several alloy systems with different types of particles were investigated, primarily by use of transmission electron microscopy (TEM) with diffraction-contrast imaging or a combination of techniques involving TEM. These include *post mortem* studies of deformed microstructure, *in situ* deformation experiments carried out inside the microscope to obtain time-resolved interaction information, high-resolution electron microscopy (HREM) to discern atomic-resolution arrangement of particle-matrix interface structures, and diffraction-contrast electron tomography to acquire spatially-resolved information about the dislocation-defect interactions. Results from *in situ* straining experiments are represented by still images which capture salient features of the interactions; and results from electron tomography are represented by select images of the original tilt series and illustrative views of the reconstructed tomogram/dislocation model produced from the series. Combining information obtained from all three analysis techniques provides details and instructive insights into the operative mechanisms during the dislocation-particle interactions.

4.1 *In Situ* Straining Experiments Involving Different Particles

Observations of lattice dislocations interacting with particles of different characteristics such as geometry, size, coherency and interfacial configuration, were performed at ambient temperature in real time inside the microscope in order to follow and elucidate the evolution of the microstructure under an applied tensile stress. In all cases, *in situ* experimental results were captured using a video recording charge-coupled device with

nominal frame rate of 30 frames sec^{-1} and presented with corresponding time stamps.

4.1.1 Dislocation Interactions with Al_2Cu Platelet Particles in Al-Cu

The Al_2Cu platelet particles were Guinier Type I, that is, having the orientation relationship $[100]_\theta \,||\, [\bar{1}01]_{Al}$ and $[001]_\theta \,||\, [010]_{Al}$. Unlike Al_2Cu particles [89-93] of the Vaughan Type II [42, 49] variety, which have orientation relationship $(\bar{1}10)_\theta \,||\, (111)_{Al}$ and $[111]_\theta \,||\, [1\bar{2}1]_{Al}$, the θ-plates studied in this work reside on $\{100\}$ planes and have an incoherent interface along the narrow side and a coherent interface along the broad side. Further analysis of the particle geometry will be discussed in terms of high-resolution images of the θ-matrix interface in Section 4.3.

Fig. 4.1 shows a series of such platelets, labeled "A1," "A2"… "A5" in front of a dislocation pile-up emitted from a crack-tip (located to the lower-left of each image but not shown) captured during an *in situ* straining experiment. This was the initial stage of deformation in this region, as no dislocations activity was detected prior to recording of the video. In Fig. 4.1(a), the arrow at particle "A2" indicates that the dislocations have bypassed the first platelet, which was immediately ahead of the advancing crack. The arrow also indicates the direction of dislocation motion. Though crosshead displacement continued to be applied between Fig. 4.1(a) and (b), platelet "A2" was not overcome easily—indicating that θ-plates were strong obstacles to dislocation glide even along the coherent interface. Eventually, the array of dislocations succeeded in overcoming "A2" and was once again arrested at the next particle, now "A3." The elapsed time between Fig. 4.1(a) and the passage of the *first* dislocation that sheared particle "A2," was less than 0.04

seconds, one video frame, indicating a fast process. Throughout the video, both dislocations as well as slip traces were visible and were consistent with dislocations gliding very rapidly in the inter-particle region but halted when they encountered a particle. This slip-and-stop process was repeated for particles "A3" and "A4," as can be seen in Fig. 4.1(d)-(e) with a total elapsed time of 1 second before a dislocation pile-up formed at precipitate "A5." This lasted for 26 seconds with increasing load followed by the bypass of "A5," Fig. 4.1(f).

The interactions are represented in Fig. 4.1(g), which shows the locations of the particles "A1" to "A5" in blue, with the portion experiencing dislocation activity colored green and the area in between parallel arrows corresponding to dislocation activity in the matrix. Thus, the region in between the parallel set of arrows spanning "A1" and "A2" corresponds to the extent of shear of particle "A1" and similarly for the other particles. The non-parallel set of arrows denote cross-slip of a number of dislocations originally between "A1" and "A2"; however, none of these dislocations ended up shearing the particle. All of the observed dislocation-particle interactions shared two key features: (1) The mechanism of bypass in each case was particle-shearing on the coherent side of the platelets; (2) The location where each particle was first sheared did not align with the location where the previous particle had first been sheared. The latter observation suggests that a sufficient local stress was required in order to shear the particles, as a certain number of impinging dislocations accumulated at the interface until a slip plane on the other side of the particle experiencing the highest level of resolved shear stress reached the required stress level. The offset in the shearing locations between successive particles may be attributed to an uneven distribution of particles in the foil and the local interface structure where the

dislocations have piled up. On average, 18 dislocations were accumulated at each particle prior to it being sheared with the number of dislocations required decreasing for successive particles, which is consistent with the stress state of a region in front of a lengthening crack.

After *in situ* straining, the propagation of the crack tip into the foil could be seen in Fig. 4.2 where the first particle, "A1," is marked by arrowheads. The crack appears to have advanced through a region (area "C") in the matrix with a low or near-zero concentration of θ-plates. Around the electropolished hole, some smaller cracks have experienced deflections in the crack path similar to Fig. 4.13. These deflections, in some cases taking 90^{o} turns, and the fact that the crack in Fig. 4.2 traveled between regions of higher particle concentration, also imply that θ-plates are strong barriers. The slip traces labeled "B" show a predominance of those parallel to the primary slip direction corresponding to dislocations seen in Fig. 4.1. When they encountered particles "A1" to "A5", the array of dislocations likely had the same Burgers vector, prior to successive and multiple shearing of the platelet particles.

It was also observed that once arrested at the particle, the stress on the leading dislocation can push it into the particle-matrix interface where it undergoes glide in the interface plane. Fig. 4.3 shows frames from an *in situ* straining video during which a number of matrix dislocations impinged on an Al_2Cu particle, then moved from left to right in the particle interface. The arrows in Fig. 4.3(a) indicate the directions of dislocation motion and the arrowheads denote the farthest position along the particle interface traveled by the array of dislocations. In Fig. 4.3(a)-(b) and (b)-(c), the dislocation motion was sporadic and rapid with long pauses followed by dislocations jumping ahead within one video frame (0.04 s). Eventually, interfacial glide was halted, Fig. 4.3(d)-(f). It can be seen

from Fig. 4.3(d)-(f) that new dislocations continued to enter the interface leading to an increase in dislocation density along the particle but ultimately they proved insufficient for continued glide in the interface due to either loss of dislocations by shear of the particle or from some kind of obstacle ahead of the dislocation array.

With sustained deformation, eventually multiple slip systems were activated as local stress levels increased. Fig. 4.4(a) shows a different particle viewed from the broad side with an array of dislocations gliding inside the particle-matrix interface. Note that the θ-plates did not extend from the top to the bottom foil surface (confirmed by tomographic reconstructions, see Section 4.4) but instead terminated in the interior of the foil. Therefore the dislocations seen moving in the interface in Figs. 4.3 and 4.4 were indeed confined to the particle interface and did not extend between the foil surfaces. The particle's upper and lower (broad-side) interfaces are marked with white lines for clarity in Fig. 4.4(a) and (f). Instead of being arrested like those in Fig. 4.3, however, these dislocations were able to glide until they reached one end of the plate, Fig. 4.4(b). No dislocation pileup was formed at the end of the particle. Instead of increased dislocation density, these dislocations exited the interface and were swept out of the foil by cross-slip away from the particle. Since no apparent change in the projected dislocation line length was detected just prior to cross-slip, the particle likely resided close to the foil surface. Fig.4.4(a and c) and (d and f) show difference images formed by superimposing a negative image (dislocations being white) onto a positive image (dislocations are black). In this case frames (a) and (d) were inverted and superimposed on positive images of (c) and (f). Dislocation movement can be tracked by comparing the relative positions of the dislocations in white versus those in black—which clearly shows that no prolonged increase in dislocation density in the array occurred.

This observation suggests that where sufficient driving force is present, glide in the particle interface will proceed forward until multiple arrays of dislocations impinge on the same particle and mutual interaction renders glide in other particles more favorable.

During the *in situ* TEM deformation experiments, the classical Orowan looping mechanism or simple particle shearing was not observed. It is noted, however, that the displacement experienced by the particle via single shearing events is equal only to the magnitude of the Burgers vector of the dislocations, in the case of aluminum $|\mathbf{b}| = 2.9 \times 10^{-10}$ m. In many cases, such reactions would be too small to detect—it is only when a number of similar dislocations have gone through that the disruptions in the interface become of sufficient magnitude to be discernable. Observations of the microstructure at later stages of deformation will be presented in Sections 4.2 and 4.4.

4.1.2 Dislocation Interactions with Spherical Al_3Sc Particles in Al-Mg-Sc

Unlike the anisotropic Al_2Cu plates, the particles in Al-Mg-Sc are spherical and have uniform coherency throughout the particle-matrix interface. Fig. 4.5 shows an example of a dislocation interacting with a small semi-coherent Al_3Sc particle at room temperature. After bowing around the particle, Fig. 4.5(a), the upper portion of the dislocation segment interacted with the interface causing a change in the interfacial contrast, Fig. 4.5(b)-(d). The black dots in the particle interface, indicated by the arrowheads, were thought to be small loops which were subsequently swept up as the upper dislocation segment moved across the particle. Both the upper and lower segments of the dislocation continued to bow around the particle, Fig. 4.5(e), eventually breaking free and leaving a single dislocation loop attached on one side to the particle, Fig. 4.5(f) [17]. This type of

loop creation is distinct from classical mechanisms involving Orowan looping, in which the loop surrounds the particle at a standoff distance. It is also different from a loop created by the Hirsch mechanism, as this also produces (prismatic) loops to one side of the particle. Instead, bypass of the particle occurred by dislocation cross-slip, with one segment still attached to the interface. Notably, loops of a similar configuration were also found in *post mortem* and electron tomographic observations of Al_3Sc particles—indicating that the creation of an attached half-loop as a result of cross-slip bypass of semi-coherent spherical particles occurs regularly. The details of these observations will be discussed in Sections 4.2 and 4.4.

4.1.3. Dislocation Interactions with Octahedral Co Particles in Cu-Co Alloys

Like Al_3Sc particles, the Co-rich particles in the Cu-Co system were also heat treated to be semi-coherent, but were able to retain coherency to large particle sizes due to the similarity in lattice parameter between Cu and (FCC) Co, 3.62×10^{-10} m and 3.55×10^{-10} m, respectively. Although the room temperature crystal structure of Co is normally hexagonal close-packed, when alloyed in small quantities with Cu the face-centered cubic structure is preferred and the particle shape is expected to be faceted, conforming to $\{111\}_{Cu}$ for incoherent particles [94-96]. For *in situ* experiments, however, both the dense interfacial contrast as well as the relatively small size of the particles rendered visualizing the faceting of the particles unfeasible.

The complexity of the Co particle interface, however, does indicate the presence of a densely-distributed interfacial dislocation network; and its interaction with dislocations, at least in the initial stage, was observed to be elastic. An example of this kind of interaction

is presented in Fig. 4.6, where two dislocations belonging to the same slip system impinged on a Co particle during an *in situ* straining experiment. In this early stage of deformation, the leading dislocation, labeled "1," experienced a repulsive interaction with the strain field of the particle, Fig. 4.6(a) for around 7 seconds before eventually contacting the particle interface. The upper portion of dislocation "1" immediately cross-slipped (arrowhead, Fig. 4.6(b)) but the lower segment remained on the original slip plane for more than 2 minutes, Fig. 4.6(c), before the applied tensile stress pushed dislocation "2" towards the particle and the lower segment of "1" was accommodated into the particle interface, Fig. 4.6(d). A new dislocation labeled "3" moved into view in Fig. 4.6(e) under sustained application of stress but did not cause dislocation "2" to undergo the same interaction as that experienced by dislocation "1." Instead, interaction with dislocation "3" was elastic, causing an existing dislocation segment spanning between the primary particle and a neighboring particle, Fig. 4.6(e)-(f), to rearrange and partially break free, Fig. 4.6(g). Eventually, bypass occurred by cross-slip around the particle, Fig. 4.6(h), where the upper segment of dislocation "3" has cross-slipped back onto a slip plane parallel to the initial slip system. We see that since dislocations "1"-"3" originated in the thinner region of the sample devoid of Co particles, the elastic interaction illustrates the collective strength of the particle field in the thicker regions; and dislocation debris left in the particle interface may also enhance these elastic interactions.

In addition to bypass via cross-slip, dislocations interacting with Co particles were also observed to involve a dislocation loop surrounding the particle, as shown in Fig. 4.7(a) at particle "A." The loop configuration suggests strong pining at the particle interface, as the loop contrast fluctuated but remained in place with sustained tensile displacement over

40 seconds until the local stress level was sufficient to overcome the attractive force between the loop and particle "A." As it detached from the interface, two prismatic loops were formed by rapid cross-slip and pinch-off (less than 0.04 seconds, Fig. 4.7(b)) reminiscent of variations on the Hirsch mechanism in experiments and simulations [34-35, 60]. 0.2 seconds later, Fig. 4.7(c), a lattice dislocation from the bottom of Fig. 4.7(b) has glided upwards while the loops at particles "B" and "D" also move on the prismatic cylinder. The lower loop, however, was intersected by the lattice dislocation at particle "C" while the lattice dislocation itself was fragmented by intersecting particle "A" to leave behind a segment pinned at particle "C." The bowed segment of the lattice dislocation, arrowed in Fig. 4.7(c) and (d), then continued to glide and after intersecting yet another particle in Fig. 4.7(d), became fragmented with only the left portion continuing to glide (Fig. 4.7(e)). With continued deformation, the trailing dislocation segment was able to detach from the interface, Fig. 4.7(f).

Aside from loops breaking free of the particles, it has also been observed that such structures could form as a result of dislocation-particle interactions. Fig. 4.8 presents a series of images taken from an *in situ* video in which attached loops were created and annihilated at the same particle. For ease of discussion, a schematic of the same interaction has been reproduced in Fig. 4.9. Initially, dislocation "1" extended from the foil surface (upper segment) to a Co particle located near the center of the image then on to another particle (lower segment). A second dislocation, labeled "2," also was pinned at the same Co particle, Figs. 4.8(b) and 4.24(b). The left segment of dislocation "2" continued to bow across the top of the particle which was then intersected by the upper portion of dislocation "1," sweeping both segments out of the foil. At the same time, a new dislocation ("3")

extending from the foil surface (upper segment) became pinned at four different Co particles, having first created an attached loop by local cross-slip, arrowed in Figs. 4.8(c) and 4.9(c). This loop was swept up by interacting with a lattice dislocation to create the configuration of dislocation "4" seen in Figs. 4.8(d) and 4.9(d). A cross-slipped segment at the same location as the previous loop was formed by the further bowing out of dislocation "4," Figs. 4.8(e) and 4.9(e), in the end generating another loop there as dislocation segments of opposite line directions intersected. The creation of the loop, arrowed in Figs. 4.8(f) and 4.9(f), also fragmented dislocation "4" such that the upper and lower segments were able to break away from the particles on which they were pinned. After remaining stationary for nearly three minutes, dislocation "1" appeared to break free of the lower Co particle to which it had been held and generated an attached loop of a different orientation (arrowed, Figs. 4.8(h) and 4.9(h)). Finally, cross-slip of the lower portion of dislocation "3" intersected the attached loop and the resulting dislocation segments were further fragmented by self-interaction and detachment from the group of particles, Figs. 4.8(l) and 4.9(l).

The evolution of the local microstructure illustrated in this example suggests that such looped configurations may form and be annihilated several times during the course of deformation in a particular region coupled with an increasingly complex interface decorated with attached dislocation loops and/or debris left by previous interactions. Although the Burgers vectors of the lattice dislocations involved in these interactions were not explicitly identified, dislocations "3" and "4" and the attached loops they created had the same Burgers vector which made the sweeping up of most of the dislocations tangles possible, as seen in Figs. 4.8(l) and 4.9(l). However, as additional slip systems become

activated in this region with continued deformation, the dislocation-dislocation interactions will produce more sessile and jogged segments as well as many more attached loops throughout the system—consistent with computer simulations results which indicated that debris such as half-loops, loops surrounding multiple particles, and single dislocation segments attached to the matrix-particle interface may play a role in the overall work hardening rate [97-101].

An additional type of interaction observed during *in situ* deformation of Cu-Co is presented in Fig. 4.10. In a region that appears to have undergone extensive twinning after *in situ* straining, several twins are visible alongside Co particles which seem to have been sheared by the twins, arrowheads in Fig. 4.10(a). Note, however, that due to the limited tilt range of the *in situ* straining stage, the twins were unable to be characterized via diffraction twin spots. When compared with relatively twin-free regions, the proclivity for dislocations to be attached to the twins, which is especially pronounced in the region between the arrowheads in Fig. 4.10(a), suggests that after being sheared, the particles impeded local dislocation activity. In some cases, particles even appeared to have been sheared by multiple twins, Fig. 4.10(b), with many dislocation segments extending from the particle to the twin bands. The stacking-fault contrast between several partial dislocations above particle "A" (magnified in Fig. 4.10(c)) suggests that perhaps microtwins could also shear the particles. It is significant that while twinning dislocations could shear the Co particles, none were observed to undergo shearing during interactions with perfect dislocations. Since *in situ* straining experiments showed cross-slip of lattice dislocations to operate predominately in the bypass of Co particles, this observation is somewhat surprising. A possible explanation may be that during normal *in situ* straining, twinning as

a deformation mechanism is not favorable due to the relatively low strain rates [25]. But occasionally, in certain regions of the foil the local strain rate may be sufficient to nucleate twins; and that once formed, twinning dislocations moved so rapidly in the foil that particle cutting was feasible. Although twinning can occur during electrojet-thinning where a local region in the sample experiences high strain rates due to foil bending, this does not appear to be the case since the virgin microstructure prior to *in situ* straining did not appear to be more bent than usual and the region captured in Fig. 4.10(a) is not located at the thinnest part of the sample. Further study of this phenomenon was carried out in *post mortem* and electron tomographic observations and will be discussed in more detail in Sections 4.2 and 4.4.

4.2 Observation of Deformed Microstructure

In order to characterize and analyze in more detail the interactions observed in the previous section, *post mortem* examinations of each alloy system after either *in situ* or *ex situ* deformation have been carried out. In some instances, 3-mm discs were extracted from straining samples to facilitate analysis; in other cases, the samples were deformed in bulk then thinned to electron transparency. As with the previous section involving *in situ* results, the method of observation is primarily strain-contrast imaging using transmission electron microscopy with the addition of characterization techniques such as $\mathbf{g} \cdot \mathbf{b}$ analysis.

4.2.1 Post Mortem *Microstructure in Al-Cu*

Fig. 4.11 illustrates various types of dislocation-particle interactions observed in the Al-Cu system. Arrowheads in Fig. 4.11(a), taken under a two-beam bright-field condition

and those in Fig. 4.11(b), taken under a kinematical bright-field condition, indicate locations of shearing of the θ-plates. The dislocations are imaged as white lines in bright-field due to a contrast reversal caused by the overlapping of precipitate layers such that $\mathbf{g} \cdot \mathbf{b} = \pm\frac{2}{3}$ [102-103]. It can be seen from Fig. 4.11(a) that the displacement associated with a shearing event is not readily visible, and that only the disruptions in the displacement fringes indicate shearing has occurred. Occasionally, a particle may also be sheared by more than one set of dislocations, as indicated by the two sets of arrowheads in Fig. 4.11(b).

Alternatively, dislocation interactions with Al_2Cu plates can also involve glide in the particle interface, as first demonstrated in Fig. 4.3. A weak-beam dark-field image taken under (**g**, 3**g**) using $\mathbf{g} = 0\bar{2}0$ is presented in Fig. 4.11(c) which shows the arrays of dislocations in the particle interface (arrowheads) as well as the complex arrangement of dislocation segments in the surrounding matrix, pinned at the ends at an interface or foil surface. These arrowed arrays of dislocations are similar to those observed gliding in the interfacial plane during *in situ* straining experiments. The spatial arrangement of these segments of dislocations is not extractable from this kind of image alone—as will be presented in Section 4.4, electron tomography can be used to overcome this limitation. Fig. 4.11(d) shows an extremely deformed region where the numerous slip traces left by previous dislocation activity are visible in the central region. The area surrounding it are populated by θ-plates whose interfaces have become a trapping site for short dislocation segments and interaction debris such that the region has a cellular distribution of dislocation tangles with the θ-plates serving as cell boundary walls.

In order to determine the Burgers vectors of *post mortem* interfacial dislocations like those shown in Fig. 4.11(c), a series of bright-field images were recorded using three different **g**-vectors, Fig. 4.12, where (a) $\mathbf{g} = \bar{1}\bar{1}1$, (b) $\mathbf{g} = 020$, and (c) $\mathbf{g} = \bar{1}11$. Since the electron beam direction was close to the [101] zone for all three images, one family of θ-plates were edge-on (those on $(010)_{Al}$ planes) and two families (those on $(100)_{Al}$ and $(001)_{Al}$ planes) were inclined. Of the latter two families, two particles on the $(100)_{Al}$ are outlined in red and one particle on $(001)_{Al}$ is outlined in blue, Fig. 4.12(a)-(c). By performing $\mathbf{g} \cdot \mathbf{b}$ analysis, it was established that the interfacial dislocation arrays had either a Burgers vector of $a/2[110]$ or $a/2[01\bar{1}]$. Clearly, those dislocations residing on the $\{100\}_{Al}$-plates could not have a Burgers vector of $a/2[110]$ since neither of the possible slip planes, the γ-plane and the α-plane, match the projected line directions seen in Fig. 4.12(a)-(c). A similar line of reasoning applies for the dislocations residing on the $(001)_{Al}$ planes with the result that all the dislocations residing in the interface of $(100)_{Al}$-plates (outlined in red) have a Burgers vector of $\mathbf{b_{Al}} = a/2[01\bar{1}]$ and all those residing in the interface of $(001)_{Al}$-plates (outlined in blue) have a Burgers vector of $\mathbf{b_{Al}} = a/2[110]$. In the body-centered tetragonal crystal structure of Al_2Cu, the possible Burgers vectors are $a/2\langle 111\rangle$ on {110} or {112} and $a\langle 001\rangle$ on {110} or {200} [104-105]; but *in situ* results, in particular Fig. 4.4, have shown that these dislocations most likely did not enter the Al_2Cu phase because they were glissile in the particle-matrix interface. The glide of dislocations on {001} planes in pure crystals of Cu, Ni, and Ag—which, like Al, have a face-centered cubic lattice structure—have been reported previously to occur for composition dislocations having $\mathbf{b} = a/2\langle 110\rangle$ from Lomer-Cottrell reactions in which the partials did not split on

two {111} planes. These dislocations could glide on {001} planes and could also easily cross-slip back onto a {111} plane; but for certain systems such as Cu-15%Al, glide on the {001} planes was found to be halted due to the high friction stress [106-107].

Typically, the highly-deformed microstructure shown in Fig. 4.11(d) was accompanied by one or more cracks present in the sample, having propagated into regions of the sample opaque to the electron beam. An example of this type of crack is shown in Fig. 4.13. As the crack propagated to this region from the right of the image, the original crack path was deflected several times, as marked by arrowheads. Each of the crack deflection occurred along the length of and adjacent to θ-plates even though the crack itself never contacted a particle but only propagated in the matrix region between plates. Crack deflection around the particles, the preference of cracks to go through particle-free "pathways" (such as that shown in Fig. 4.2), and the fact that cracks do not occur at the particle interface all attest to the efficacy of Al_2Cu particles in hindering dislocation glide as well as illustrating the strength of the particle-matrix interface of Al_2Cu plates.

4.2.2 Post Mortem *Microstructure in Al-Sc and Al-Mg-Sc*

Figure 4.14 presents some examples of *post mortem* dislocation structures surrounding Al_3Sc particles. In Fig. 4.14(a), a number of dislocation segments can be seen to end at the interface, with the half-loop undergoing cross-slip away from the particle (arrowheads denote location of cross-slip). For this very large particle with a radius of 570 nm, the contrast of the particle interface also illustrates the complexity of the interfacial dislocation network. Therefore, when a matrix dislocation impinges on such particles, interaction with the interfacial dislocations would likely result in some rearrangement of the

interfacial network, which has only been implied from *in situ* videos. Fig. 4.14(b) and (c) show dislocation segments residing partially in the interface and the presence of loops attached on one side to the interface. In Fig. 4.14(d), a network of matrix as well as interfacial dislocations form a sort of "grid" littered with interaction debris such as small loops (arrowed) on and around the particle. In addition to interacting with single dislocations, some particles were found to have interacted with an array of dislocations. Fig. 4.14(e)-(f) shows images of the *post mortem* microstructure after a particle has interacted with a twist boundary composed of two sets of dislocation arrays with different Burgers vectors. The vertical array shown in Fig. 4.14(e), imaged using a two-beam bright-field condition with $\mathbf{g} = 11\bar{1}$, was determined using $\mathbf{g} \cdot \mathbf{b}$ analysis to have Burgers vector $\mathbf{b} = a/2[0\bar{1}1]$; and the horizontal array, barely visible due to the invisibility criterion, was determined to have Burgers vector $\mathbf{b} = a/2[1\bar{1}0]$. Though the majority of the boundary has already bypassed the particle, moving from right to left, a few individual dislocations from the array remain attached to the particle interface, appearing to wrap around it. Since other dislocations in the array have already detached from the particle interface, it is expected that with continued deformation, those dislocation segments still attached will eventually detach, allowing the boundary to continue to glide. However, as suggested by *in situ* straining experiments, these interactions certainly altered or caused rearrangements in the interfacial dislocation network resulting in changes in interfacial strain. In Fig. 4.14(f), the Al_3Sc particle also appeared to be on the verge of full bypass by the boundary. Apparently possessing a less complex interfacial structure, the particle has a complete loop around its equator which may be in the interface. Approximately 5.6 x 10^{-7}m away, a large loop of

comparable size but different orientation can be seen (arrowhead on right). From these images, it could not be positively determined how the loop related spatially to the particle. Whether if it was the result of boundary-particle interaction is not clear in this case; but a similar microstructure has been recorded using electron tomography of a dislocation array and the interaction debris left around the same type of particle and will be discussed in further detail in Section 4.4.

4.2.3 Post Mortem *Microstructure in Cu-Co*

Similar to the Al_3Sc particles, there are several structures of post-deformed Cu-Co such as cross-slip of dislocation sections pinned in at least one location, as seen in Fig. 4.15(a), and the creation of standalone loops from a loop surrounding the particle, Fig. 4.15(b). The loop surrounding the particle is different from an Orowan loop; from *in situ* results, these are likely caused by cross-slip of dislocation segments pinned on one side to the interface, such as the arrowed loop in Fig. 4.15(c). Occasionally, multiple half-loops could be found on one particle, as indicated by the left arrowhead in Fig. 4.15(d). More frequently, however, loops that surround two or more particles were observed, like those marked in Fig. 4.15(e)-(f). The loop on the left in Fig. 4.15(f) appears to be "broken" due to a segment interacting with the interfacial dislocations severing from the rest of the original dislocation in order to continue glide, similar to the interaction seen in Fig. 4.8.

In situ experiments also suggested an alternate mechanism in which Co particles were sheared by small twins. As Fig. 4.16 shows, this type of interaction is indeed particle shear, as the displacement of the upper portion of the particle relative to the lower portion can be seen in Fig. 4.16 (a), from an edge-on view with beam direction parallel to the (110)

normal and (b), a slightly tilted view showing the projected width of twin bands. And in Fig. 4.16(c), several closely-spaced parallel twins can cause multiple shearing of the same particle, displacing the particle over a distance of 6.7×10^{-8} m which, if it were caused by particle cutting, would require more than 230 dislocations.

4.3 High-Resolution Electron Microscopy

4.3.1 Al_2Cu Platelets

As mentioned previously, the Al_2Cu plates are highly anisotropic, with the broad side, along the plate-growth direction being more coherent with the aluminum matrix than the short side, perpendicular to the growth direction. In order to discern the mismatch, high-resolution images of the particles were acquired. An example of such an image is shown in Fig. 4.17(a). The orientation relationship between the particle and the matrix atoms can be clearly seen: whereas the matrix displays a {110} type arrangement, for the particle it is clearly {001}. Using the Gatan DigitalMicrograph software, the HREM image in Fig. 4.17(a) was Fourier-transformed to obtain a diffraction pattern, Fig. 4.17(b), corresponding to the aluminum [101] zone. By applying a mask over the rest of the diffraction pattern save one pair of spots, e.g., the (020) spots as indicated in the inset in Fig. 4.18(b)), they were Fast Fourier-transformed to produce the plane-reconstructed image showing all (020) planes, Fig. 4.17(c). The interface or geometrically necessary edge dislocations can be clearly visualized in locations where an extra half-plane occurs, magnified and traced in the inset in Fig. 4.17(c). When all dislocations have been identified, indicated by the blue circles, they can be superimposed onto the original high-resolution

image, revealing the location of interfacial edge dislocations, denoted by yellow circles in Fig. 4.17(d). This analysis confirmed the interface anisotropy of the Al_2Cu platelets. The narrow side of the particle was incoherent since it contained numerous interfacial dislocations whereas the broad side remained relatively coherent with the aluminum matrix, containing fewer interfacial dislocations. Notably, comparable results supporting this conclusion were also reached by repeating the Fourier transform plane-reconstruction for the $(11\bar{1})$ and $(1\bar{1}\bar{1})$ spots.

Fig. 4.18 shows high-resolution images for each of the interface sites, where disruptions in contrast due to growth ledges, denoted by arrowheads, illustrate the reason why there is such a marked difference in the interface character: Since the plates grow preferentially in the [010] direction by a terrace-ledge-kink mechanism [89, 93], the narrow side growth ledges (Fig. 4.18(a)) were much more numerous and pronounced than the occasional ledge found on the broad side associated with particle thickening, perpendicular to the growth direction (Fig. 4.18(b)).

4.4 Diffraction-Contrast Electron Tomography

As mentioned in Section 4.1 and 4.2, interpretation of the dislocation structures seen in *in situ* and *post mortem* observations is complex and the three-dimensional spatial arrangement is not easily extractable from these projected images. Past efforts in achieving some measure of "3D" resolution, such as stereo microscopy, were not truly three-dimensional as the effect was only present in the direction in which the left and right stereo- or anaglyph-pairs were taken. One of the challenges undertaken in this work was developing a method with which we can obtain truly 3D, or spatially-resolved dislocation

microstructures. As outlined in Chapter 3, this goal has been accomplished and there is at present a well-established procedure in employing electron tomography in order to produce faithful reconstructions. This section presents a selection of the electron tomographic results in investigating and understanding dislocation-particle interactions in each of the three alloy systems.

4.4.1 Spatially-Resolved Microstructure in Al-Cu

Since the Guinier Type I plates in Al-Cu reside on {001}-type planes, they can be classified into three distinct families: those residing on parallel $(0\bar{1}0)$ planes, on parallel (100) planes, and those on parallel (001) planes. The micrographs presented in Figs. 4.19(a)-(c) show a number of bright-field micrographs ($\mathbf{g} = \bar{1}\bar{1}1$) from a tilt series composed of 41 images acquired over $\pm 40^{o}$ at intervals of 2^{o}, of a largely undeformed region containing Al_2Cu plates. Since the imaging vector was held constant, the projected growth direction of the plates could be used to identify their habit planes—these are marked with dashed lines in Fig. 4.19. It can be seen that this particular region of the foil consisted of mostly θ-plates residing on parallel $(0\bar{1}0)$ planes and parallel (100) planes. As the tilt value was changed, the fringe contrast on the particles also evolved as a function of the deviation from the Bragg diffracting condition and the relative increase in the thickness of the foil. To avoid the deleterious effects of strong strain contrast, the images were carefully adjusted throughout the acquisition process. After alignment and reconstruction of the volume, a traced dislocation structure model was made such that the three families of plates were colored-coded with those on $(0\bar{1}0)$ planes in orange; those on (100) planes in blue;

and those on (001) planes in green. Fig. 4.20 illustrates the enhanced visualization of 3D structures with electron tomography: the habit plane of each plate can be discerned simply by inspection. In particular, compare the tomographic reconstruction presented in Fig. 4.20(a) with the bright-field micrograph presented in Fig. 4.19(a). Although they share the same projected orientation, the overlapping of particles and the relative positions of each family of plates are unambiguously represented in the tomographic reconstruction. Although a few dislocations were present, colored in yellow, it can be seen that the matrix was largely devoid of dislocations or defects, the only prominent features being the population of θ-plates. The dislocations present also appeared to be relatively short segments with one end pinned on a particle interface or to the foil surface; by comparing the view in Fig. 4.20(b) and (c) with the embedded crystallographic coordinates, it was determined that they resided on $\{\bar{1}\bar{1}1\}$, or γ-planes.

After deformation, however, the microstructure surrounding the θ-plates was found to have evolved significantly to become vastly more complex. Fig. 4.21(a) shows a (**g**, **3g**) weak-beam dark-field micrograph (**g** = $11\bar{1}$) from a tilt series composed of 41 images acquired over an angular range of 62^{o} at intervals of 2^{o}, of a highly-deformed region. Bright-field imaging with strong diffraction contrast could not be used in this instance due to the high density of dislocation structures. Two regions, highlighted in red (magnified in Fig. 4.21(b)) and blue (magnified in Fig. 4.21(c)) boxes, illustrate the complexity of the dislocation arrangement. In the red box, a region in the Al-matrix surrounded by θ-plates appears to have developed a complicated tangle of dislocations; but the actual arrangement of these dislocations is not clear from the image alone. In the blue box, a loop-like

structure can be seen behind the large (100)-particle but its orientation and relationship to the particle remain ambiguous. In order to answer these questions, a tomogram was reconstructed from the tilt series images and a traced dislocation structure model was produced, Fig. 4.22. Again, the three families of θ particles are color-coded in the same way as the undeformed Al-Cu shown in Fig. 4.20. It can be seen from the three views presented in Fig. 4.22(a), (d), and (g) that lattice dislocations have fully populated the regions in between particles, many of which experienced cross-slip of at least one segment along their length onto conjugate slip planes or bowing at large angles around the plates. Fig. 4.22(a) shows the same projected view as Fig. 4.21(a) and the complex dislocation tangle in the red box can now be viewed from any angle. Three of these views, magnified in Fig. 4.22(b), (e), and (h), show that the tangle consists of three lattice dislocations all pinned at particles with the middle segment undergoing cross-slip between a particle residing on a $(0\bar{1}0)$ plane and the foil surface. Since the tilt series was acquired using **g** = $11\bar{1}$, the Burgers vector of the cross-slipped segment can only be $a/2[110]$, $a/2[10\bar{1}]$, or $a/2[01\bar{1}]$. Of these, only **b** = $a/2[110]$ is capable of slip on both the α- and β-planes corresponding to the slip planes determined by the tomogram.

The large loop inside the blue box in Fig. 4.21 can be analyzed in a similar fashion—from the magnified views presented in Fig. 4.22(c), (f), and (i), the loop was determined to have formed from the intersection of two dislocation segments residing parallel to or inside the (100)-plate interface. Due to the resolution limit of the tomogram, this ambiguity could not be eliminated. However, *in situ* straining experiments of Al-Cu have already shown that lattice dislocations can glide in the particle interface under

sufficient local stress and the bowing of these two dislocation segments in the interface is reminiscent of dislocations undergoing interfacial glide.

In general, most dislocations were found to be pinned at both ends to a particle interface belonging to different plate families, rendering breakaway more difficult. Small loops, seen near the center of Fig. 4.23(a)-(c), may also indicate the production of interaction debris as matrix dislocations contort or bow around the plates and interact with other dislocations. Magnified views of several of these dislocations (colored magenta) are presented in Fig. 4.23(a)-(c) with the direction of dislocation motion denoted by arrows. Rather than cutting the smaller (001)-plate, the dislocations seem to bow around it with a small portion of the dislocation line residing close to or on the particle interface. By using the tomographic reconstruction, they are determined to have a Burgers vector of either $a/2[10\bar{1}]$ or $a/2[01\bar{1}]$. If deformation were allowed to continue, the final microstructure might resemble Fig. 4.11(d) where the inter-particle region in the matrix has a reduced density of dislocations but the interface regions near the particles have a very high density of dislocations.

4.4.2 Spatially-Resolved Microstructure in Al-Sc and Al-Mg-Sc

Post mortem observation of dislocation interactions with Al_3Sc particles has revealed an extremely complex microstructure surrounding the particles, such as that shown in Fig. 4.14(d) where a field of dislocations, interaction debris, and interfacial dislocations surround a large Al_3Sc particle. Undoubtedly, the ability to spatially resolve these structures will facilitate the interpretation and understanding of the dislocation-particle

interactions that have taken place.

A post-deformation structure similar to Fig. 4.14(d) was captured by a (**g**, **3g**) weak-beam dark-field tilt series (**g** = 200) composed of 61 images acquired over an angular range of 60^o at intervals of 1^o [50]. Fig. 4.24 (top row) shows the reconstructed tomogram of this series from three different vantage points where the large spherical Al_3Sc particle located in the center is surrounded by many line dislocations as well as loops. A traced dislocation structure model, Fig. 4.24 (bottom two rows), reveals the full complexity of this structure. For clarity, individual dislocation segments are represented in different colors even though nearly all of the dislocations present were determined to have the same Burgers vector, **b** = $a/2[1\bar{1}0]$, by **g** · **b** analysis. Those dislocations colored in white have Burgers vectors ($\omega 1$) **b** = $a/2[101]$, ($\omega 2$) **b** = $a/2[10\bar{1}]$ and ($\omega 3$) **b** = $a/2[1\bar{1}0]$. By coupling prior knowledge about dislocations with the Thompson tetrahedron embedded in the volume, a complete characterization of dislocation slip planes and line directions was accomplished and the results are summarized in Table 4.1.

Most of the dislocations in blue colors extend between the two foil surfaces without contacting the particle. The general complexity in shape of these dislocations suggests that they may have previously interacted with and subsequently bypassed the particle. In contrast, there are also dislocations which terminate with both ends on the particle interface; for example, the dislocation half-loops in orange labeled "a," "b," and "c" in Figs. 4.25 and 4.29. While half-loop "c" resides on one slip plane (γ-plane), both half-loop "a" and "b" reside on two slip planes via cross-slip with "a" originally lying on the δ-plane and "b" on the γ-plane. After cross-slip, the half-loops come to reside on the γ-plane for "a"

and the δ-plane for "b." The Burgers vector of the half-loops, namely $a/2[1\bar{1}0]$, is consistent with the intersection between the two slip planes and it is believed that the loops cross-slipped as they extended away from the particle in order to glide on more energetically favorable slip planes.

Two alternate views from the traced tomogram are presented in Fig. 4.25(a) and (b), highlighting a standalone dislocation loop (colored red) and an attached loop on the particle interface (colored yellow and labeled "d"), respectively. The red loop located to one side of the particle was found to reside on the $(\bar{1}\bar{1}1)$, or γ-plane as indicated by the dashed line to the Thompson tetrahedron, Fig. 4.25(a). The inset of Fig. 4.25(a) shows a magnified view of the region surrounding the red loop: The blue dislocation labeled "2" has a Burgers vector **b** = $a/2[1\bar{1}0]$ and a line direction and slip plane that changes, from the side closest to the red loop, from CA (δ) → AD (γ) → AB (γ) → DB (γ) → DA (γ), indicating it has cross-slipped as it approaches the foil surface. The blue dislocation labeled "1" has the same Burgers vector and a line direction that changes from the side closest to the red loop from BA (γ) → BC (δ) → AB (δ) → CB (δ) → DB (γ). Since both "1" and "2" end on the same foil surface, it is suggested they could have been loops similar to the red loop which have grown large enough to eventually intersect the foil surface. The change in line direction as a free surface is approached is consistent with the influence of surface image forces on the direction of the line dislocation. In addition, the proximity of the red loop to the orange half-loop "a" and the fact that the cross-slipped segment of "a" resides on the same slip plane imply that it may have resulted from a pinch-off of a previously cross-slipped dislocation segment similar to the half-loop "a." It is possible for a portion of the

dislocation conforming to the particle surface to pinch off, producing the partial-loop configurations similar to orange loops "a" and "b" with the remaining segment extending from the matrix-particle interface to the free surface. Alternatively, the loops could cross-slip with pinch-off occurring at the cross-slip point to release one loop from the particle and leave another tethered to it. The tethered loop may expand again under the influence of an applied stress, allowing the process to either repeat or the loop to collapse onto the particle-matrix interface and become accommodated.

The yellow attached loop labeled "d" was found to reside on the (111), or δ-plane as indicated by the dashed line to the Thompson tetrahedron, Fig. 4.25(b). The inset of Fig. 4.25(b) shows a magnified view of the region surrounding the attached loop. From *in situ* straining experiments, it has already been established that attached loops or half-loops may be generated as a result of dislocation-particle interactions, most likely through the cross-slip of one or more dislocation segments while being locally pinned on the particle interface. The yellow dislocations labeled "m" and "n" appear to be undergoing a similar process on a parallel δ-plane, with most of their length devoted to bowing around the Al_3Sc particle. Several of the views presented in Fig. 4.24 reveal that they conform very closely to the local particle contour. However, due to the resolution limit of the tomogram, it is unknown whether they are simply bowing very close to the particle or are actually contacting the interface.

In general, the convoluted dislocation shapes and arrangement around the particle suggest an advanced deformation state formed by dislocations pinned at the particle extending away from the interface and interacting with other dislocation segments. When these dislocations encounter those from neighboring particles, possibly having a different

Burgers vector, the subsequent dislocation-dislocation interactions can produce debris which may accumulate in the region surrounding the particles.

A second type of *post mortem* microstructure of interest was shown in Fig. 4.14(e), in which an array of dislocations successively bypassed a large Al_3Sc particle. Again, due to the projected nature of the micrograph, questions about the alignment of individual dislocations in the array or the orientation of interaction debris with respect to the particle and the array could not be answered easily. A post-deformation structure similar to Fig. 4.14(e) of a twist boundary interacting with an Al_3Sc particle was captured by a (**g**, **3g**) weak-beam dark-field tilt series (**g** = 020) composed of 60 images acquired over an angular range of 59^o at intervals of 1^o [50]. Fig. 4.26 presents four images from the tilt series, (e)-(h), and the corresponding bright-field images, (a)-(d), at the same tilt values respectively. By comparing the two sets of images, for example Fig. 4.26(d) with (h), it can be seen that the use of two-beam bright-field imaging was not feasible due to the complexity of the interaction and the density of dislocation structures present. The reconstructed tomogram is shown in Fig. 4.27(a)-(b), and the traced dislocation model in Fig. 4.27(c)-(e). In this case, the traced model allows for a much clearer representation of the dislocation arrangement than the reconstruction alone, Fig. 4.27(a) and (e), in particular dislocations overlapped with or very close to the twist boundary.

Here, the dislocations are colored by Burgers vector: The screw dislocations forming the boundary have Burgers vectors of (orange, labeled "TB2") **b** = $a/2[0\bar{1}1]$ and (blue, labeled "TB1") **b** = $a/2[1\bar{1}0]$, and dislocations with **b** = $a[010]$ form at the intersection nodes of the two screw dislocations. Dislocation lines "a" and "b," partial

loops "c" and "d," and full loop, "e," have a Burgers vector of **b** = $a/2[011]$. It was found that not all of the dislocations that appear in Fig. 4.26 as being part of the twist boundary actually reside on the boundary plane despite having the same Burgers vector: Dislocations "1" and "2" in Fig. 4.27(e) have a Burgers vector of **b** = $a/2[1\bar{1}0]$, which is the same as the twist boundary dislocations labeled "TB1" (colored blue), but do not reside inside the boundary. Also, the dislocation indicated by the arrowhead in Fig. 4.27(c) and (e) was part of the dislocation array but remained bowed out from the array plane, having interacted with the particle but has yet to realign with the other dislocations in the boundary. Alternatively, it is possible, although not verified in this case, that this dislocation is in the process of detaching from the array. This ejection of dislocations from the twist boundary may explain the origin of dislocations "1" and "2," which may be a sign of the instability of the twist boundary after it has interacted with the particle.

Line dislocation "b" extends from the particle surface to the free surface whereas dislocation "a" extends through the foil and has interacted with the particle as evidenced by its curvature. Partial loops "c" and "d" reside on the α-plane although there is some distortion near the free surface; such distortions are expected from surface image force considerations. Note, however, that as the tomogram is formed with **g** = 020, dislocations with a Burgers vector of either **b** = $a/2[10\bar{1}]$ or **b** = $a/2[101]$ are invisible and this can lead to misinterpretation of tomographic images in a similar manner as it would do in conventional micrographs. For example, the complete loop "e" appears to lie on two different planes, the lower portion resides on the β-plane but the upper portion does not coincide with an allowed plane. From bright-field images formed with different diffraction

vectors, two additional dislocations, one with a Burgers vector of $\mathbf{b} = a/2[101]$ and the other with $\mathbf{b} = a/2[10\bar{1}]$, intersect the loop at the two locations where it is kinked. These interactions yield segments with Burgers vectors of $\mathbf{b} = a/2[\bar{1}10]$ and $\mathbf{b} = a/2[110]$, respectively. These interactions account for the observed form of this dislocation loop. Thus, it is possible to specify in detail the configuration of the dislocations interacting with and in the vicinity of the particle.

A dislocation, labeled "3," extended from the twist boundary to wrap around the particle interface, forming a partial loop in the particle interface. Similar to dislocation "b," as the twist boundary retracts from the particle, individual segments of the boundary detach and realign into the lowest-energy configuration. It is believed that with continued deformation, all segments of the array will detach to continue glide, leaving behind the partial loops in the interface.

4.4.3 Spatially-Resolved Microstructure in Cu-Co

An example of dislocation-particle interactions in the Cu-Co system involving semi-coherent particles is shown in Fig. 4.28. Micrographs presented in Fig. 4.28(a)-(b) show two bright-field images of the same region acquired using two diffracting vectors, $\mathbf{g} = 1\bar{1}\bar{1}$ and $\mathbf{g} = 11\bar{1}$, respectively. Following the procedure described in Section 3.3.5, dual-axes electron tomography was used to obtain a reconstruction of the volume of interest, followed by 3D-tracing to produce a dislocation structure model, Fig. 4.28(d)-(e). By using $\mathbf{g} \cdot \mathbf{b}$ analysis, the Burgers vectors of the dislocations were determined and color-coded in the structure model along with an embedded Thompson tetrahedron whose orientation was

determined by using image-diffraction pattern pairs. Several half-loops were observed to be attached to the particle interface, indicated by arrowheads in Fig. 4.28(d). These are small loops which resided entirely on one slip plane and had no cross-slipping segments: The blue loop, which has a Burgers vector of **b** = $a/2[10\bar{1}]$, resided on the α-plane; and the two red loops, which have a Burgers vector of **b** = $a/2[1\bar{1}0]$, resided on the δ-plane, Fig. 4.28(e). Also notable was that within the reconstructed volume, dislocations with five different Burgers vectors were present, perhaps suggesting a proliferation of prior dislocation-dislocation interactions. With further deformation, these dislocation segments will interact with each other, which can lead to the appearance of a complex network of dislocations surrounding the Co particles.

The observed interactions between dislocations and Co particles are reminiscent of those for small (~70 nm), semicoherent Al_3Sc particles. The similarity in particle size and interfacial contrast between the Co and Al_3Sc particles, seen in Fig. 4.5 and Fig. 4.15, may account for why the generation of an attached dislocation loop by dislocation cross-slip was favored over classical bypass mechanisms such as particle cutting and Orowan looping. Both particles diameters were much larger than the predicted particle shear-Orowan looping transition (no more than 27.6 nm for Al_3Sc [17, 108] and 20.2 nm for Co) using |**b**| = 0.25 nm, $G_{FCC\ Co}$ = 75 GPa, f ≈ 0.1, γ ≈ 13.5 erg cm^{-2} [109]) but were still small enough such that a combined looping/cross-slip bypass was energetically favorable. At larger particle sizes, up to 250 nm as mentioned in Section 4.4.3 for Al_3Sc particles, the creation of an attached loop appears to still operate as part of the bypass mechanism (Figs. 4.24, 4.25) but a variety of other dislocation configurations were also present, indicative of a

transition from looping to interactions involving the particle interface and interfacial dislocations as the predominant mode of bypass.

Though similar to dislocation interactions with Al_3Sc particles in several respects, bypass of Co particles in Cu exhibited an unexpect mechanism, as suggested by *in situ* and *post mortem* analyses, which involves shearing by small twins of particles normally not shearable by dislocations. Fig. 4.29(a)-(d) shows four views from a dual-axes tomogram (also see Fig. 3.15) captured using $\mathbf{g} = \bar{2}20$ and $\mathbf{g} = 0\bar{2}0$, of sheared Co particles where the original, or unsheared particle locations are represented by purple markers and the displaced, or sheared particle locations by yellow markers. Although no twins were present when the tilt series images were acquired (see Fig. 3.15(a)-(b)), Fig. 4.29(c) clearly shows that the shearing, or particle-displacement direction (indicated by the red arrow) does not correspond to the slip trace direction (as indicated by the blue arrow). Furthermore, the configuration is similar to that presented in Figs. 4.10 and 4.16, in which small twins were observed to have sheared semi-coherent Co particles of comparable size during *in situ* straining and *post mortem* observation, respectively. Short dislocation segments as well as half-loops were also seen to span between the sharing plane and the sheared particles in Fig. 4.29(a)-(b) in a similar manner to Fig. 4.16(a)-(b), thought to be the result of the twins impeding lattice dislocation motion. Although no direct observation of twinning dislocations shearing Co-rich particles were made in real-time, the available results suggest that particle-cutting is generally unfavored as a means of dislocation bypass of these particles. When particle-cutting does occur, it is accomplished by the propagation of small twins and occasionally may even shear the same particle multiple times along parallel twinning planes. As for the microstructure in Fig. 4.29, it is hypothesized that the particles

were previously sheared by a twin before matrix stacking was restored by the operation of more twinning dislocations.

Future work in the form of high-strain rate deformation via split-Hopkinson pressure bar tests, known to induce twinning [110], will be able to verify this hypothesis by assessing whether more particles are sheared and if they are sheared exclusively by twins, in order to fully establish the role of twinning in dislocation-particle interactions in the Cu-Co system.

4.5 Table

Identification	Burgers vector	Slip plane(s)	Line direction(s)
Red loop	$a/2[1\bar{1}0]$ = BA	ABD (γ)	----
Orange loop *a*	$a/2[1\bar{1}0]$	ABC (δ) → ABD (γ)	BC (δ) → BD (γ)
Orange loop *b*	$a/2[1\bar{1}0]$	ABD (γ) → ABC (δ)	AD (γ) → CB (δ)
Orange loop *c*	$a/2[1\bar{1}0]$	ABD (γ)	BD (γ)
Yellow loop *d*	$a/2[1\bar{1}0]$	ABC (δ)	----
Blue dislocation *1*	$a/2[1\bar{1}0]$	ABD (γ) → ABC (δ) → ABD (γ)	BA (γ) → BC (δ), AB (δ), CB (δ) → DB (γ)
Blue dislocation *2*	$a/2[1\bar{1}0]$	ABC (δ) → ABD (γ)	CA (δ) → AD (γ), AB (γ), DB (γ) → DA (γ)
Yellow dislocation *l*	$a/2[1\bar{1}0]$	Particle ABD (γ) → Particle ABC (δ) → ABD (γ)	DB (γ) → CA (δ) → BA (δ) → AD (γ)
Yellow dislocation *m*	$a/2[1\bar{1}0]$	ABD (γ), Particle ABD (γ) → Particle ABC (δ), ABC (δ)	BA (γ) → AC (δ)
Yellow dislocation *n*	$a/2[1\bar{1}0]$	ABD (γ), Particle ABD (γ) → Particle ABC (δ), ABC (δ)	BA (γ) → AC (δ)

Table 4.1. Complete characterization of all dislocations surrounding the Al_3Sc particle shown in Fig. 4.19(c)-(d) by using electron tomography. Cross-slipping is determined by slip plane information and the edge/screw character of a dislocation can be determined by its line direction [50].

4.6 Figures

Fig. 4.1. (a)-(f) Still images captured from an *in situ* straining experiment showing the initial stage of interaction between matrix dislocations and semi-coherent Al_2Cu platelets (labeled A1-A5). Arrows indicate how far the dislocations have advanced by successive and multiple shearing of the particles. (g) A schematic of the particles (colored blue) and regions of observed dislocation activity in the matrix (between arrows) and in the particle interface (in green) is superimposed over a montage of the same region for clarity.

Figure 4.1 (cont.)

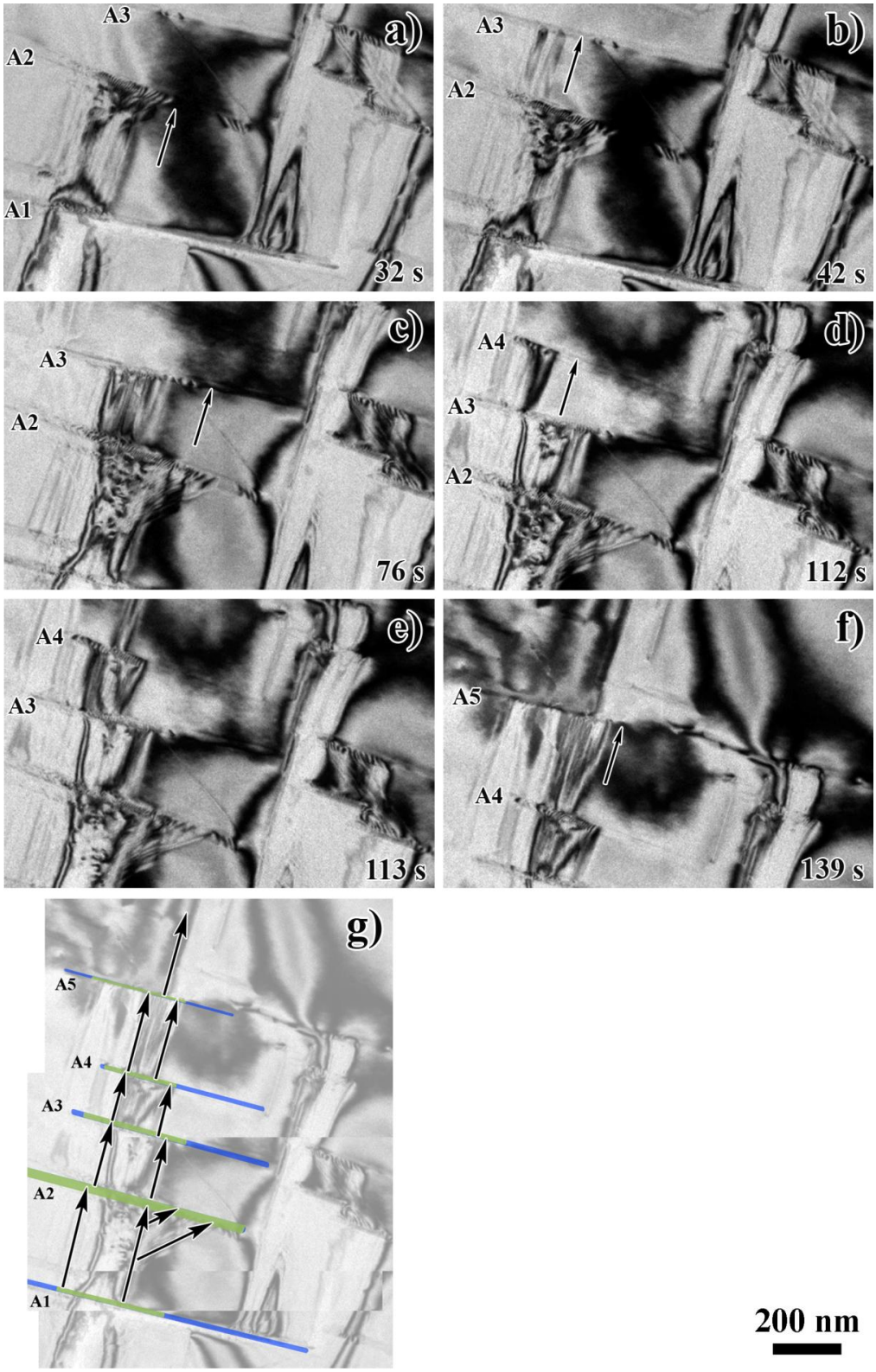

Fig. 4.2. The dislocation-emitting crack from Fig. 4.1 after *in situ* straining. The first sheared Al_2Cu platelet 'A1' is denoted by arrowheads. Regions labeled 'B' show a predominance of the same slip traces left by dislocations seen in Fig. 4.1. Smaller particles of the same orientation as 'A1' are present in the thinner regions of the foil, labeled 'C,' which did not interact with the crack.

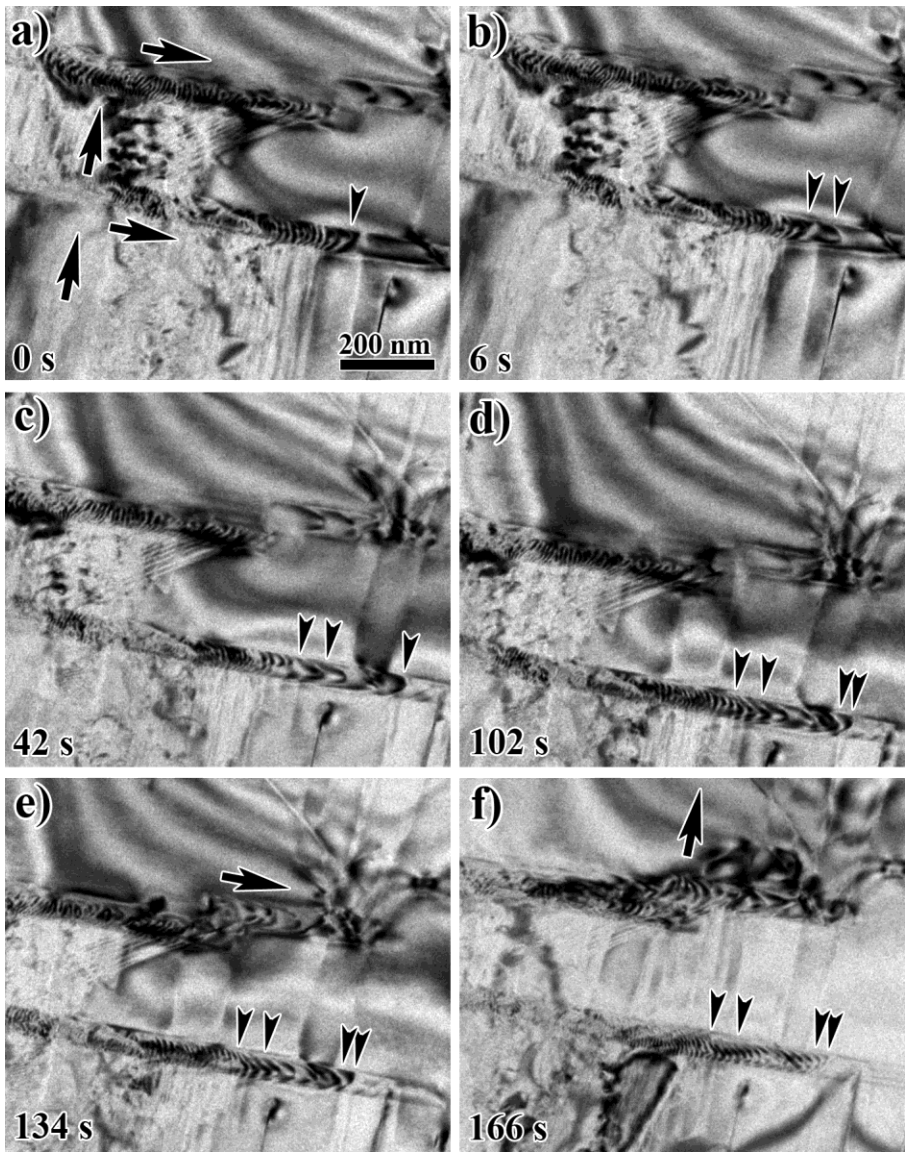

Fig. 4.3. Still images captured from an *in situ* straining experiment in Al-Cu where matrix dislocations, emanating from the lower left, were accommodated into the particle-matrix interface and move along the interface (denoted by arrowheads) as more dislocations impinge on the particle, (a)-(c); but the motion became arrested, (d)-(f), subsequently only the density of dislocations increased.

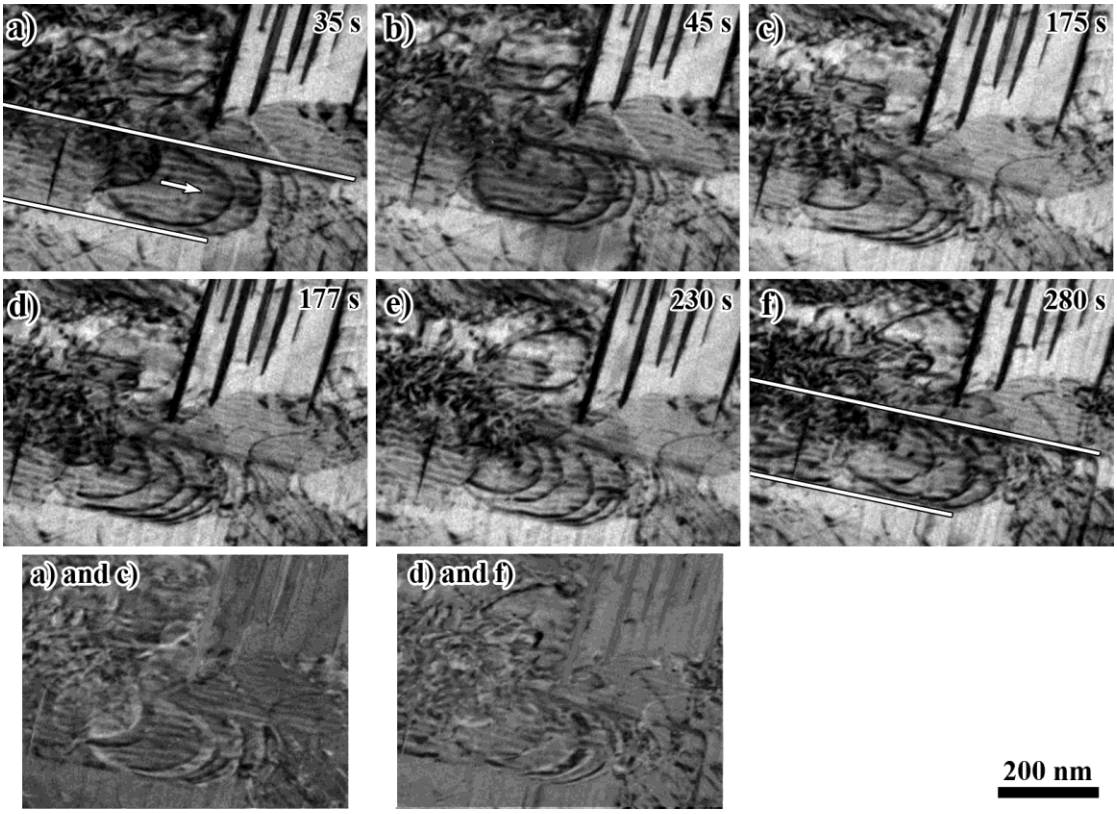

Fig. 4.4. Still images captured from an *in situ* straining experiment showing glide of dislocations along the interface of an Al_2Cu platelet particle, outlined in white in (a) and (f). The dislocations moved rapidly, comparison images (a and c) and (d and f), to one end of the particle then exited by cross-slip.

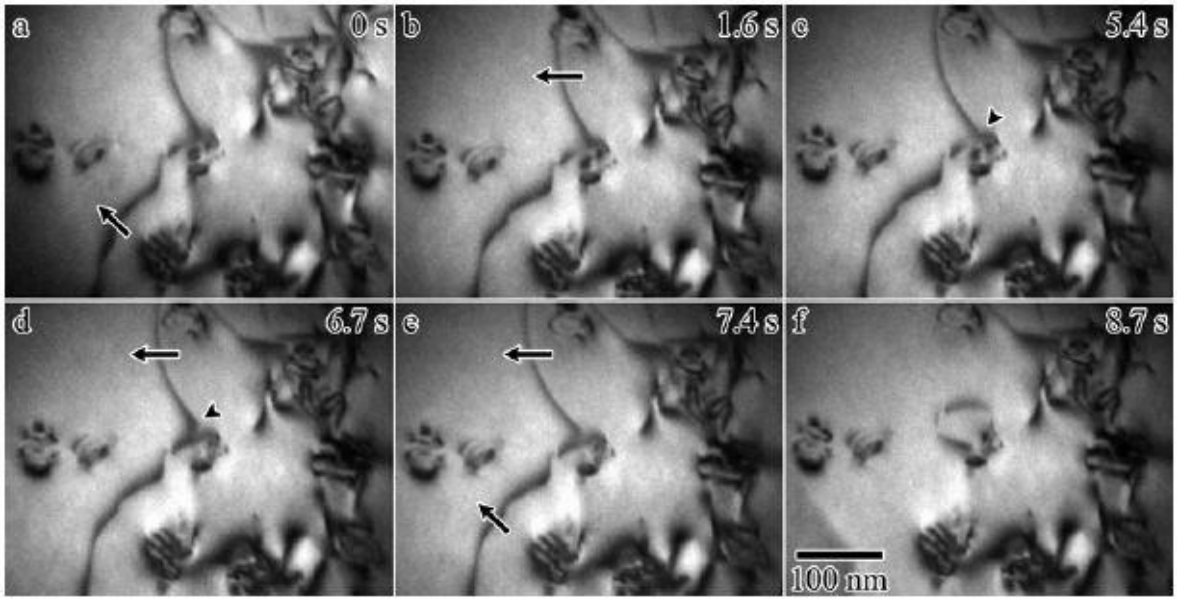

Fig. 4.5. A lattice dislocation interacting with a semi-coherent Al_3Sc particle where the cross-slip of a jogged segment, (b)-(d), while pinned at the particle interface resulted in the creation of an attached loop to one side to the particle-matrix interface, (f) [17].

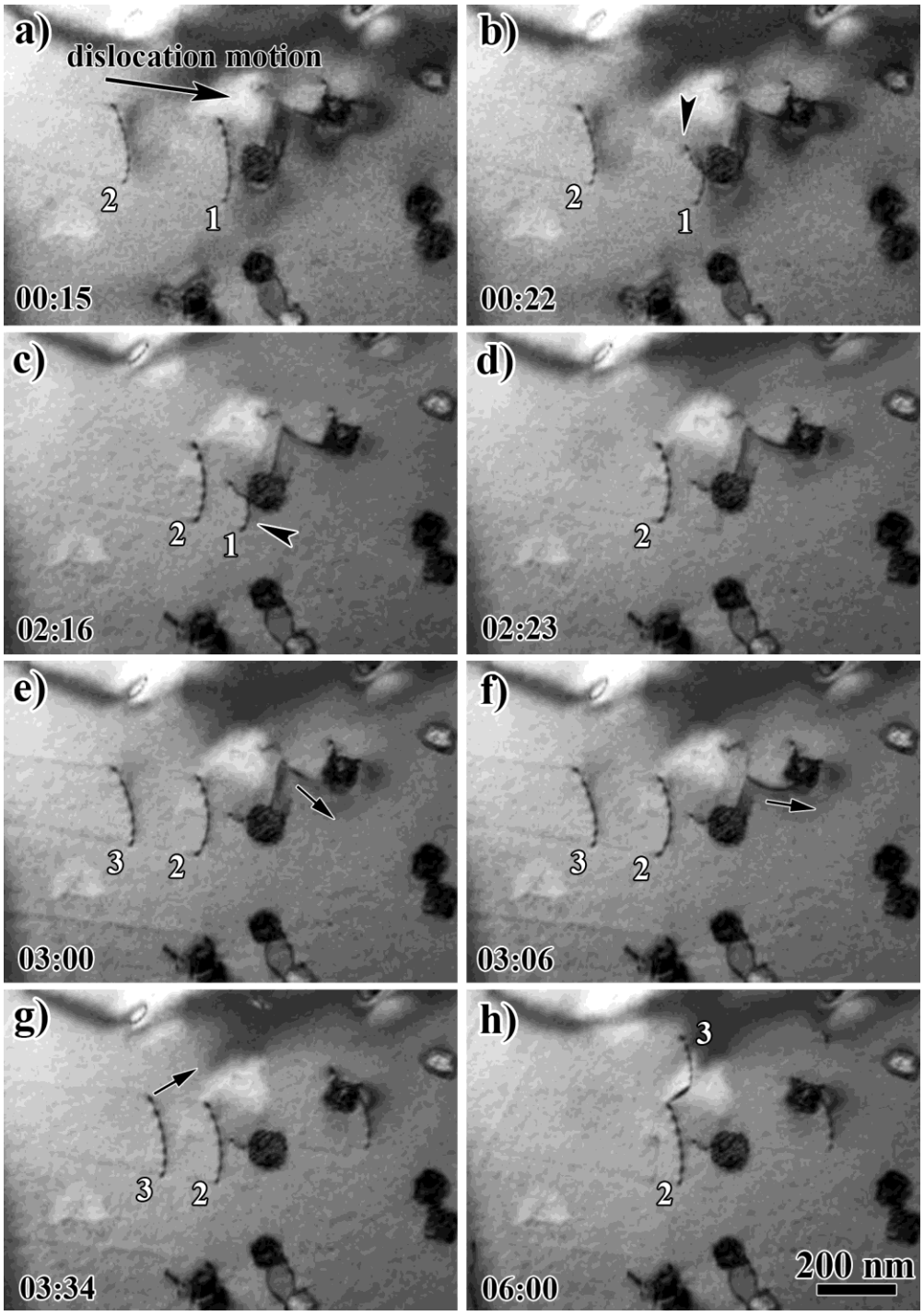

Fig. 4.6. Interaction of pile-up dislocations with a Co particle involving (a) an initial strong elastic interaction followed by (b) cross-slip (arrowhead) and (c) accommodation (arrowhead) in the particle-matrix interface. Interaction with subsequent dislocations was elastic and bypass occurred by double cross-slip, (d)-(h). See text for details.

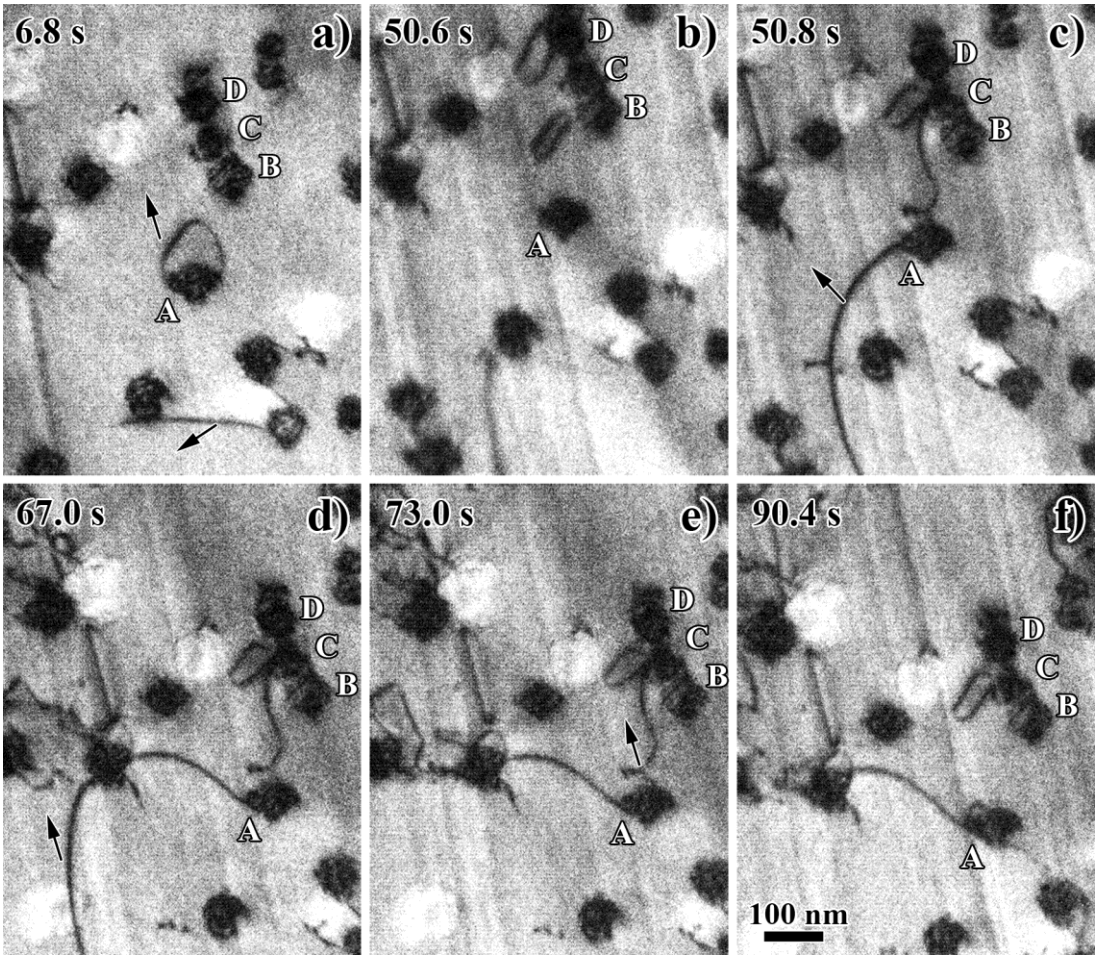

Fig. 4.7. (a) Break-away of a dislocation half-loop around a Co particle, labeled 'A,' accompanied by (b)-(c) reorientation and creation of a loop attached on one side to a neighboring particle and (d)-(f) the cross-slip of a single dislocation segment pinned on one end at the particle interface. See text for details.

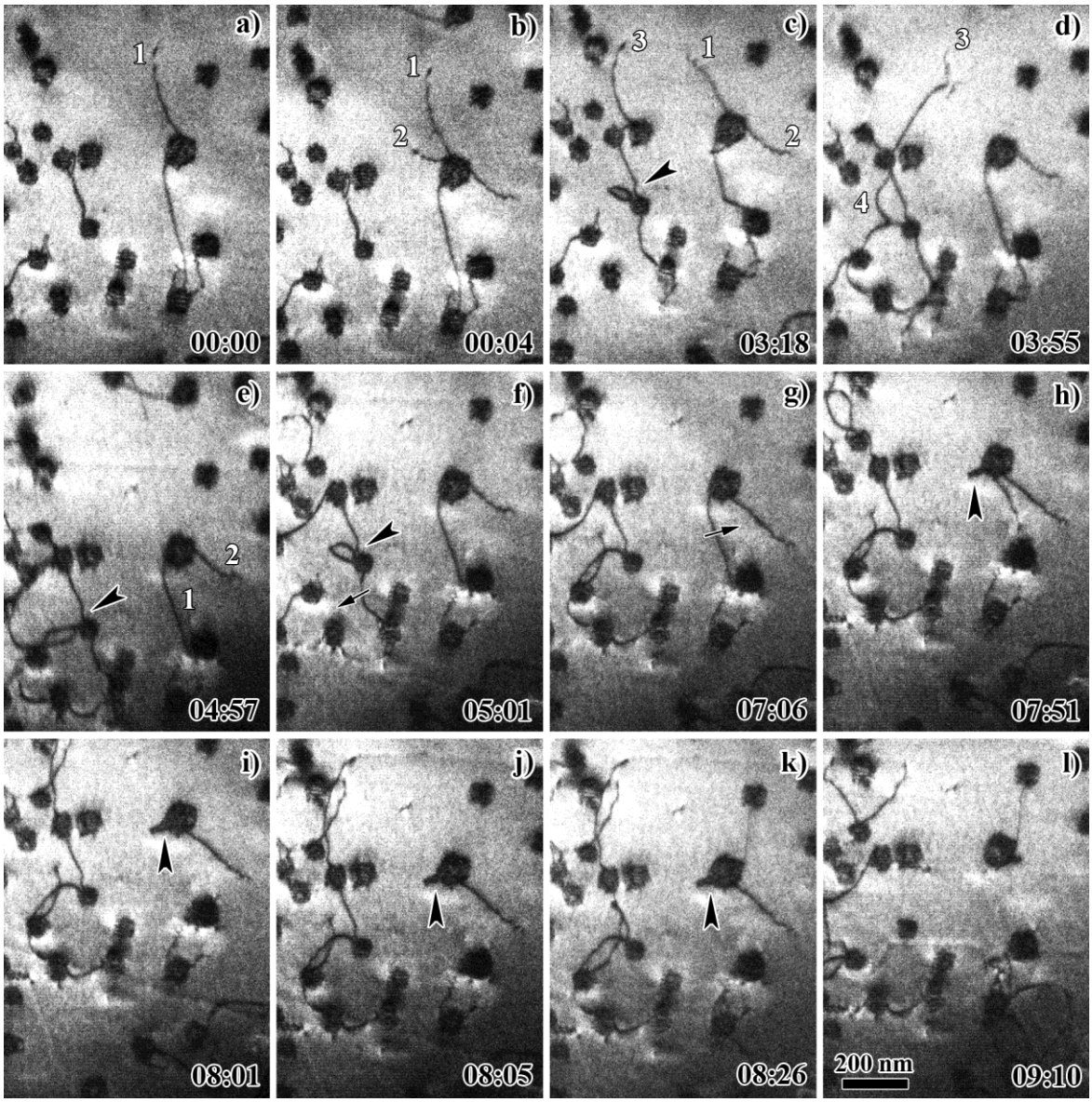

Fig. 4.8. Dislocation-particle interaction in Cu-Co resulting in the creation and annihilation of attached loops to one side of a particle, indicated by arrowheads. See Fig. 4.9 and text for further details.

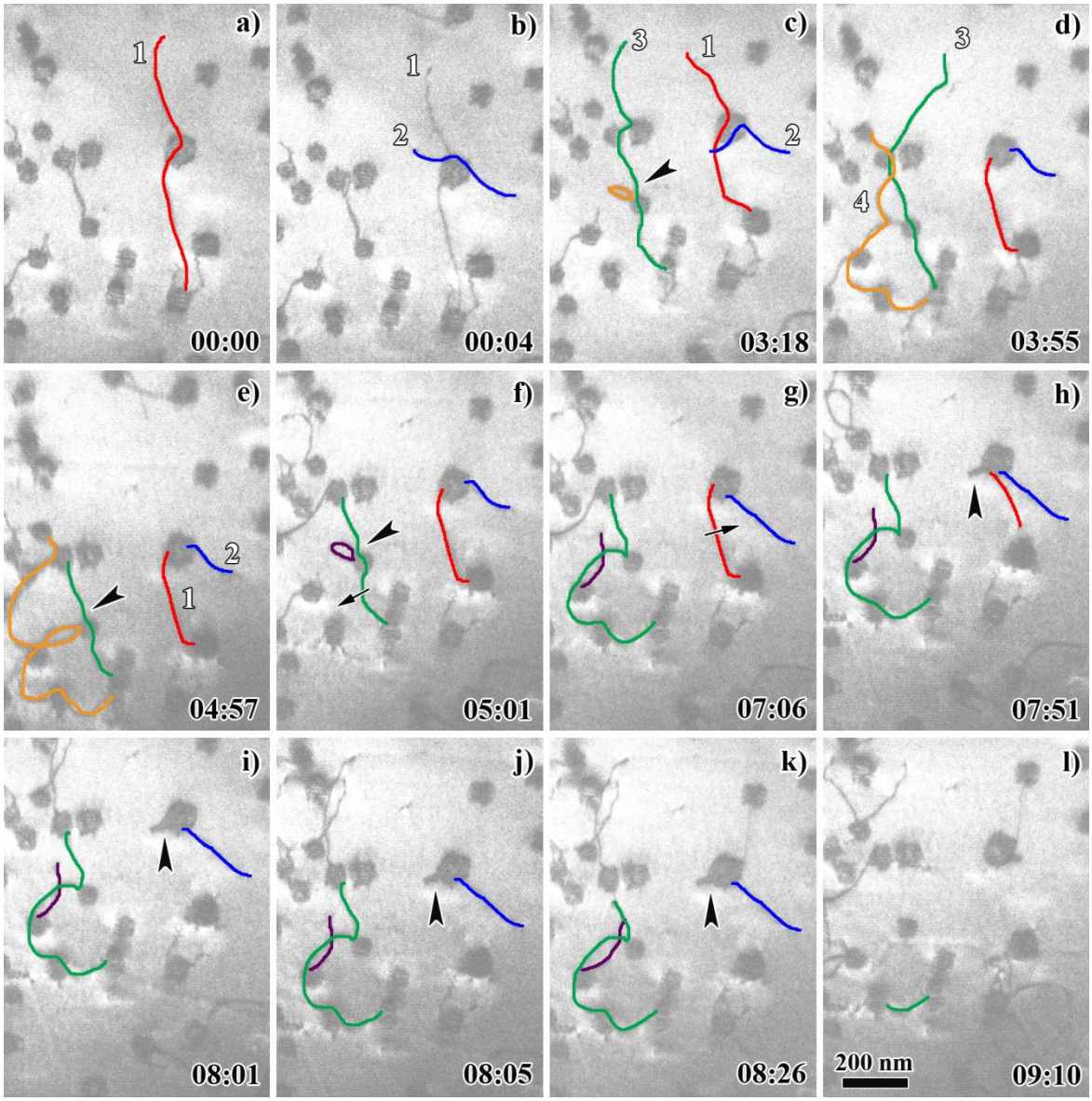

Fig. 4.9. A schematic of the dislocation-particle interactions captured in Fig. 4.8 superimposed over the video still frames. Two sets of interactions take place: dislocations '1' and '2' (in red and blue, respectively) interact with each other while pinned at a the same particle; and dislocations '3' and '4' (green and orange, respectively) interact with each other as well as with the products of previous reactions (in purple) near seven different particles. See text for details.

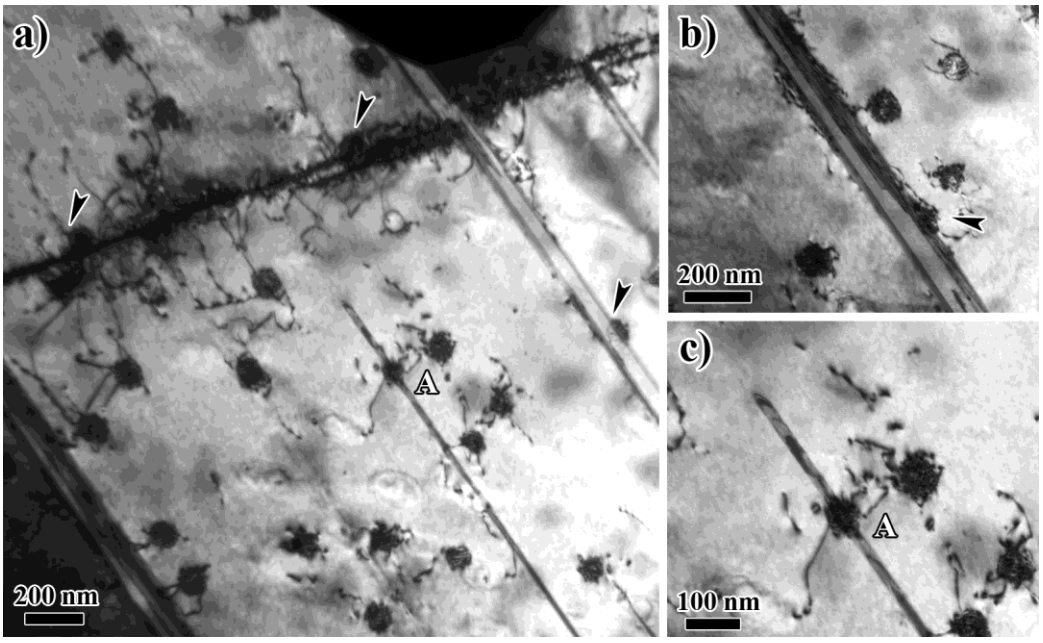

Fig. 4.10. (a) A heavily-twinned region after *in situ* straining of Cu-Co showing Co particles sheared by small twins; a magnified view around particle 'A' is magnified in (c). (b) Multiple shearing of the same particle (arrowed) by a number of twins. Compare with the interaction shown in Fig. 4.6, more typically observed in *in situ* experiments, in which cross-slip rather than shear served as the principal mechanism of bypass.

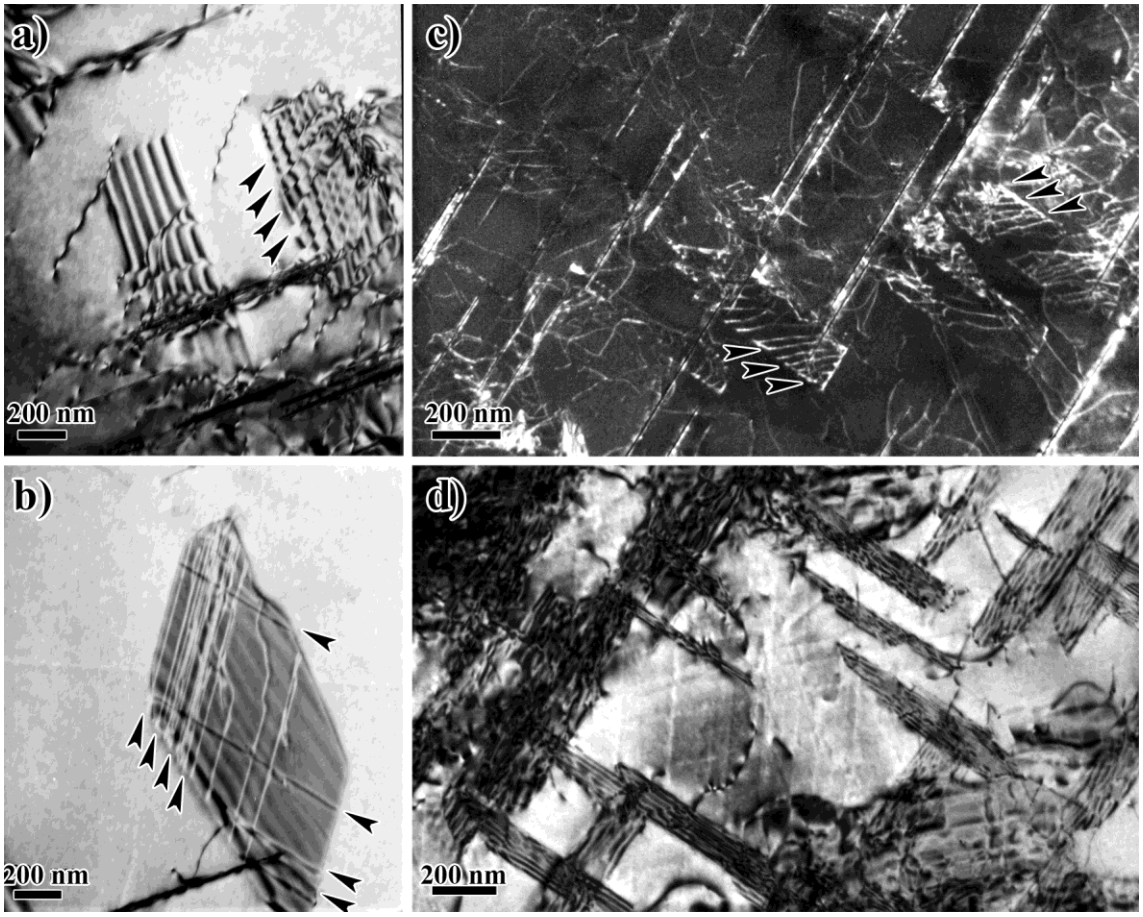

Fig. 4.11. Types of dislocation-particle interactions revealed by *post mortem* observation of Al_2Cu plate particles. (a)-(b) under low local strain dislocations on parallel slip-planes shear the plates from the coherent side and (c) with increasing strain matrix dislocations enter and experience diminished mobility in the interface before (d) multiple-slip produces a complex dislocation cell-like network with plates as boundary walls. See text for further details.

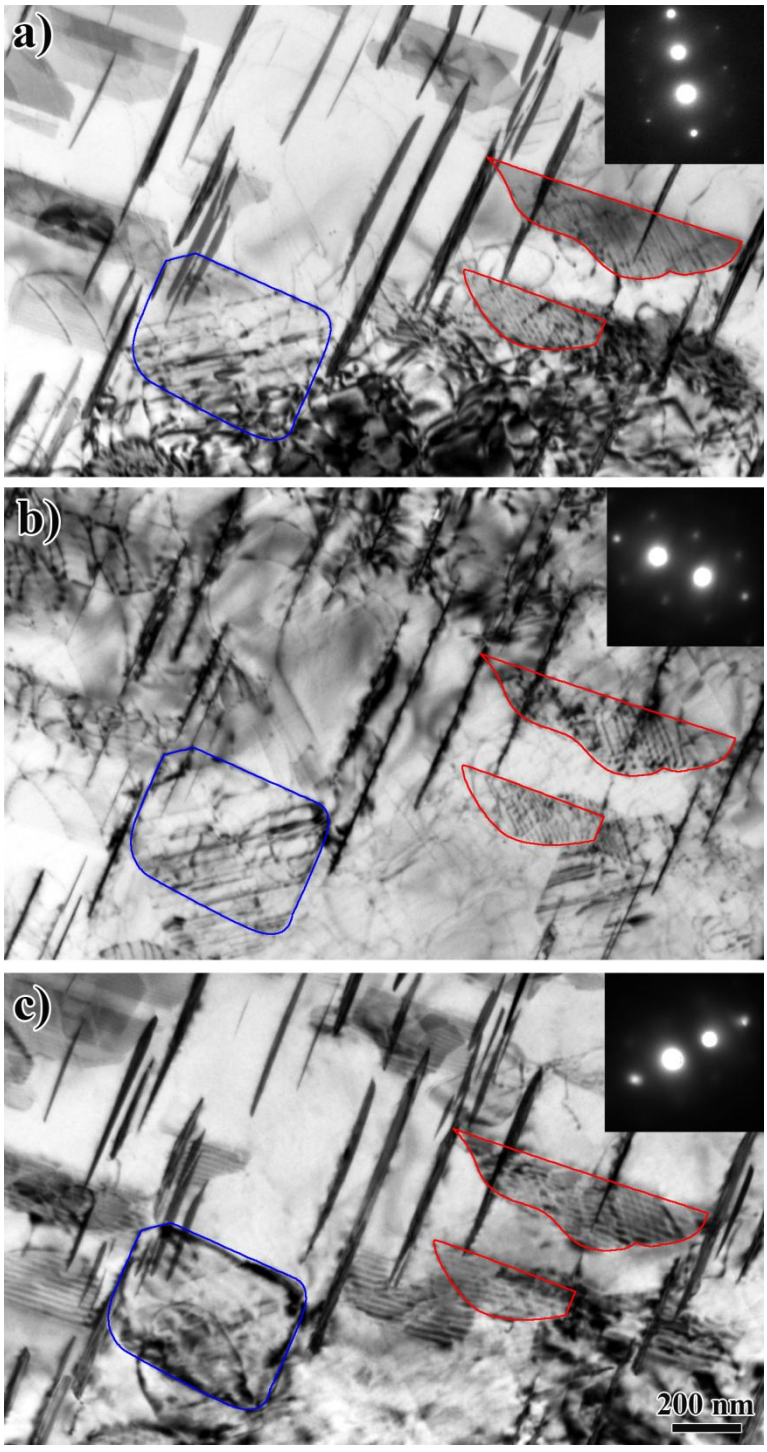

Fig. 4.12. g · b analysis of lattice dislocations in the interface after deformation using bright-field images under (a) g = $\bar{1}\bar{1}1$, (b) g = 020, and (c) g = $\bar{1}11$. The particle outlined in blue resides on an {001} plane and has interfacial dislocations with a Burgers vector of b = $a/2[110]$; particles outlined in red reside on {100} planes and have interfacial dislocations with a Burgers vector of b = $a/2[01\bar{1}]$.

Fig. 4.13. Path of a crack propagating through a field of Al_2Cu plates. The arrow indicates the original crack opening direction, which was deflected as separation occurred in the matrix region in between plates.

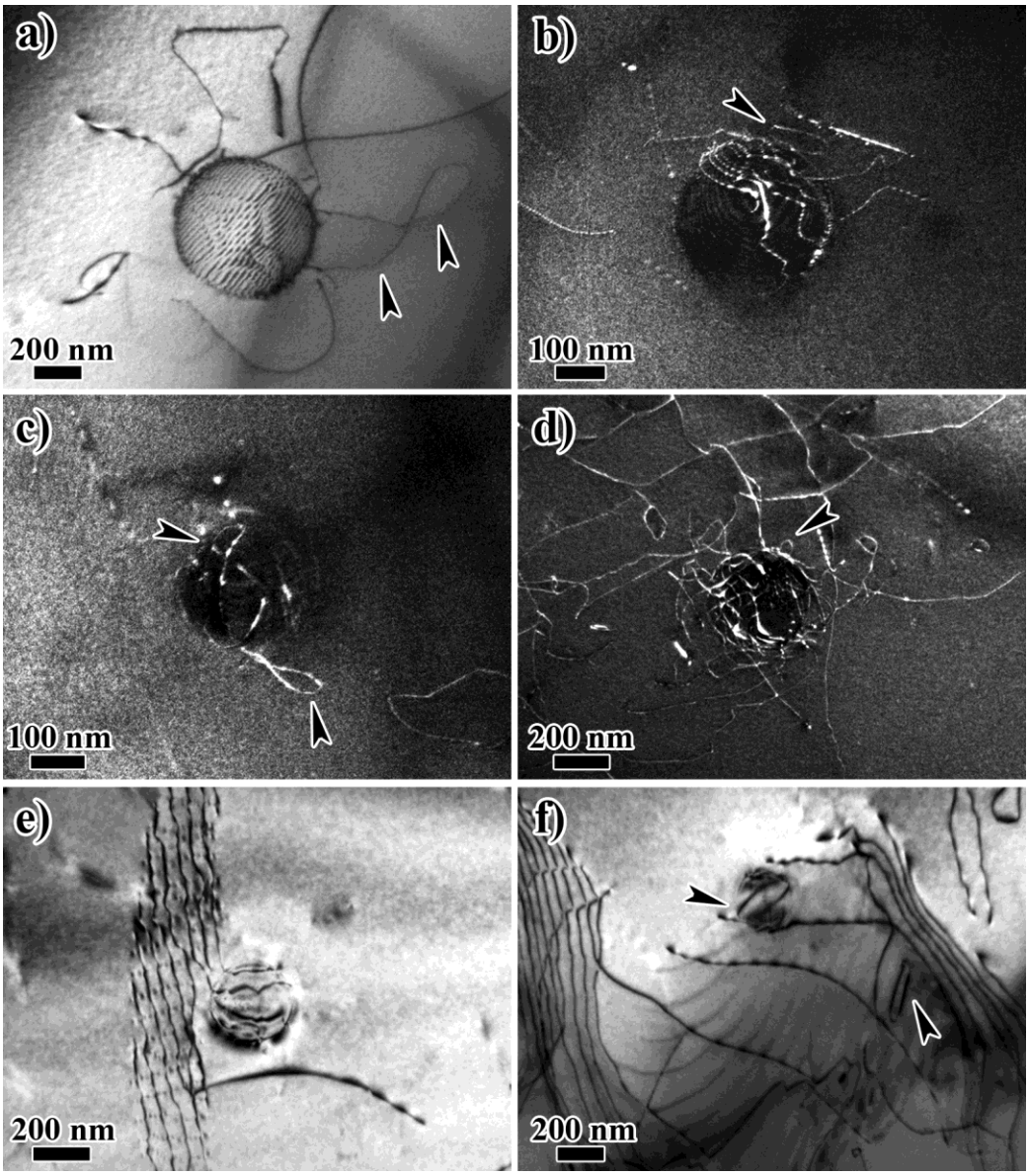

Fig. 4.14. Types of dislocation-particle interaction revealed by *post mortem* observation of Al_3Sc particles where (a) half-loops pinned at the ends undergo cross-slip, (b)-(c) full loops are created with one side attached to the interface, resulting in (d) a complex network of matrix and interfacial dislocations surrounding the particle. (e)-(f) Interaction involving dislocation arrays produce aligned interfacial features and debris.

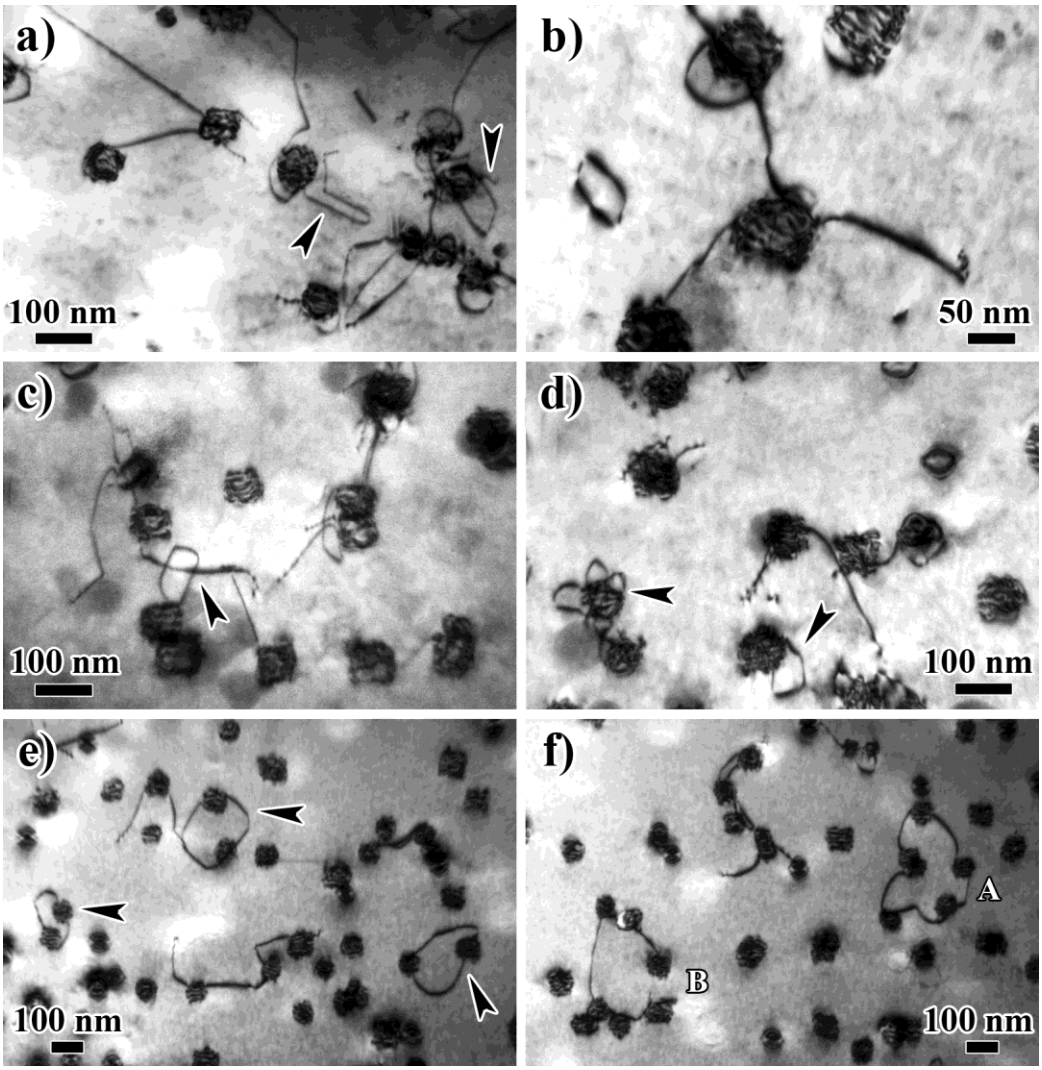

Fig. 4.15. Examples of dislocation-particle interaction revealed by *post mortem* observation of Co particles where (a) cross-slip bypass of particles is believed to produce either (b) standalone loops or as was more commonly observed, (c)-(d) loops attached on one side to the particle interface. Occasionally, such loops may encompass (e)-(f) multiple particles or be 'broken' due to one segment breaking free.

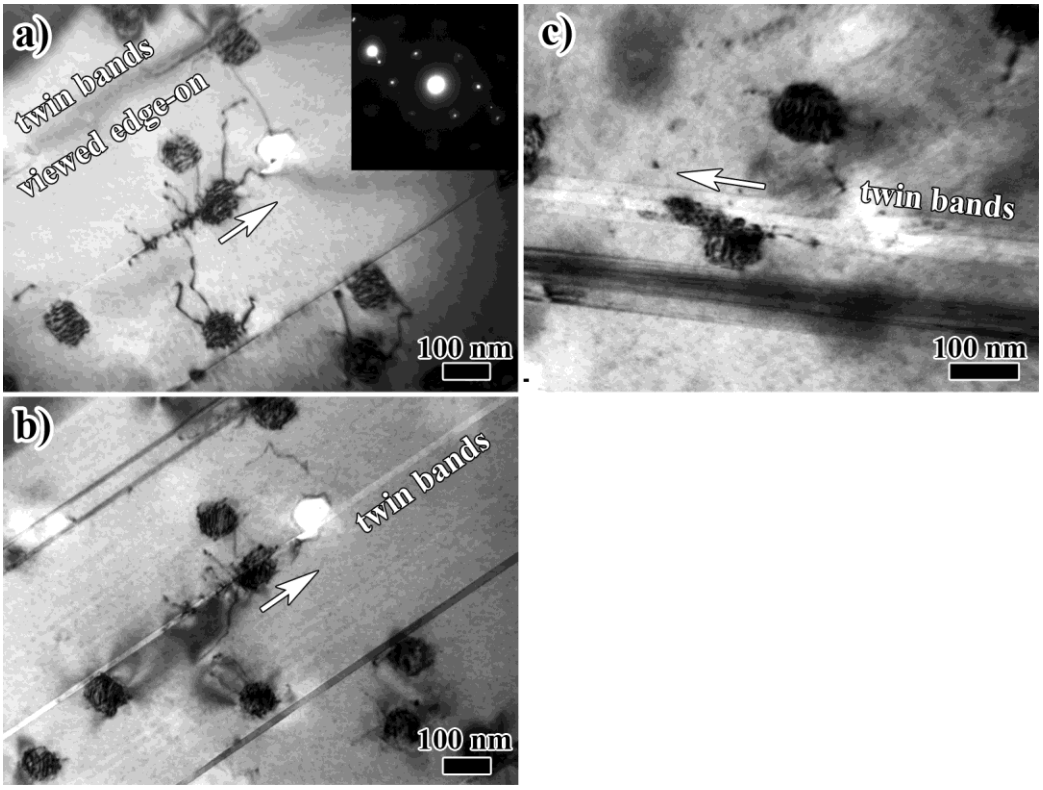

Fig. 4.16. (a)-(b) A different type of interaction involving the shearing of Co particles by twinning dislocations. The twin bands, always very thin, are occasionally observed to extend through the shearing plane, between two halves of displaced Co [111]. (c) Sometimes a single particle was found to be sheared multiple times. See also Fig. 4.10.

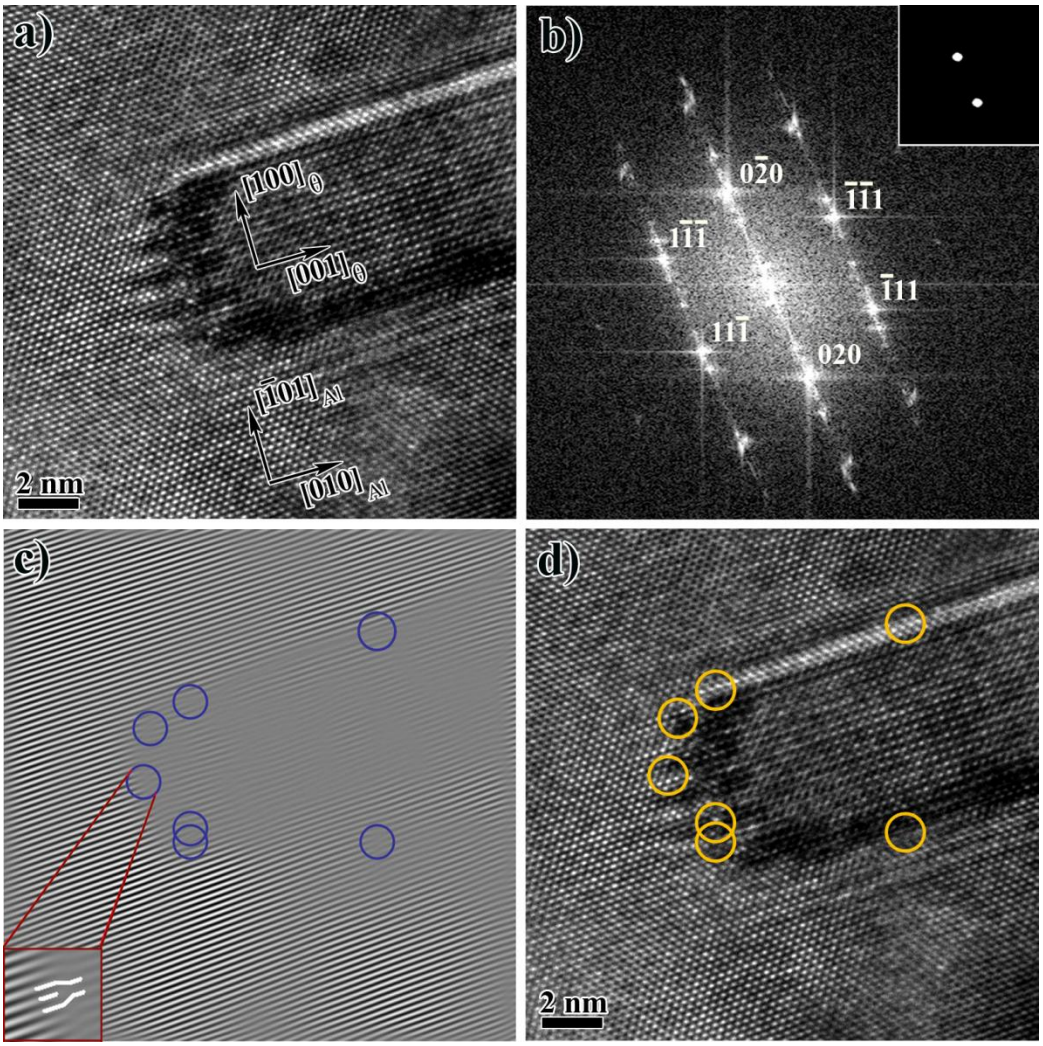

Fig. 4.17. Particle-matrix interface coherency of an Al_2Cu platelet revealed by high-resolution microscopy and fast Fourier transform: (a) HRTEM image of the platelet at $[101]_{Al}$ // beam direction. (b) FFT of (a) where all but one pair of spots, ±020, are masked out as shown in the inset. (c) Inverse FFT of (b)-inset, producing a planar image where interruptions, circled in blue, indicate interfacial dislocations. (d) The locations of the interfacial dislocations overlaid back onto (a), where the higher degree of particle misfit along the $[100]_\theta$ side compared to $[001]_\theta$, or particle growth direction, is clearly visualized.

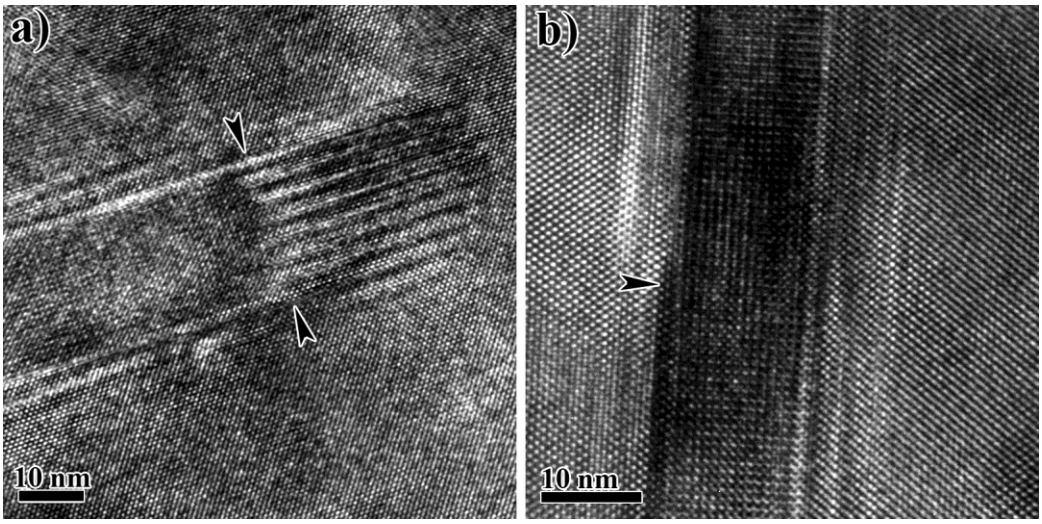

Fig. 4.18. High-resolution images of Al_2Cu plates (a) normal to the primary plate-growth direction with electron beam // $[010]_\theta$, where the particle-matrix interface is non-coherent and exhibits contrast disruptions resulting from growth ledges, arrowed. (b) The particle interface along the primary growth direction, however, is nearly fully coherent except for a few growth ledges.

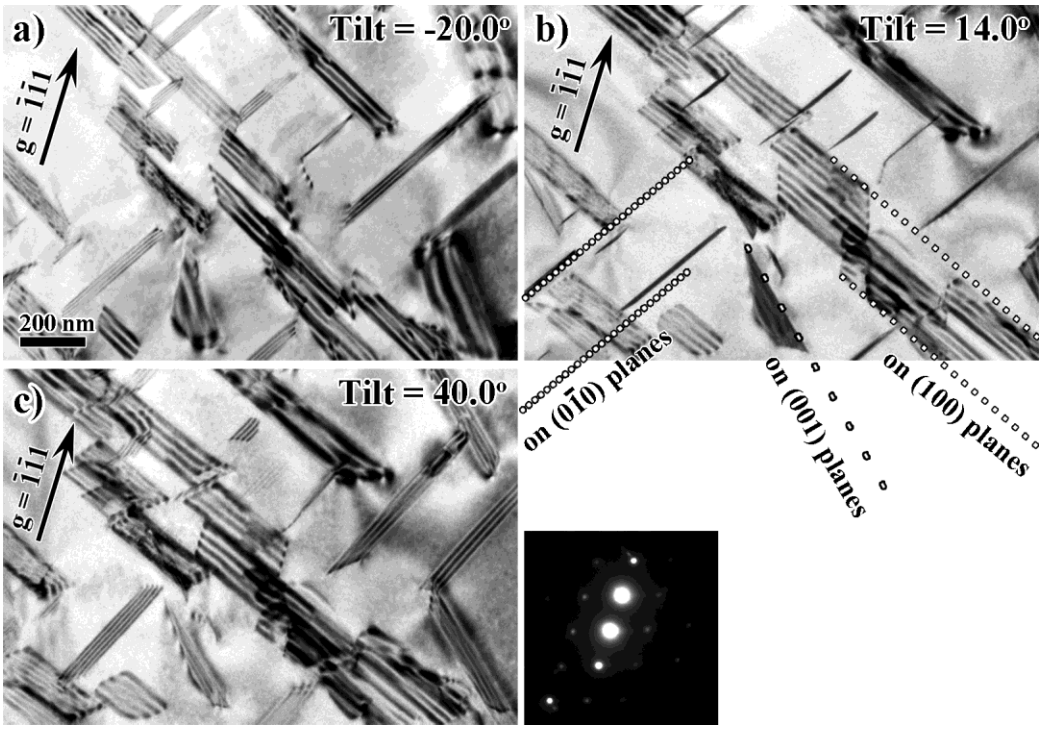

Fig. 4.19. Kinematical bright-field images of Al_2Cu particles from a tilt series spanning ±40° captured using g = $\bar{1}\bar{1}1$ where (a) was taken at -20.0°, (b) was taken at 14.0°, and (c) was taken at 40.0°. The three families of θ-plates are identified by their projected particle growth directions and indicated by dashed lines. The traced tomographic reconstruction from this series is presented in Fig. 4.20.

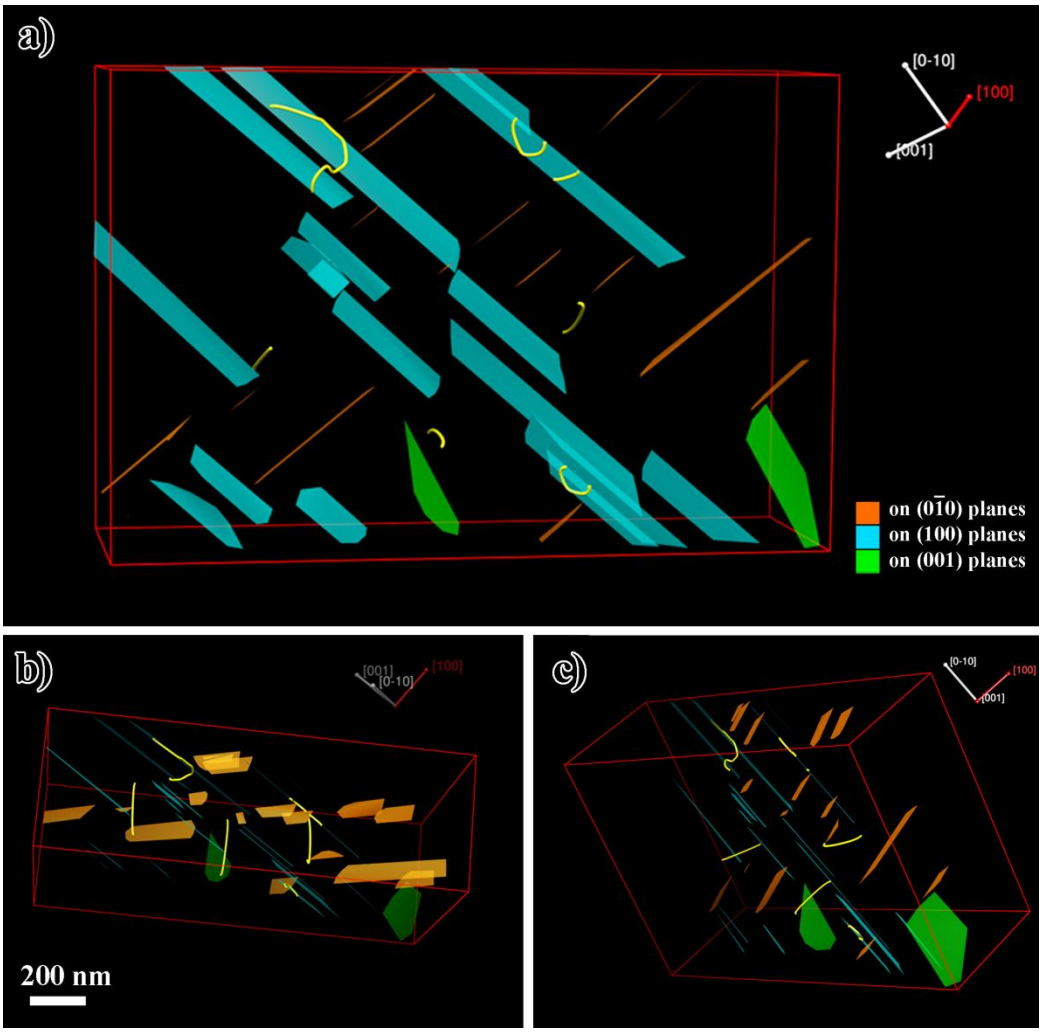

Fig. 4.20. Spatial and orientation relationship between Guinier Type I Al_2Cu platelets prior to deformation obtained using electron tomography and colored according to habit plane families. (a) A near-$[\bar{2}\bar{1}\bar{2}]$ view, similar to Fig. 4.19(a), of the traced tomographic reconstruction which shows much improved detail; (b) An $[0\bar{2}\bar{1}]$ view and (c) an $[00\bar{1}]$ view.

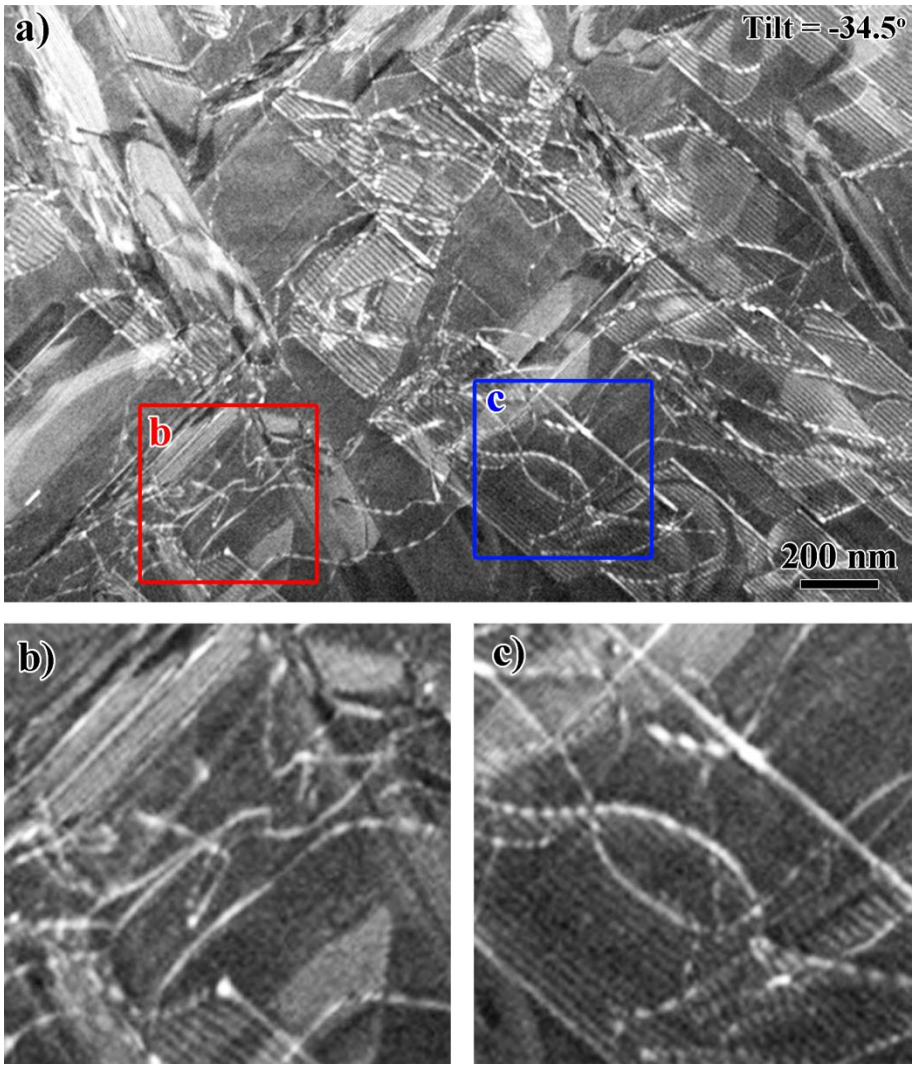

Fig. 4.21. (a) A (g, 3g) weak-beam dark-field image of post-deformation Al-Cu from a tilt series spanning 62.0° captured using g = $11\bar{1}$. Two regions, one showing a complex arrangement of lattice dislocations in between particles (red box) and the other showing a large loop residing in a particle interface (blue box) are highlighted and magnified in (b) and (c), respectively. The traced tomographic reconstruction from this series is presented in Fig. 4.22.

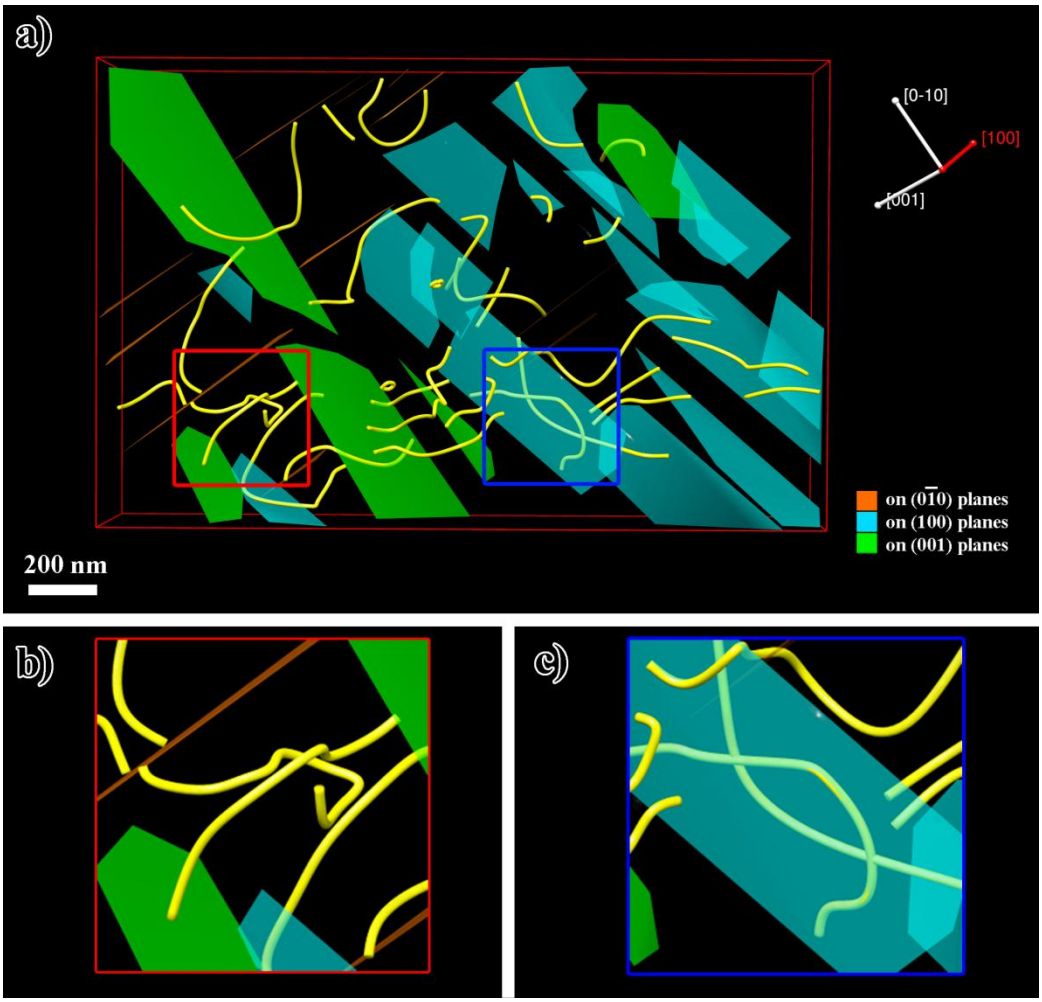

Fig. 4.22. Spatial and orientation relationship of dislocations surrounding Al_2Cu particles after deformation, obtained using electron tomography. (a)-(c) A near-$[\bar{1}0\bar{1}]$ view with the same regions as Fig. 4.21 highlighted and magnified in (b) and (c). (d)-(f) A near-$[0\bar{1}\bar{1}]$ view of the traced model, magnified in (e) and (f); and (g)-(i) a near-$[\bar{1}\bar{1}0]$ view, magnified in (h) and (i). See text for details.

Figure 4.22 (cont.)

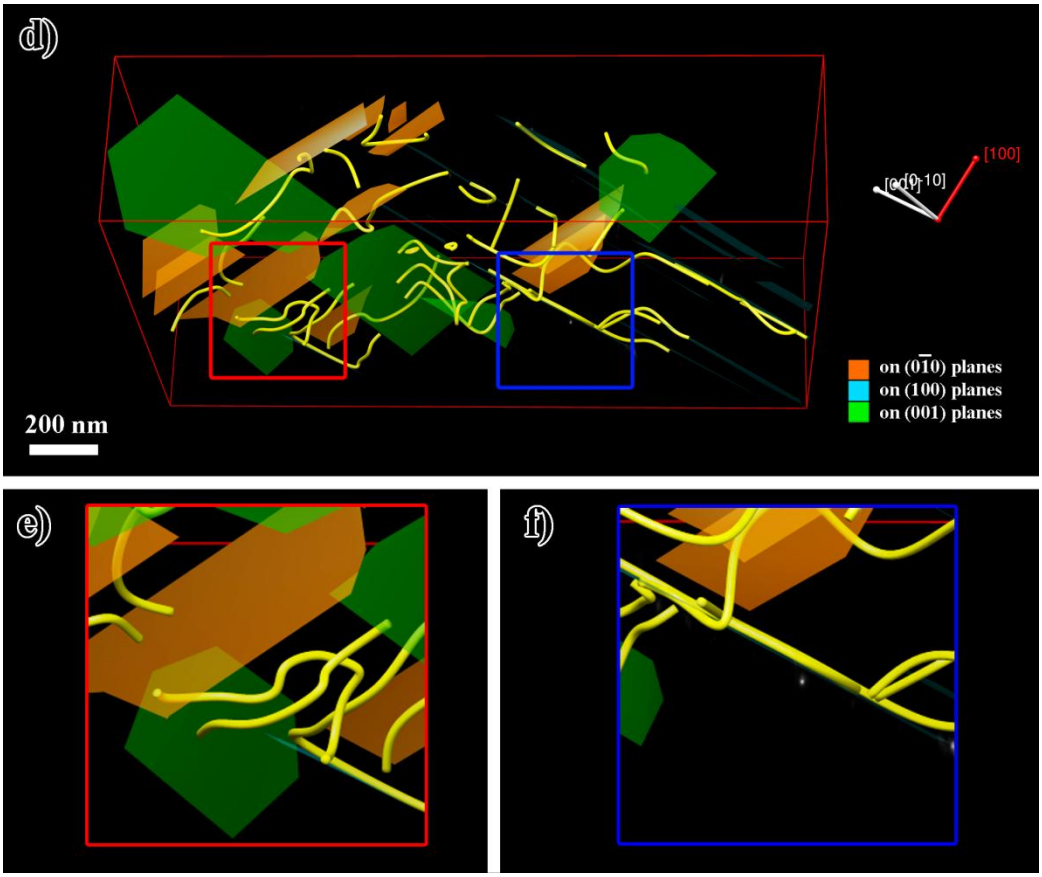

Fig. 4.22. Spatial and orientation relationship of dislocations surrounding Al_2Cu particles after deformation, obtained using electron tomography. (a)-(c) A near-$[\bar{1}0\bar{1}]$ view with the same regions as Fig. 4.21 highlighted and magnified in (b) and (c). (d)-(f) A near-$[0\bar{1}\bar{1}]$ view of the traced model, magnified in (e) and (f); and (g)-(i) a near-$[\bar{1}\bar{1}0]$ view, magnified in (h) and (i). See text for details.

Figure 4.22 (cont.)

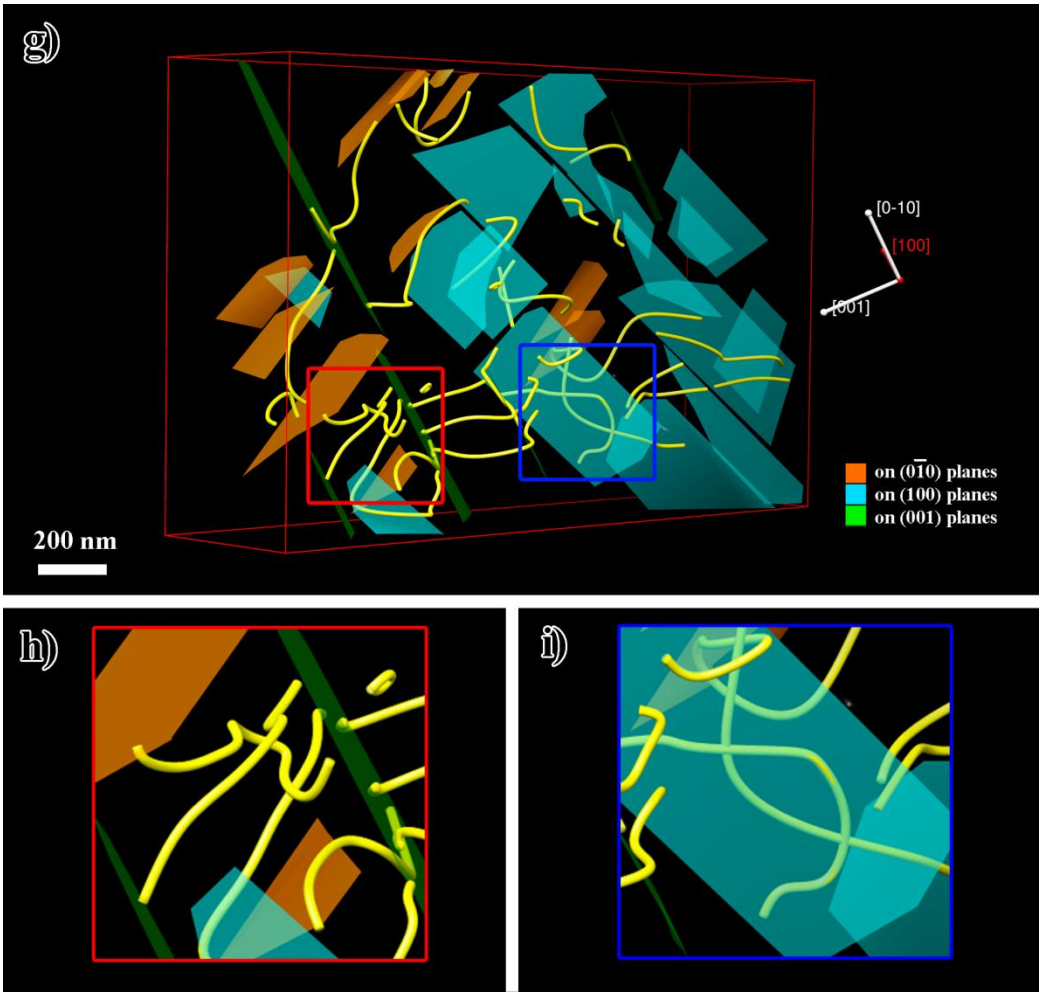

Fig. 4.22. Spatial and orientation relationship of dislocations surrounding Al_2Cu particles after deformation, obtained using electron tomography. (a)-(c) A near-$[\bar{1}0\bar{1}]$ view with the same regions as Fig. 4.21 highlighted and magnified in (b) and (c). (d)-(f) A near-$[0\bar{1}\bar{1}]$ view of the traced model, magnified in (e) and (f); and (g)-(i) a near-$[\bar{1}\bar{1}0]$ view, magnified in (h) and (i). See text for details.

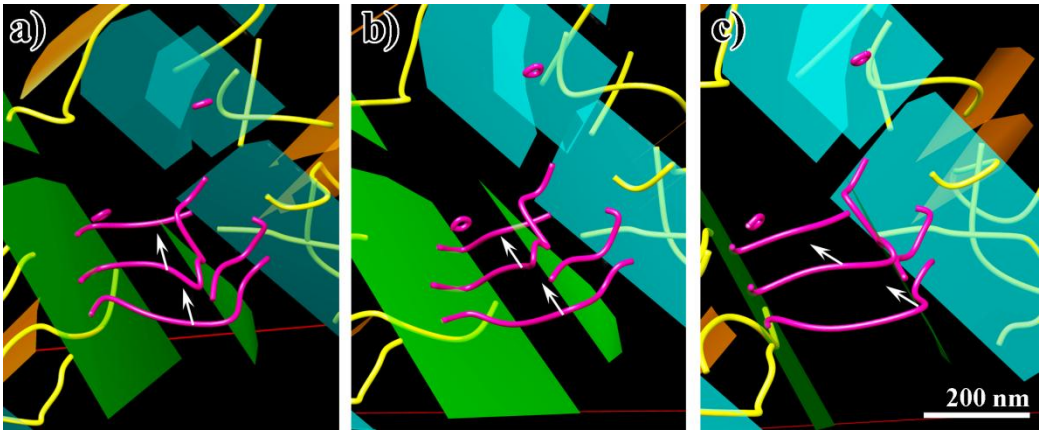

Fig. 4.23. (a)-(c) Three different views of dislocations (colored magenta) bowing around a small {001} plate, colored green, located at the center of the images, where the direction of dislocation motion is indicated by arrows. Short segments along the dislocations' length appear to reside close to or on the particle interface.

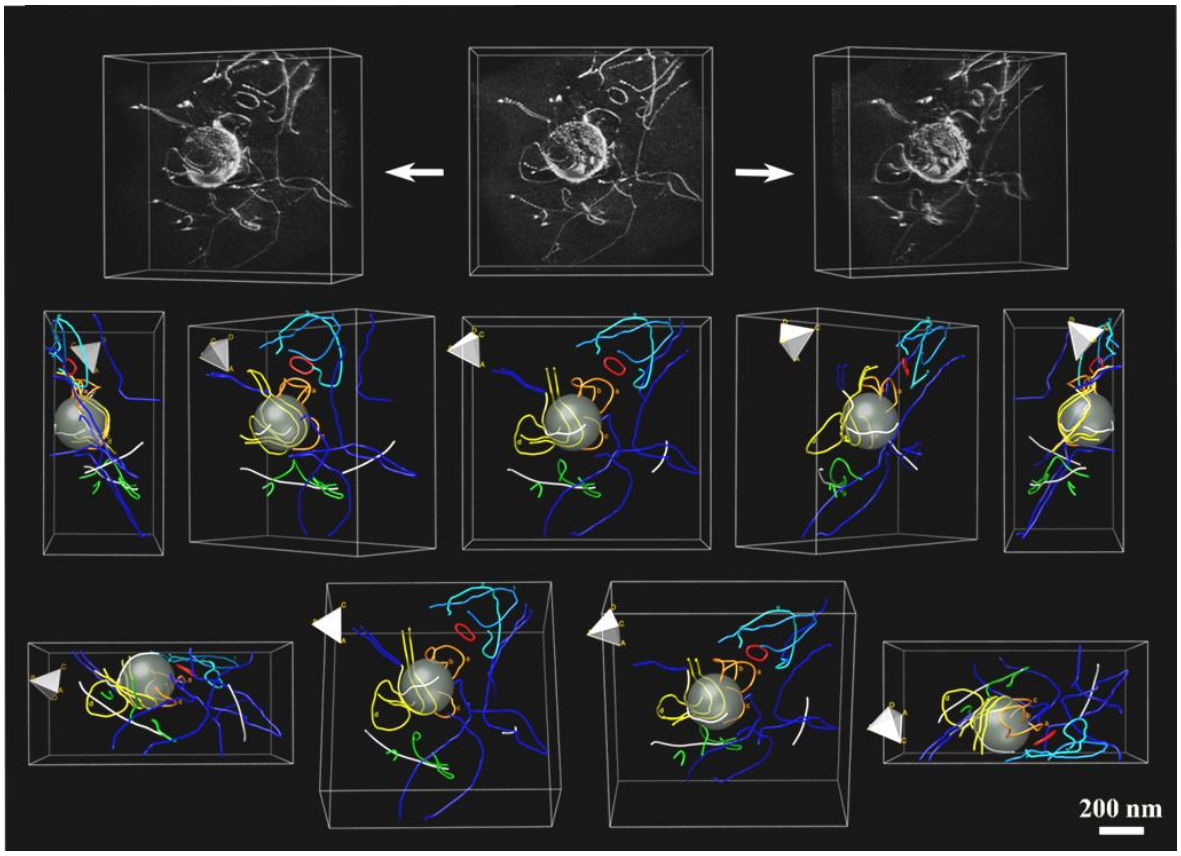

Fig. 4.24. Spatial and orientation relationship of dislocations surrounding an Al_3Sc particle after deformation, produced from a tilt series spanning 60°. (top row) Three views of the reconstructed tomogram and (middle row)-(bottom row) rotated views of the traced dislocation structure model, showing the complexity of the dislocation structures present. All colored dislocations have the same Burgers vector, b = $a/2[1\bar{1}0]$. See text for details.

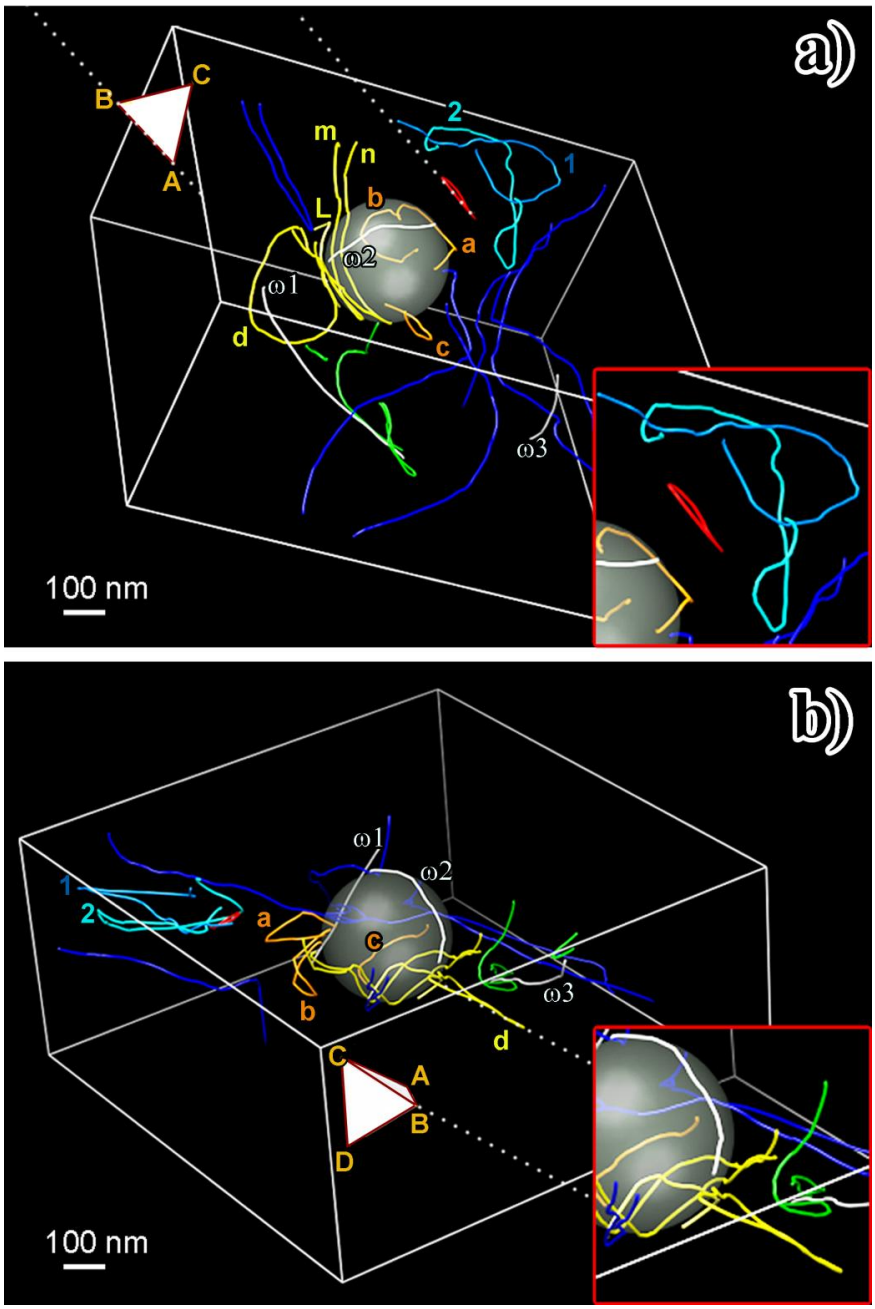

Fig. 4.25. Alternate views from the same traced model as Fig. 4.24, highlighting (a) a standalone dislocation loop (colored red) residing on the γ-plane to one side of the Al_3Sc particle and (b) an attached loop (colored yellow and labeled 'd') residing on the δ-plane. Insets show enlargements of the regions surrounding the loops. See text for details.

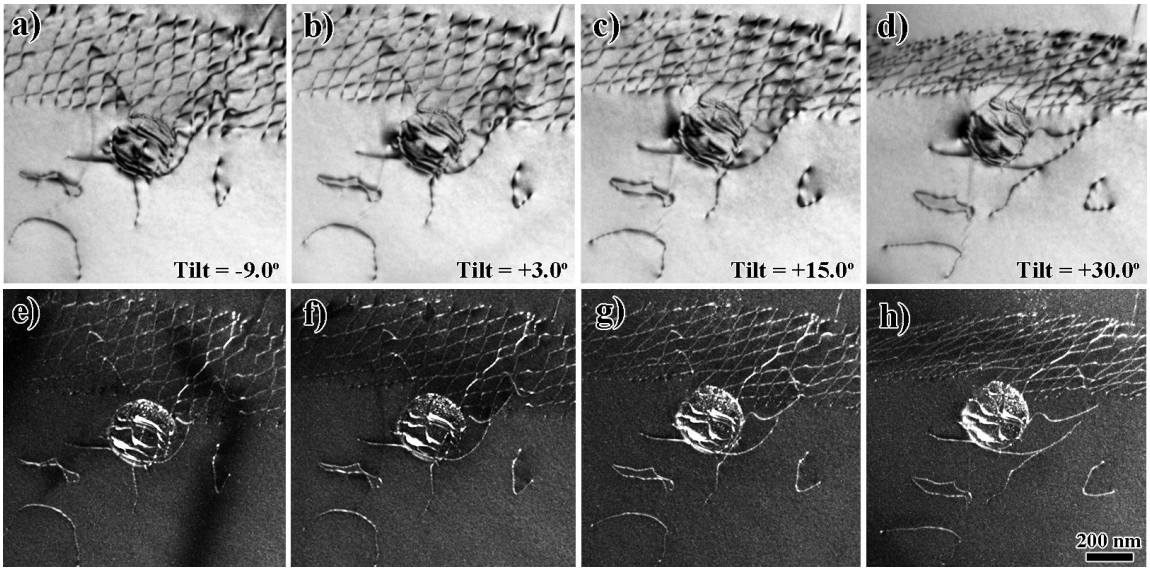

Fig. 4.26. Micrographs showing the post-interaction microstructure between a twist boundary and an Al_3Sc particle using g = 020. (a)-(d) Two-beam bright-field micrographs taken at -9.0°, 3.0°, 15.0°, and 30.0°-tilt, respectively; and (e)-(h) (g, 3g) weak-beam dark-field micrographs taken at the same title values belonging to a tilt series spanning 59°. See text for details.

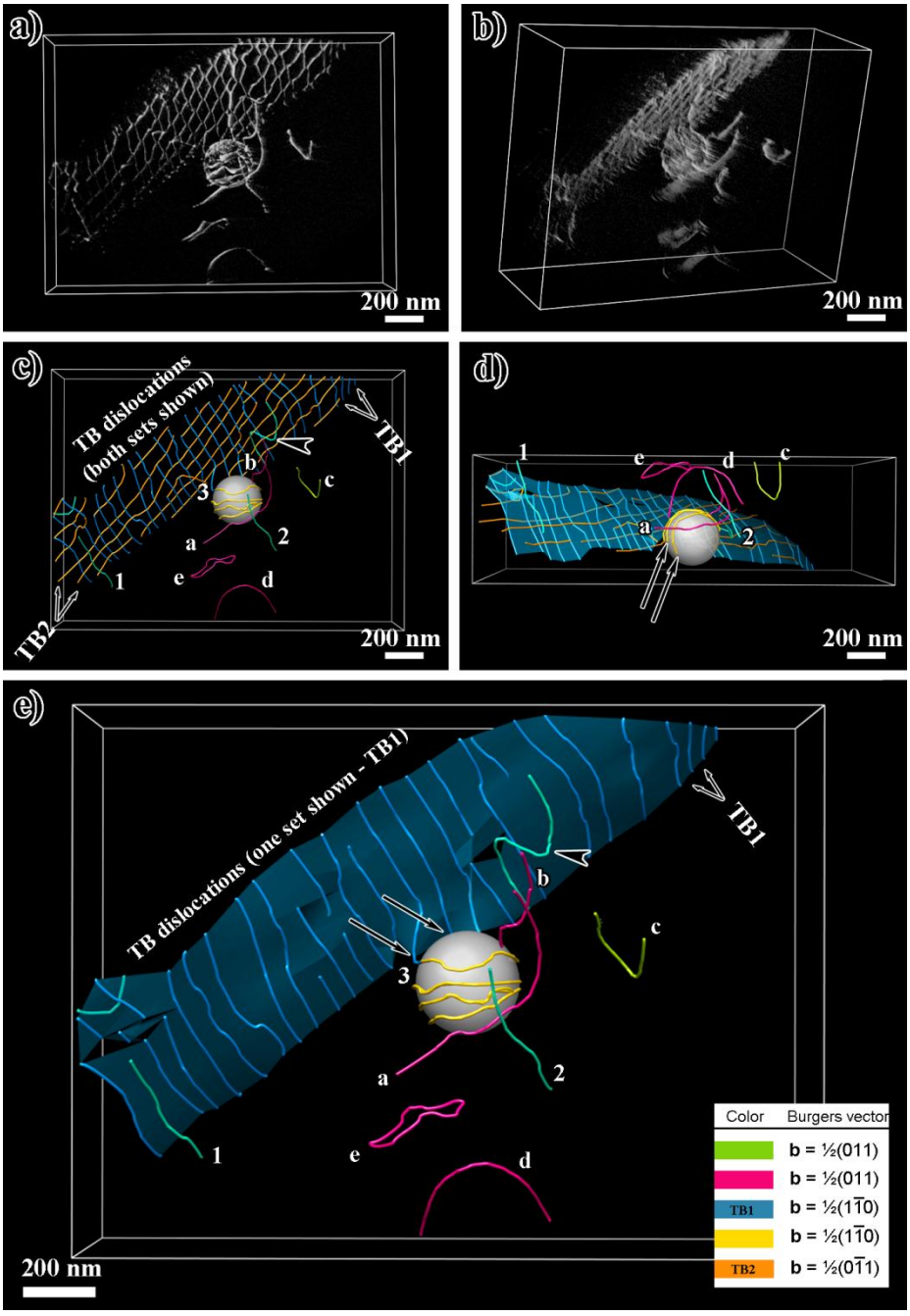

Fig. 4.27. Spatial and orientation relationship of a twist boundary interacting with an Al_3Sc particle obtained from the tilt series represented in Fig. 4.26(e)-(h). (a)-(b) Views extracted from the tomographic reconstruction and (c)-(d) the traced dislocation structure model, where individual dislocations are colored by Burgers vector. See text for details.

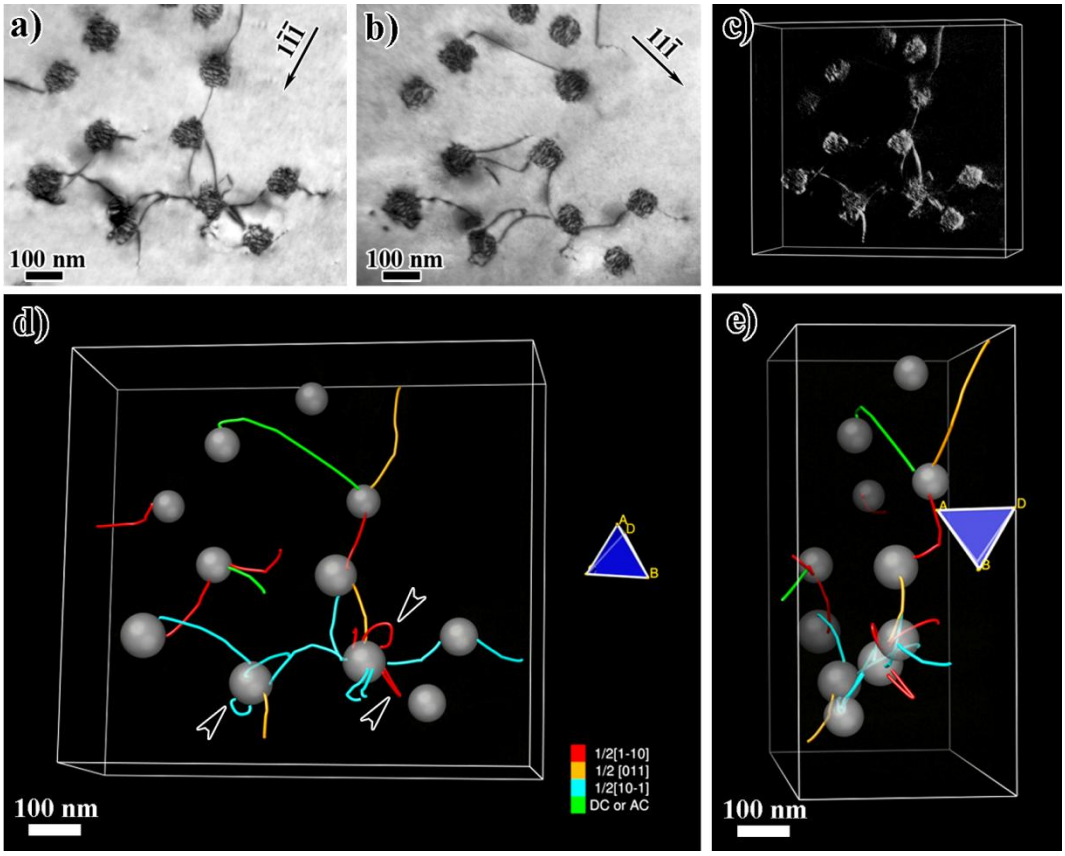

Fig. 4.28. Spatial and orientation relationship of dislocations interacting with Co-rich particles, obtained from dual-axes electron tomography using (a) g = $1\bar{1}\bar{1}$ and (b) g = $11\bar{1}$. (c) The reconstruction served and (d)-(e) the traced dislocation structure model, where the dislocations are colored by Burgers vector. Several attached loops are found at the particle interfaces, denoted by arrowheads.

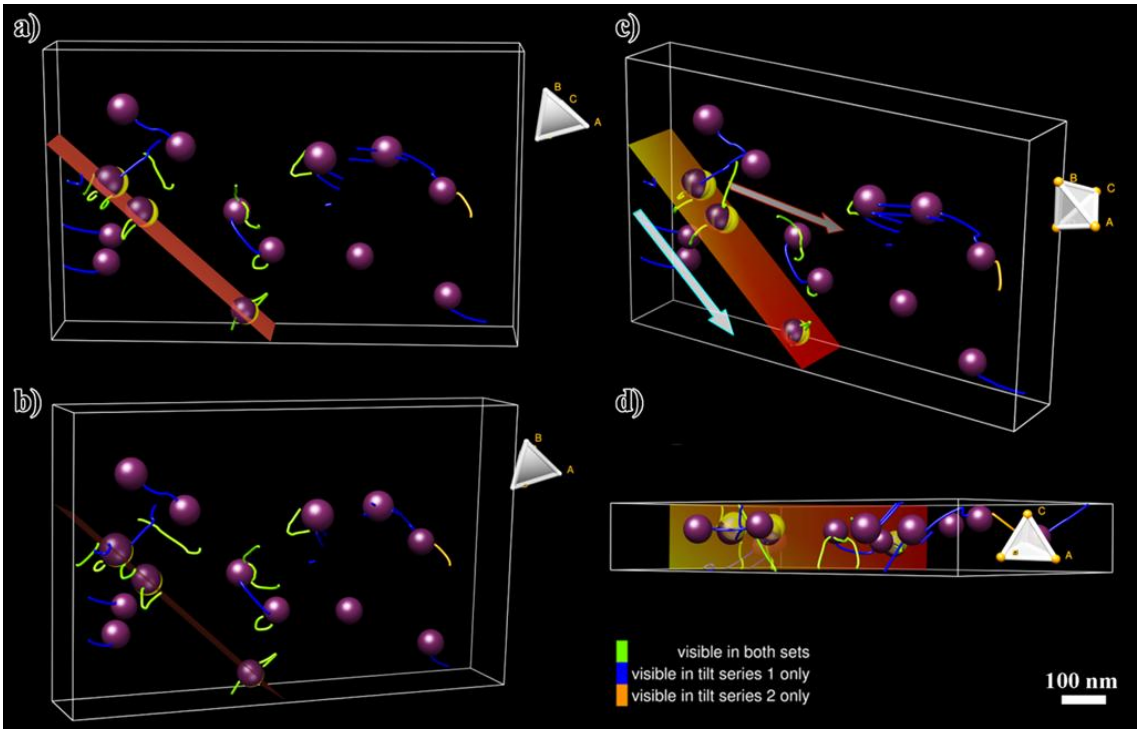

Fig. 4.29. Views from a dual-axes traced model of intact and sheared Co particles captured using $\mathbf{g} = \bar{2}20$ and $\mathbf{g} = 0\bar{2}0$. The original, or unsheared particle locations are represented by purple markers and the displaced, or sheared particle locations by yellow markers. See text for details.

CHAPTER 5

DISCUSSION

Using a number of analytical techniques, dislocation-particle interactions in three alloy systems containing different types of particles have been investigated: Al_2Cu platelet particles in Al-4Cu and Al-4.5Cu; Al_3Sc spherical particles in Al-4Mg-0.3Sc and Al-0.3Sc; and Co octahedral particles in Cu-2Co and Cu-3Co. The results of *in situ* straining experiments, *post mortem* observations and spatially-resolved volume reconstructions using electron tomography will be discussed in this chapter with respect to material parameters such as particle size, interface coherency, and particle geometry; as well as taking into account external variables normally overlooked in computer models such as deformation and strain over time. The implications of these findings in providing new insights for particle-strengthening models will be discussed in each section in the context of previous work; and finally, concluding with some remarks on the development of diffraction-contrast electron tomography and its potential to enhance the study of other materials systems in the future.

5.1 Influence of Material Characteristics on Dislocation-Particle Interactions

Several types of particles were studied in order to elucidate the operating mechanisms in room temperature dislocation-particle interactions as a function of material characteristics such as particle size, interface coherency, and particle geometry. Although particle crystal structure often differed from that of the matrix, its influence is only in terms of elastic interactions (stemming from differences in lattice parameter, shear and elastic

moduli, and Poisson's ratio) and when particle cutting produces a faulted interface such as an antiphase boundary or stacking-fault. Since the rate-limiting steps in the observed interactions were not purely elastic, and that particle cutting occurred under special circumstances, the discussion will focus on particle parameters such as size, shape, and interfacial structure as related to coherency.

Classical models of dislocation-particle interactions typically consider spherical, isotropic particles and only predict a limited number of possible interactions such as Orowan looping [24], Hirsch prismatic looping [29-30] or particle cutting. Literature reviewed in Chapter 2 as well as results from this work both support the idea that the classical models constitute only a subset of the possible interactions because many important factors were not accounted for. For this study, the various alloy systems were chosen such that the contribution of some of these factors may be better understood: Al_2Cu plates have the highest anisotropy but the broad side interface is the most coherent; Al_3Sc particles have a classical spherical geometry but develop a complex interfacial dislocation network when particle sizes are large; and Co particles are octahedral in shape while also exhibiting interfacial dislocations at the sizes tested.

5.1.1 Effect of Particle Size and Interface Coherency

Particle size was found to have limited effect on the dislocation bypass mechanisms beyond the coherent regime, around 20-30 nm for both Al_3Sc and Co particles. Prior to this dimension, dislocations bypass both types of particle via shearing on the intersecting slip plane [44]. With increasing particle size, beyond 40 nm and up to more than 200 nm for

Al_3Sc particles and 100 nm for Co particles, they are considered to be *semi-coherent* and their interaction with lattice dislocations also share some key features:

- An initial elastic interaction between an incoming dislocation and the semi-coherent particle, Figs. 4.5 and 4.6;
- Contact between the dislocation and the particle interface involving rearrangement or reaction with interfacial dislocations, Figs. 4.5 to 4.9;
- Creation of a half-loop or a complete loop attached on one side to the particle interface, Figs. 4.5, 4.8, 4.9, 4.14, 4.15, 4.24, 4.25, and 4.28;
- Cross-slip of half-loops away from the particle while pinned on the interface, Figs. 4.14, 4.15, 4.24 and 4.25;
- Annihilation of the half-loop or attached loop by other dislocations, Figs. 4.7 to 4.9;
- Creation of stand-alone loops and debris around the particle from multiple interactions, Figs. 4.7, 4.14, 4.15, 4.24 to 4.27.

It appears that once the particles lose complete coherency, the effect of particle size on dislocation-particle interactions becomes diminished; instead, interfacial structure now plays a dominant role by arbitrating the competition between bypass mechanisms based on density and arrangement of interfacial dislocations, defect structures pinned on the interface…etc. Most likely the presence of half-loops or attached loops on the interface hindered local cross-slip of future dislocation interactions; but with sufficient applied stress combined with the dislocation self-stress, lattice dislocations can approach the interface loops and annihilate them.

There are, however, two types of microstructure seen only in the Cu-Co system: A single loop encircling two or more particles, Fig. 4.15(e)-(f); and shearing of semicoherent

Co particles by twins, Fig. 4.10, 4.16, and 4.29. Twin shear of particles will be discussed in greater detail in Section 5.2.2. Due to the smaller size of Co particles compared with Al_3Sc, a single dislocation frequently interacts with multiple Co particles—and that bowing along the dislocation line can occur simultaneously in neighboring inter-particle regions. As suggested by the *in situ* video frame captures shown in Figs. 4.8 and 4.9(c)-(d), a dislocation segment pinned between two particles (lowest segment of dislocation "3," just below the arrowhead) can bow out to form this configuration. The departure of other dislocation fragments spanning between a particle interface and the foil surface can then account for the type of *post mortem* microstructure shown in Fig. 4.15(e)-(f).

As the coherency of the particle decreases with increasing particle size within the semicoherent regime, the density of interfacial dislocations increases thereby exerting a larger stress field on an incoming dislocation [55, 57]. Linear elasticity theory predicts that above the half-plane, a positive edge dislocation will experience a repulsive force; and below the particle half-plane, an attractive force [54, 112]. Thus when only the mesh size of the interfacial network is varied via loss of coherency, only the kinetics of dislocation-particle interactions is affected—becoming slower due to the increased stress field around the particle—a conclusion which is commensurate with experimental results for Al_3Sc particles measuring 12 nm and 40 nm in size [17].

Although copious indirect evidence exists suggesting that interfacial dislocations can react or self-rearrange when lattice dislocations impinge on the particle interface, direct *in situ* observation of both the interacting lattice dislocation and the interfacial network proved unsuccessful as both thermal and mechanical stimuli induced excessive local foil translation and buckling. The interfacial network for Al_3Sc, however, does appear to be

remarkably stable under electron-beam irradiation: *In situ* electron-irradiation at 200 keV of a semi-coherent Al_3Sc particle produced no discernable rearrangement of the interfacial dislocation network even after more than 1 hr. At elevated temperatures, the dissociation of matrix dislocations in climb has been reported in both experiments as well as computer simulations for creep [15, 101, 113]. And in Cu-1.95%Co and Cu-2.8%Co, coherent precipitates were found to lose coherency, growing larger after dynamic loading whereas incoherent particles exhibited more dislocations tangles after loading [44]. These results, along with those observed in this work, all indicate that accounting for the contribution of the interfacial dislocation network in dislocation-particle interactions will help improve the accuracy of computer models for creep and particle-strengthening systems.

5.1.2 Effect of Particle Anisotropy

Particle size effects for the highly anisotropic Al_2Cu plates were also found to be minor due to geometric considerations. As seen in atomic-resolution images presented in Figs. 4.17 and 4.18, the coherency along the broad side of the particle, $[001]_\theta$, is well-maintained even for a particle of this size. Since the plates lie on habit planes $\{001\}_{Al}$, lattice dislocations impinge along the $\{001\}-\{111\}$ plane intersections, or $\langle 110\rangle_{Al}$. Unlike Al_3Sc or Co particles, however, Al_2Cu plates cannot be bypassed by cross-slip as easily due to the length of the plates (up to nearly 1 μm). Instead, lattice dislocations were observed to accumulate at the particle interface followed by glide in the interfacial plane, Figs. 4.1 and 4.3. These dislocations can then either exit the interface as seen in Fig. 4.4 or continue to slip into the Al matrix, effectively shearing the particle. Previously, only direct

multiple-shearing [114-115] and variants of Orowan looping [116-117] had been reported for platelet particles. In particular, the observed multiple-shearing of {001} θ-plates is in direct contrast to that reported by Russell and Ashby [49], which maintained that no slip penetration of {001} Al_2Cu plates occurred, even when extensive shear loop accumulation took place at the particle interfaces. The current results are, however, consistent with recent molecular dynamics simulations of Ω-plates with {111} habit planes in Al-Cu-Mg-Ag [118], where geometrically-necessary dislocations were generated along the incoherent interface before shearing the particles. This difference in bypass mechanisms between {001}-plates and {111}-plates, along with the observation of a new bypass mechanism involving interfacial glide illustrate the complexity of dislocation interactions with anisotropic particles; and more importantly, demonstrate the importance of accounting for the exact crystallographic orientation of anisotropic particles and interfacial interactions in such particle-strengthening models.

5.2 Influence of Other Factors on Dislocation-Particle Interactions

5.2.1 Role of Deformation History

From time-resolved *in situ* experiments and spatially-resolved electron tomograms, the evolution of the microstructure as successive dislocations interact with a particle, could be deduced. The results highlighted in Chapter 4 demonstrate that as dislocations undergo bypass, a variety of competing mechanisms may operate in concert such as cross-slip, loop pinch-off, and creation/annihilation of half-loops or attached loops. Often, the presence of these dislocation segments or debris in the vicinity of the particle hindered subsequent dislocation interactions. Humphreys and Stewart reported increasing complexity of bypass

processes with increasing strain around SiO_2 particles, with half-loop structures resembling those in Fig. 4.12 and 4.19 at more than 0.2 shear strain [35]. With increasing deformation, alloy systems whose primary particle bypass mode is cross-slip will experience an increased rate of precipitation hardening as dislocation tangles develop in the inter-particle regions.

On the other hand, if the primary mode of bypass is particle cutting, as Li and Wawner reported for Ω-plates, successive passage of dislocations can only occur for a limited number of times due to the buildup of anticoherency dislocations at the interface [114-115, 119]. In contrast, simulation results by Takahashi and Ghoniem reported that each successive cutting of a Cu particle in Fe actually *reduces* its resistance to subsequent shear [120]. Compared with Fig. 4.10(a)-(b), the multiple cutting (not necessarily successive) of Al_2Cu particles appear to be more consistent with Li and Wawner's results. That is, after an Al_2Cu particle is sheared, it becomes more resistant to subsequent shearing along the same slip plane with particle shearing at that location eventually shutting down and an adjacent, parallel slip system activating with the particle becoming sheared at multiple locations. Along with the lack of slip localization, lattice dislocations impinging on the particle interface must re-enter the matrix either by interfacial glide to one end of the particle or by particle-shearing.

5.2.2 Role of Strain Rate

Twinning as a deformation mechanism has a tendency to operate at higher strain rates or low temperatures [25, 121]. Results from *in situ* straining experiments and *post mortem* observation of Co particles in Cu-3Co revealed that small twins can shear these

particles whereas shear by lattice dislocations was never encountered. An existing stacking-fault may have served as the twinning source such that when the twinning stress for Cu, 41~45 mJ m^{-2} [122], was exceeded locally, the twin propagated by glide of at least three $a/6\langle 112\rangle$ partials on consecutive $\{111\}$ planes [121]. Shearing of the octahedral particle can be attributed to the high local stress concentration, during which the twin may have propagated at a velocity greater than 400 m s^{-1} [123]. Since the crystal structure of the Co particle is also face-centered cubic, the increase in surface energy is expected to be less than the shearing of an Al_3Sc particle where an antiphase boundary would be created in the $L1_2$ lattice, consistent with the experimental observation that particle cutting is not favored as a bypass mechanism for Al_3Sc larger than 40 nm.

5.3 Relevance to Creep Model Behavior

Although the dislocation-particle interactions investigated in this work operated at room temperature, a number of key observations can be correlated with those from a previous study for dislocation-Al_3Sc particle interactions operating at elevated temperatures [17]. Some of these include the nucleation of debris at the particle interface, changes in the interfacial contrast during bypass, and the fact that a variety of bypass mechanisms can occur. The net effect of these processes would be a general reduction in the ease of dislocation bypass and multiple mechanisms being active instead of a single prevailing mechanism. In addition, since dislocation-particle interactions were found to evolve over time, it is suggested that the models should include deformation history by introducing defects around particles as a function of time. Whether it is particle-strengthening models

at room temperature or creep models at high temperatures, accounting for the accuracy of physically-based details can prove beneficial by improving their predictive capabilities.

5.4 Development of Diffraction-Contrast Electron Tomography

As outlined in Chapters 2 and 3, the capability to visualize dislocation and defect structures in three dimensions has proven to be a great advantage in facilitating the interpretation of dislocation-particle interactions. This section will briefly reflect on the significance and future potential of diffraction-contrast electron tomography as a materials characterization technique. It is believed that following the initial work on dislocation-particle interactions presented here, electron tomography can be employed to yield new insights in many other types of studies.

5.4.1 Significance for Study of Crystalline Defects

Coupled with conventional analysis techniques such as $\mathbf{g} \cdot \mathbf{b}$ analysis, electron tomography allows for microstructural information like the slip plane and line direction of every dislocation, the contour and degree of bowing along dislocation lines, location of intersecting slip plane with respect to a particle, edge/screw character, and cross-slip events…etc. to be unequivocally determined for a particular volume of interest. For example, the contour of the bowing dislocations around a small θ-particle in Fig. 4.23 would have been difficult to determine without the spatial resolution made possible by tomography. Another example can be found in the cross-slip of attached half-loops "a" and "b" in Fig. 4.25—where the cross-slipping is only apparent when both slip planes are viewed edge-on, at a vantage point nearly parallel to the foil surface—which would have

been physically impossible for conventional micrographs.

The implications for any study involving crystalline defects are enormous; never before has such a wealth of information been available from a single sample volume, typically represented by just a single micrograph. In addition, the level of detailed spatial knowledge also allows for direct and meaningful comparisons between experimental and computer simulation results. For instance, dislocation dynamics simulations by Xiang et al. reported a dependence of the bypass of a hard particle by an edge dislocation on where the slip plane intersects the particle [54]. For a dislocation gliding on a slip plane just above the particle center at h = 0.1R, where R is the particle radius, the bypass occurs by a process similar to Orowan looping. At slip plane intersection half way between the top and the center of the particle, h = 0.5R, however, a combined cross-slip and pinch-off of two non-glide loops takes place. Whereas from a conventional micrograph the exact location of a slip plane with respect to the particle would be ambiguous, in a reconstructed tomogram the same information is straightforward to determine.

Furthermore, prior knowledge about dislocations as well as image contrast theory can be used to complete the information lost by not sampling all of Fourier space to produce a dislocation model in spite of the missing wedge. Consequently, fewer images are needed to enable the construction of a dislocation model. The real benefit of electron tomography is the ability to produce an exact dislocation model of a volume by 3D tracing. This is a novel capability which has been demonstrated for the first time during the course of this study, producing a colored high-density information display of the volume of interest. Additional benefits include that dislocations of different character and/or Burgers vector can be coded with different colors to enhance visually reactions between dislocations

and other obstacles. Other features such as the embedding of a crystal coordinate system or slip planes and 3D labels…etc. all contribute to bring about a much more visual representation of the volume information with unprecedented clarity. These advances provide an opportunity to better understand and represent complex reactions.

5.4.2 Future Developments in Electron Tomography

While diffraction-contrast electron tomography has undoubtedly proven its usefulness, it remains at present a technique that is demanding in terms of the time and number of images required. And although its use in a number of studies is just now gaining recognition, a goal of this effort lies in improving its accessibility so that electron tomography may become a routine investigative tool for material scientists. To that end, several recent and on-going developments with future potential will be mentioned here. One of these involves reducing the time expenditure by fully- or semi- automating the acquisition of the tilt series. The first such endeavor by Dierksen and Typke involved electron microscope controls and automatic image recording [124]. That basic premise remains unchanged in today's microscopy software written to work in conjunction with transmission electron microscopes and CCD cameras. For example, SerialEM [125] has automated functions to tilt, search (correcting sample displacement incurred by tilting), focus (using goniometer Z-height and objective lens focus), and record tilt series images.

Two other developments are the fiducial method, for lowering the number of images when reconstructing straight dislocations lines [126]; and dual-axes tomography for eliminating the $\mathbf{g} \cdot \mathbf{b}$ invisibility of dislocations and improving the tomogram fidelity [85, 87]. These efforts all contribute to the eventual objective of 4D tomography—namely

granting the microscopist the ability to follow the evolution of the microstructure in *space and time* by taking 3D "snapshots" of the volume while the sample is subjected to interrupted *in situ* stimuli. Then it will be possible to link the before and after microstructures, say, in the Al-Cu system (Fig. 4.20 and Fig. 4.22), with *in situ* time-resolved information. Undeniably, there still remain many technical challenges before the potential for diffraction-contrast electron tomography is fully explored; but future developments look certain to yield new insights and improved understanding for a variety of materials processes.

CHAPTER 6

CONCLUSIONS

In situ straining experiments, *post mortem* analyses, and electron tomographic reconstructions have been used to investigate the deformation behavior of three alloy systems, Al-Cu containing Al_2Cu plates, Al-Mg-Sc containing Al_3Sc spherical particles, and Cu-Co containing Co-rich octahedral particles as a function of particle size and geometry, particle-matrix interface coherency, and deformation history and strain rate. In addition, capabilities of diffraction-contrast electron tomography were developed as a 3D imaging technique for transmission electron microscopy. Key conclusions include:

Dislocation-particle interactions

- Dislocation-particle interactions for Al_3Sc and Co particles are influenced by the particle-matrix interface coherency. For coherent particles, less than 40 nm in size, particle shearing by lattice dislocations occurs; but for semi-coherent particles, up to around 200 nm for Al_3Sc and 100 nm for Co, an initial elastic interaction occurred as a result of differences in the shear moduli, lattice parameters, and Poisson's ratios between the precipitate phases and the matrix.
- Dislocation interactions with semi-coherent Al_3Sc and Co particles involved reactions with interfacial dislocations which increased the complexity of the particle-matrix interface that can hinder subsequent bypass of the particles.
- As a part of dislocation bypass of semi-coherent Al_3Sc and Co particles, half- and complete loops attached on one side to the particle interface were created through

cross-slip and bowing around the particle. These looped structures can break away from their pinning locations on the particle interface via cross-slip or be annihilated by other lattice dislocations.

- Stand-alone loops and debris can be generated around one particle as a result of multiple interactions with lattice dislocations resulting in an evolution of the defect structures around the particles over time. The dislocation-particle interactions studied were much more complex than single dislocation-single particle interactions depicted in classical theoretical models.
- Al_2Cu platelet particles were anisotropic in shape and interface coherency—being highly coherent along the broad side but incoherent along the narrow side. With sufficient applied stress, lattice dislocations entered and were glissile in the $\{001\}_{Al}$ particle-matrix interface until they either exit the interface via cross-slip at one end of the plates or slip into the Al matrix, shearing the particle.
- Semi-coherent Co particles larger than the predicted transition radius between particle shearing and Orowan looping were sheared by twins but not by lattice dislocations. This was thought to be due to the high strain rate of deformation associated with twinning and a smaller increase in interfacial energy associated with shearing of Co particles, which has the same stacking order as the Cu matrix.

Electron tomography

- Diffraction-contrast micrographs were acquired over a large angular range and used to reconstruct tomograms, or a representation of the imaged sample volume, that recovered the lost information in the through-thickness direction. The tomograms

enabled viewing of defect structures from any vantage point.

- Accurate dislocation models of the sample volume were produced by 3D tracing of the tomographic reconstructions. Dislocations of different character or Burgers vector could be color coded for enhanced visualization and clarity of the spatial arrangement and reactions between dislocations and other obstacles.
- A method to define the specimen crystal coordinate system inside a reconstructed tomogram was developed which permitted the identification of slip planes, line directions, dislocation character and occurrence of cross-slip.
- The $\mathbf{g} \cdot \mathbf{b}$ invisibility condition was overcome by using dual-axes tomography in which an additional tilt series imaged under a different diffraction vector was acquired. The results of both tilt series were incorporated together such that all the defect structures were represented in the tomogram.
- By using prior knowledge about dislocations and image contrast theory, the effects of the missing wedge, or incomplete sampling of the sample Fourier space, could be mitigated. This effort facilitated the production of dislocation models using fewer tilt series images.

These observations regarding dislocation-particle interactions in the Al-Cu, Al-Mg-Sc, and Cu-Co alloys provide new insight into the operating mechanisms during room temperature bypass of second-phase particles. They were made possible through the development of diffraction-contrast electron tomography and have implications for creating accurate predictive computer models for particle-strengthening systems.

References

[1] W.F. Smith, Structure and Properties of Engineering Alloys, Second ed., McGraw-Hill, Inc., 1993.
[2] alumatter, http://www.alumatter.info/, Physical Properties, 2011.
[3] Z. Ahmad. The properties and application of scadium-reinforced aluminum. JOM, 55 (2003) 35-39.
[4] Z. Ahmad, B.J. Abdul Aleem. Effect of nano Al($Sc_{x-1}Zr_x$) precipitates on the mechanical and corrosion behavior of Al-2.5 Mg alloys. Mater. Corros., 62 (2011) 335-345.
[5] D. Hull, D.J. Bacon, Introduction to Dislocations, 4th ed., Butterworth-Heinemann, 2001.
[6] G.E. Dieter, Mechanical Metallurgy, 2nd ed., McGraw-Hill Book Company, 1976.
[7] T.H. Courtney, Mechanical behavior of materials, 2nd ed., McGraw Hill, 2000.
[8] L. Zang, http://www.eng.utah.edu/~lzang/, The Zang Research Group, 2011.
[9] MATTER University of Liverpool, http://www.matter.org.uk/, glossary, 2011.
[10] J. Wang, R.G. Hoagland, A. Misra. Room-temperature dislocation climb in metallic interfaces. Appl. Phys. Lett., 94 (2009) 1910-1912.
[11] N. Li, J. Wang, J.Y. Huang, A. Misra, X. Zhang. In situ TEM observations of room temperature dislocation climb at interfaces in nanolayered Al/Nb composites. Scripta Mater., 63 (2010) 363-366.
[12] J.S. Koehler. On the dislocation theory of plastic deformation. Phys. Rev., 60 (1941).
[13] J.E. Dorn, Creep and Recovery, American Society for Metals, 1957.
[14] E. Arzt, D.S. Wilkinson. Threshold stresses for dislocation climb over hard particles: the effect of an atractive interaction. Acta Metall., 34 (1986) 1893-1898.
[15] R.S. Mishra, T.K. Nandy, G.W. Greenwood. The threshold stress for creep controlled by dislocation-particle interaction. Philos. Mag. A., 69 (1994) 1097-1109.
[16] E.A. Marquis, D.C. Dunand. Model for creep threshold stress in precipitation-strengthened alloys with coherent particles. Scripta Mater., 47 (2002) 503-508.
[17] B.G. Clark, Dislocation-obstacle interactions in aluminum alloys, Ph. D Thesis, Unversity of Illinois at Urbana-Champaign, 2006.
[18] K. Ihara, Y. Miura. Dynamic recrystallization in Al-Mg-Sc alloys. Mater. Sci. Eng. A, (2004).
[19] J. Courbon, F. Louchet. On the mechanisms of formation of superlattice stacking faults in $L1_2$ precipitates embedded in a FCC matrix. phys. Stat. Sol. (a), 137 (1993) 417.
[20] B. Decamps, A.J. Morton, M. Condat. On the mechanism of shear of g' precipiatates by single (a/2)<110> dissociated matrix dislocations in Ni-based superalloys. Philos. Mag. A., 64 (1991) 641-668.
[21] B. Decamps, J.-M. Penisson, M. Condat, L. Guetaz, A.J. Morton. Lattice imaging of dislocations at the g/g' interface in deformed Ni-based superalloys. Mater. Sci. Forum, 189-190 (1995) 261-266.
[22] N.F. Mott, F.R.N. Nabarro. An attempt to estimate the degree of precipitation hardening, with a simple model. Proc. Phys. Soc., 52 (1940) 86-90.

[23] N.F. Mott, F.R.N. Nabarro, Proceedings of the Physical Society of London, Conference on the Strength of Solids, London, 1948, pp. 1.
[24] E. Orowan, Symposium on Internal Stresses in Metals and Alloys, Symposium on Internal Stresses in Metals and Alloys, Inst. Met. London, London, 1948, pp. 451.
[25] J.P. Hirth, J. Lothe, Theory of Dislocations, 2nd ed., Krieger Publishing Company, 1982.
[26] M.F. Ashby. The deformation of plastically non-homogeneous materials. Philos. Mag., 21 (1970) 399-424.
[27] N.S. Stoloff, Fundamentals of strengthening, John Wiky & Sons, 1987.
[28] M.F. Ashby, On the Orowan stress, MIT Press, 1969.
[29] F.J. Humphreys, P.B. Hirsch. The deformation of single crystals of copper and copper-zinc alloys containing alumina particles. II. Microstructure and dislocation-particles interactions. Proc. R. Soc. London, Ser. A, 318 (1970) 73.
[30] P.B. Hirsch. J. Inst. Met., 86 (1957).
[31] P.B. Hirsch, F.J. Humphreys. The deformation of single crystals of copper and co. Proc. Roy. Soc. Lond., A318 (1970) 45-72.
[32] A.J.E. Foreman, P.B. Hirsch, F.J. Humphreys, Movement of a dislocation through random arrays of point and parallel line obstacles, Conference on Fundamental Aspects of Dislocation Theory, Washington, D.C., 1970, pp. 1083-1098.
[33] L.M. Brown, G.R. Woolhouse. The loss of coherency of precipitates and the generation of dislocations. Philos. Mag., 21 (1970) 329-345.
[34] F.J. Humphreys, Dislocation-particle interactions, Dislocations and properties of real materials, Inst. Metals, London, 1984.
[35] F.J. Humphreys, A.T. Stewart. Dislocation generation at SiO_2 particles in an a-brass matrix on plastic deformation. Surf. Sci., 31 (1972) 389-421.
[36] D.B. Williams, C.B. Carter, Transmission Electron Microscopy: A Textbook for Materials Science, Plenum Press, 1996.
[37] J.D. Eshelby. The determination of the elastic field of an ellipsoidal inclusion, and related problems. Proc. Royal Soc. London Series A, 241 (1957).
[38] V.A. Phillips, J.D. Livingston. Direct observation of coherency strains in a copper-cobolt alloy. Philos. Mag., 7 (1962) 969-980.
[39] A. Kelly, R.B. Nicholson. Precipitation hardening. Prog Mater Sci, 10 (1963) 149-391.
[40] G. Thomas, V.F. Zackay, E.R. Parker, Structure and high-strength metals, Sagamore Army Materials Research Conference, 1965, pp. 3-39.
[41] M.F. Ashby. Work hardening of dispersion-hardened cyrstals. Philos. Mag., 14 (1966) 1157-1178.
[42] D. Vaughan, J.M. Silcock. The orientation and shape of q precipitates formed in an Al-Cu alloy. Phys. Stat. Sol. (b), 20 (1967) 725-736.
[43] D.J.H. Cockayne. Investigations of dislocation strain fields using weak beams. Philos Mag, 20 (1969) 1265-1270.
[44] K.V. Rao, D.H. Polonis. Microstructural damage due to dynamic loading of Cu-Co dispersion alloys. J. Mater. Sci., 20 (1985) 491-500.
[45] N. Thompson. Dislocation nodes in face-centred cubic lattices. Proc. Phys. Soc. B, 66 (1953) 481-492.
[46] C.W. Allen, In situ electron microscopy techniques, Marcel Dekker, Inc., 2004.

[47] P.B. Hirsch, R.W. Horne, M.J. Whelan. Direct observations of arrangement and motion of dislocations in aluminium. Philos. Mag., 1 (1956) 677-684.
[48] D.W. Pashley, A.E.B. Presland. Ion damage to metal films inside an electron microscope. Philos. Mag., 6 (1961) 1003-1012.
[49] K.C. Russell, M.F. Ashby. Slip in aluminum crystals containing strong, plate-like particles. Acta Metall., 18 (1970) 891-901.
[50] G.S. Liu, I.M. Robertson. Three-dimensional visualization of dislocation-precipitate interactions in a Al-4Mg-0.3Sc alloy using weak-beam dark-field electron tomography. J. Mater. Res., 26 (2011) 514-522.
[51] P. Donnadieu, G.F. Dirras, J. Douin. An approach of precipitate/dislocation interaction in age-hardened Al-Mg-Si alloys: measurement of the strain field around precipitates and related simulation of the dislocation propagation. Aluminum Alloys 2002: Their Physical and Mechanical Properties Pts 1-3, 396-4 (2002) 1019-1024.
[52] D. Baither, V. Mohles, E. Nembach. In situ transmission electron microscopy tensile tests of a peak- to overaged γ'-strengthend nickel base alloy. J. Mater. Res., 20 (2005) 1722-1727.
[53] Y. Brechet, F. Louchet. On the stability of Orowan loops around coherent spherical ordered precipitates. Acta Metall., 37 (1989) 2469-2473.
[54] Y. Xiang, D.J. Srolovitz, L.-T. Cheng, W. E. Level set simulations of dislocation-particle bypass mechanisms. Acta Mater., 52 (2004).
[55] K. Yashiro, F. Kurose, Y. Nakashima, K. Kubo, Y. Tomita, H.M. Zbib. Discrete dislocation dynamics simulation of cutting of γ' precipitate and interfacial dislocation network in Ni-based superalloys. Intern. J. Plasticity, 22 (2006) 713-723.
[56] T. Harry, D.J. Bacon. Computer simulation of the core structure of the < 111 > screw dislocation in alpha-iron containing copper precipitates: II. dislocation-precipitate interaction and the strengthening effect. Acta Mater, 50 (2002) 209-222.
[57] K. Yashiro, Y. Nakashima, Y. Tomita. Discrete dislocation dynamics simulation of interfacial dislocation network in gamma/gamma-prime microstructure of Ni-based superalloys. CMES, 1 (2005).
[58] L.M. Brown, W.M. Stobbs. The work-hardening of copper-silica 1. Philos. Mag., 23 (1971) 1185-1199.
[59] L.M. Brown, W.M. Stobbs. The work-hardening of copper-silica 2. Philos. Mag., 23 (1971) 1201-1233.
[60] T. Hatano. Dynamics of a dislocation bypassing an impenetrable precipitate: The Hirsch mechnism revisited. Phys. Rev. B, 74 (2006).
[61] T. Tsuru, Y. Shibutani. Formation and critical shear stresses of prismatic dislocation loops observed around spherical precipitate in single crystalline aluminum and copper matrices. Jpn. Soc. Mech. Eng., 71 (2005) 25-30.
[62] T. Tsuru, Y. Shibutani. Initial yield process around a spherical inclusion in single-crystalline aluminium. J. Phys. D: Appl. Phys., 40 (2007) 2183-2188.
[63] Z.S. Basinski. Stereo-Electron Micrography of Dislocation Networks. Proc. Int. Conf. Electron Microsc., (1962).
[64] J. Frank, Electron Tomography: Methods for Three-Dimensional Visualization of Structures in the Cell, 2nd ed., Springer, 2005.

[65] B.F. McEwen, M. Marko. The emergence of electron tomography as an important tool for investigating cellular ultrastructure. J. Histochem. Cytochem., 49 (2001) 553.
[66] B.F. McEwen, C. Renken, M. Marko, C. Mannella, J.C. John, I. W. Detrich. Principles and practice in electron tomography. Methods Cell Biol., 89 (2008) 129.
[67] R.A. Crowther, D.J. DeRosier, A. Klug. The reconstruction of a three-dimensional structure from projections and its application to electron microscopy. Proc. R. Soc. Lond. A, 317 (1970) 319-340.
[68] M. Radermacher. Three-dimensional reconstruction of single particles from random and nonrandom tilt series. J. Electron Microsc. Tech., 9 (1988) 359-394.
[69] P.A. Midgley, M. Weyland. 3D electron microscopy in the physical sciences: the develoopment of Z-contrast and EFTEM tomography. Ultramicroscopy, 96 (2003).
[70] JEOL USA, http://www.jeol.com/Default.aspx?tabid=93, Electron optics, 2011.
[71] V.K. Lindroos. Knitting of a dislocation network with selective interaction. Philos. Mag., 24 (1971) 709-712.
[72] J.W. Edington, Practical electron microscopy in materials science, Techbooks, 1976.
[73] P.B. Hirsch, A. Howie, R.B. Nicholson, D.W. Pashley, M.J. Whelan, Electron microscopy of thin crystals, 2nd Revised ed., Krieger Publishing Company, 1977.
[74] M. Weyland, P.A. Midgley, R. Brydson, A.R. Lupini, S.N. Rashkeev, M. Varela, A.Y. Borisevich, M.P. Oxley, K.v. Benthem, Y. Peng, N.d. Jonge, G.M. Veith, S.T. Pantelides, M.F. Chisholm, S.J. Pennycook, R.E. Dunin-Borkowski, T. Kasama, R.J. Harrison, D.J. Smith, P.L. Gai, M.R. Castell, Nanocharacterization, RSC Publishing, 2007.
[75] M. Raman, C. Koch-Stoschek, D. Yip, D. Ress, M. Harlow, R. Marshall, J. Xu, J. Szule, U.J. McMahan, EM3D ver. 2.0, Software for Electron Microscope Tomography, 2007.
[76] W.S. Rasband, ImageJ ver. 1.44, U.S. National Institutes of Health, Bethesda, Maryland, USA, 1997-2008.
[77] M.D. Abramoff, P.J. Magelhaes, S.J. Ram. Image processing with ImageJ. Biophotonics Int., 11 (2004) 36-42.
[78] C. Messaoudi, T. Boudier, C.O. Sanchez Sorzano, S. Marco, TomoJ ver. 2.11, Tomography software for three-dimensional reconstruction in transmission electron microscopy, Universite Pierre & Marie Curie, 2007.
[79] D.J.H. Cockayne. Weak-beam electron microscopy. Ann. Rev. Mater. Sci., 11 (1981) 75-95.
[80] I.L.F. Ray, D.J.H. Cockayne. The observation of dissociated dislocations in silicon. Philos Mag, 22 (1970) 853-856.
[81] E.F. Pettersen, T.D. Goddard, C.C. Huang, G.S. Couch, D.M. Greenblatt, E.C. Meng, T.E. Ferrin. UCSF Chimera--a visualization system for exploratory research and analysis. J. Comput. Chem., 25 (2004) 1605-1612.
[82] T.E. Ferrin, C.C. Huang, G.S. Couch, E.F. Pettersen, T.D. Goddard, E.C. Meng, D.M. Greenblatt, D. Konerding, G. Pintilie, W. Zhang, T. Lang, S. Schreiber, B. Morris, T. Margraf, UCSF Chimera ver. 1.5.3, An extensible molecular modeling system, 2004-11.
[83] T.D. Goddard, C.C. Huang, T.E. Ferrin. Software extensions to UCSF Chimera for interactive visualization of large molecular assemblies. Structure, 13 (2005) 473-482.

[84] M. Tanaka, S. Sadamatsu, G.S. Liu, H. Nakamura, H. Higashida, I.M. Robertson. Sequential multiplication of dislocation sources along a crack front revealed by HVEM-tomography. J. Mater. Res., 26 (2011) 508-513.
[85] D.N. Mastronarde. Dual-axis tomography: an approach with alignment methods that preserve resolution. J. Struct. Bio., 120 (1997) 343-352.
[86] I. Arslan, J.R. Tong, P.A. Midgley. Reducing the missing wedge: High-resolution dual axis tomography of inorganic materials. Ultramicroscopy, 106 (2006) 994-1000.
[87] P. Penczek, M. Marko, K. Buttle, J. Frank. Double-tilt electron tomography. Ultramicroscopy, 60 (1995) 393-410.
[88] Gatan Inc., http://www.gatan.com/products/specimen_holders/, Gatan, Inc. products, 2011.
[89] J.M. Howe, W.E. Benson, A. Garg, Y.C. Chang. In Situ Hot-Stage High-Resolution Transmission Electron Microscopy of Interface Dynamics during Growth and Dissolution of $\{111\}_a$ q-Al_2Cu Plates in an Al-Cu-Mg-Ag Alloy. Mat. Sci. Forum, 189-190 (1995) 255-260.
[90] K.M. Knowles, W.M. Stobbs. The structure of {111} age-hardening precipitates in Al-Cu-Mg-Ag alloys. Acta Cryst., B44 (1988) 207-227.
[91] B.C. Muddle, I.J. Polmear. The precipitate W phase in Al-Cu-Mg-Ag alloys. Acta Metall., 37 (1989) 777-789.
[92] Y.C. Chang, J.M. Howe. In-Situ HRTEM Study of Omega-Precipitate Dissolution in an Al-Cu-Mg-Ag Alloy. Ultramicroscopy, 51 (1993) 46-63.
[93] W.E. Benson, J.M. Howe. An in-situ high-resolution transmission electron microscoy study of the growth and dissolution of $q_{\{111\}}$ precipitate plates in an Al-Cu-Mg-Ag alloy. Philos. Mag. A., 75 (1997) 1641-1663.
[94] M. Takeda, N. Suzuki, G. Shinohara, T. Endo, J.V. Landuyt. TEM study on precipitation behavior in Cu-Co alloys. Phys. Stat. Sol. (a), 168 (1998).
[95] M. Takeda, H. Yamada, Y. Yoshida, K. Shimasue, T. Endo, J.V. Landuyt. TEM study and Monte-Carlo simulation of nano-scale Co particles precipitated in a Cu matrix. Phys. Stat. Sol. (a), 198 (2003) 436-442.
[96] A. Garcıa Prieto, M.L. Fdez-Gubieda, C. Meneghini, A. Garcıa-Arribas. In situ observation of the structural changes induced by thermal annealing on melt-spun Co15Cu85 granular alloys. J. Magn. Magn. Mater, 254-255 (2003) 82-84.
[97] J.H. Shim, D.I. Kim, W.S. Jung, Y.W. Cho, B.D. Wirth. Atomistic modeling of nanosized Cr precipitate contribution to hardening in an Fe-Cr alloy. J Nucl Mater, 386 (2009) 56-59.
[98] D.C. Chrzan, J.W. Morris, Y.N. Osetsky, R.E. Stoller, S.J. Zinkle. What is the Limit of Nanoparticle Strengthening? Mrs Bull, 34 (2009) 173-177.
[99] A.J. Wang, R.S. Kumar, M.M. Shenoy, D.L. McDowell. Microstructure-based multiscale constitutive modeling of gamma-gamma ' nickel-base superalloys. Int J Multiscale Com, 4 (2006) 663-692.
[100] C.S. Shin, M.C. Fivel, M. Verdier, K.H. Oh. Dislocation-impenetrable precipitate interaction: a three-dimensional discrete dislocation dynamics analysis. Philos Mag, 83 (2003) 3691-3704.
[101] D.J. Bacon, Y.N. Osetsky, D. Rodney. Chapter 88 dislocation-obstacle interactions at the atomic level. Dislocations in Solids, 15 (2009) 1-90.

[102] I.M. Robertson. Microtwin formation in deformed nickel. Philos. Mag. A., 54 (1986) 821-835.
[103] W.J. Tunstall, P.J. Goodhew. Electron microscope image contrast of double loops in quenched aluminium. Philos. Mag., 13 (1966) 1259-1272.
[104] M. Ignat, F. Durand. Deformation lines on Al_2Cu single crystals after creep in compression. Scripta Metall., 10 (1976) 623-626.
[105] R. Bonnet, M. Loubradou. Crystalline defects in a B.C.T. Al2Cu(q) single crystal obtained by unidirectional solidification along [001]. Phys. Stat. Sol. (a), 194 (2002) 173-191.
[106] H.P. Karnthaler. The study of glide on {001} planes in f.c.c. metals deformed at room temperature. philos. Mag. A., 38 (1978) 141-156.
[107] A. Korner, H.P. Karnthaler. Weak-beam studies of composite dislocations and dislocations gliding on (001) planes in silver. Philos. Mag. A., 44 (1981) 275-284.
[108] P. Guyot. Hardening by ordered coherent precipitates related to the statistical theory. Philos. Mag., 24 (1971) 987-993.
[109] T. Ericsson. The temperature and concentration dependence of the stacking fault energy in the Co-Ni system Acta Metall., 14 (1966) 853-865.
[110] High Rate Deformation Group, http://hrdg.matse.illinois.edu/hopbar.html, Split-Hopkinson Pressure Bar Testing, 2011.
[111] Y. Matsukawa, G.S. Liu, Unpublished work, University of Illinois at Urbana-Champaign, 2009.
[112] D.J. Srolovitz, R.A. Petkovic-Luton, M.J. Luton. Diffusional relaxation of the dislocation-inclusion repulsion. Philos. Mag. A., 48 (1983) 795-809.
[113] S.M. Zhu, S.C. Tjong. Dislocation/particle interactions in b'(NiAl) precipitation strengthened ferritic Fe-19Cr-4Ni-2Al alloy. Metall. Mater. Trans. A, 28A (1997).
[114] B.Q. Li, F.E. Wawner. Dislocation interaction with semicoherent precipitates (Omega phase) in deformed Al-Cu-Mg-Ag alloy. Acta Mater, 46 (1998) 5483-5490.
[115] B.Q. Li, F.E. Wawner. Observation of dislocation multiple cutting of the semicoherent precipitate in Al-Cu-Mg-Ag alloy. Aluminium Alloys: Their Physical and Mechanical Properties, Pts 1-3, 331-3 (2000) 1359-1364.
[116] B. Noble, S.J. Harris, K. Dinsdale. Yield characteristics of aluminium-lithium alloys. Met. Sci., 16 (1982) 425-430.
[117] J.T.M.d. Hosson, A.J. Huis In't Veld, H. Tamler, O. Kanert. Dislocation dynamics in Al-Li alloys. mean jump distance and activation length of moving dislocations. Acta Metall., 32 (1984) 1205-1215.
[118] K. Elkhodary, W. Lee, L.P. Sun, D.W. Brenner, M.A. Zikry. Deformation mechanisms of an W precipitate in a high-strength aluminum alloy subjected to high strain rates. J. Mater. Res., 26 (2011) 487-497.
[119] B.Q. Li, F.E. Wawner. Observation of dislocation cutting Omega phase and its strengthening mechanism in an Al-Cu-Mg-Ag alloy. Microsc Microanal, 3 (1997) 139-145.
[120] A. Takahashi, N.M. Ghoniem. A computational method for dislocation-precipitate interaction. J. Mech. Phys. Solids, 56 (2008).
[121] S. Mahajan, G.Y. Chin. Formation of deformation twins in F.C.C. crystals. Acta Metall., 21 (1973) 1353-1363.

[122] S. Kibey, J.B. Liu, D.D. Johnson, H. Sehitoglu. Predicting twinning stress in fcc metals: linking twin-energy pathways to twin nucleation. Acta Mater., 55 (2007) 6843-6851.
[123] J. Marian, W. Cai, V.V. Bulatov. Dynamic transitions from smooth to rough to twinning in dislocation motion. Nat. Mater., 3 (2004) 158-163.
[124] K. Dierksen, D. Typke, R. Hegerl, A.J. Koster, W. Baumeister. Towards automatic electron tomography. Ultramicroscopy, 40 (1992) 71-87.
[125] D.N. Mastronarde. Automated electron microscope tomography using robust prediction of specimen movements. J. Struct. Bio., 152 (2005) 36-51.
[126] J.P. Kacher, G.S. Liu, I.M. Robertson. Visualization of grain boundary/dislocation interactions using tomographic reconstructions. Scripta Mater., 64 (2011) 677-680.

APPENDIX A

INSTRUCTIONS FOR USING THE TILT-ROTATE STAGE

The tilt-rotate stage is a single-tilt stage with sample-plane rotation controlled via two "chopsticks" and is compatible with JEOL TEMs. It is capable of -60^{o} to $+60^{o}$ tilt, making a total of 120^{o} theoretical tilt range. For this reason, it is especially useful in experiments requiring large tilts, e.g. electron tomography. The stage needs to be connected with a computer installed with the LabView (ver. 8.2 or higher) software as well as the custom program "Read AD7746 Capacitance" along with the Kleindiek control box and the TEM via several cables. The sample needs to be 2.3 mm in diameter and is fixed to a "puck" that rests between the chopsticks. As the stage rod interior is hollow, it is highly recommended that the stage is pre-pumped prior to the actual TEM session.

This document is divided into four sections as follows:

A.1 Hardware Overview

The tilt-rotate stage is composed of a standard-dimension rod with motor-driven chopsticks at the tip. The sample is held by a ring-shaped puck fixed between the chopsticks, which are controlled independently (forward on right stick and backward on left stick for clockwise rotation of sample) via knobs "B" and "C" on the Kleidiek control box. "B" knob controls right motor and "C" knob controls the left motor.

A.2 Sample Loading/Unloading

Sample dimension is 2.3mm diameter disc with thickness 100 to 150 μm. After punching the discs out, be sure to polish away the burrs as they can make it difficult to fit the sample into the puck, or make the sample in a slanted fashion.

You may find it easier to perform the following under an optical microscope: After adjusting the position of the sample to align the tilt-axis with the hole (if visible), fix it by carefully applying carbon paste on the thick side portions. Now use flat-ended tweezers to place the puck in between the chopsticks.

Hook up all the connecting cables between the computer (control software), control box and the stage, see Section III below. Make the encoders go to zero values on the computer by turning B and C knobs on control box, then verify the puck is in the "**ZERO-position**" (i.e. the distance between the yellow plastic end cap and the center of the puck is **22.5 mm**) by using a micrometer. If not, move gently with tweezers.

Now retract the chopsticks into the "**BACK-position**" (i.e. the distance between the yellow plastic cap and the tips of chopsticks is **< 27.5 mm**) by turning the B and C knobs clockwise until the capacitance reads +2.5 pF. This is necessary so the tips of chopsticks will be far away from the pumping valve when the stage is first inserted into the TEM.

Pre-pump stage by inserting the plastic cover sleeve to just over the last o-ring then engage roughing/diffusion pumps of vacuum storage system as posted. It takes several hours for carbon paste to dry properly.

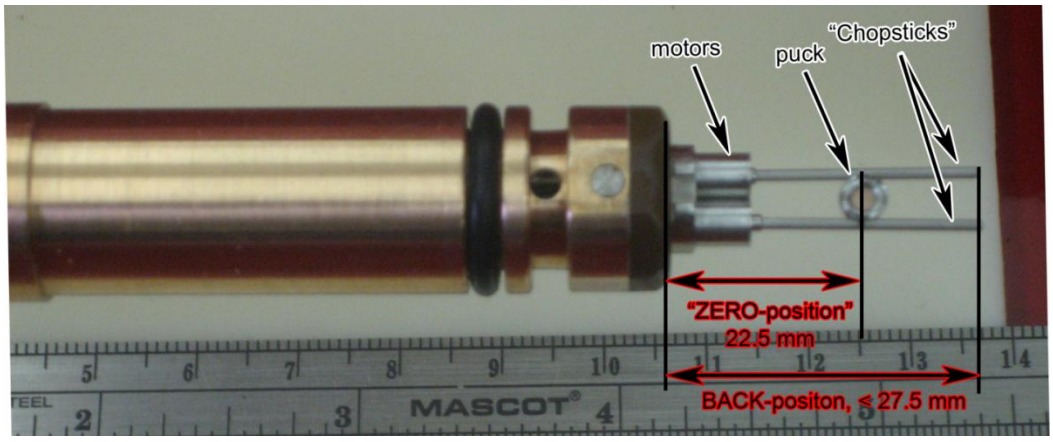

A.3 Connecting Cables

A number of cables link the hardware components together: Kleidiek control box, stage, TEM goniometer, and the computer. Plug in the power cables after ①-⑤ below have been attached. The cables are labeled with matching numbers as follows:

① Kleidiek control box to stage
② USB COM2 (default) to computer for capacitance data transfer
③ USB motor control to Kleidiek control box
④ "OUT" port on Kleidiek control box to motors
⑤ grounding wire (black side), attach yellow clamp to goniometer (grounds TEM).

When all connections have been made, turn on Kleidiek control box via power switch on left back side. The program sets the USB port for capacitance data as COM2—if the software doesn't respond or an error message indicating the software is unable to find correct connector at COM2, close program and reconnect cable ② to another port then open program to try again.

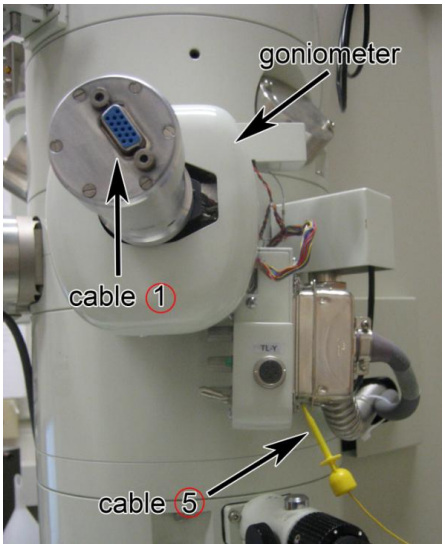

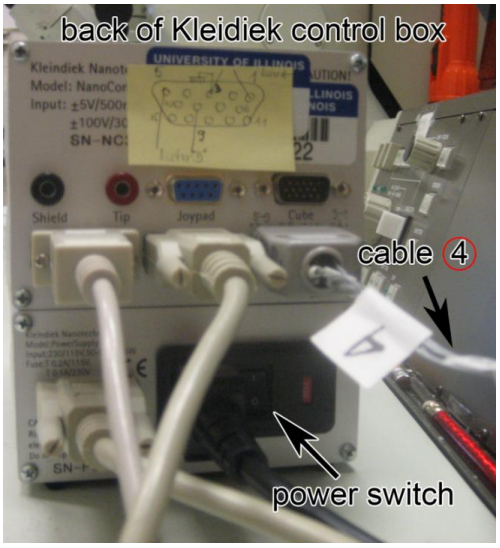

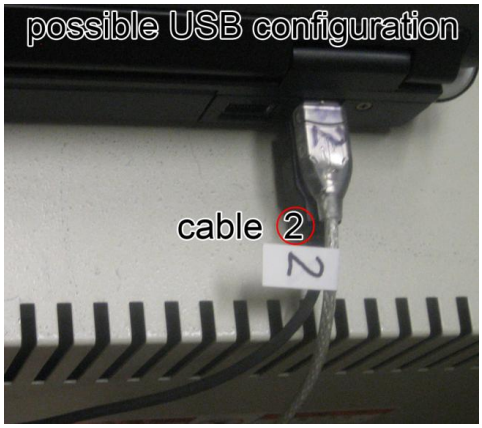

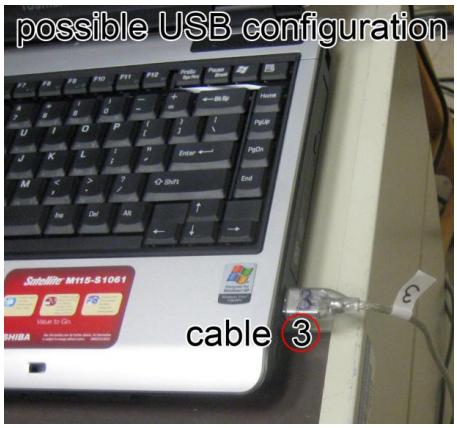

A.4 Running Software and Data Acquisition

Run position-capacitance measurement program "Read AD7746 Capacitance." When all the cables are connected (see Section III), run program. If something is not connected correctly (default for serial/USB port is COM2), check the drop-down menu, 1, and try other ports. Rearrange the connections as needed.

Press **Start** button, 2. Two curves will appear, showing the capacitance of each motor. They are used to designate the position of chopsticks. The red curve corresponds to the right motor; and the green curve to the left motor. You can change between constant range display and automatically-scaled mode (as the curve moves, the range display scales to keep the curve within the viewing area) by pressing 3 (**Capacitance**). The same applies for the **Data point** plotted on the x-axis by pressing 4. Note that x=0 is fixed. Under 5 there are more display options (zooming, scaling, graph scrolling) for ease of data collection. The most important reading is the capacitance values for the left and right motors in pF, 6, where 0.001 pF corresponds approximately to 1 μm of movement.

Once **Start** has been pressed (2), the button changes to read **Stop**. Data collection can be stopped by pressing this button to save computer memory while you move the chopsticks. Press **Start** again to get correct reading afterwards. If past readings are no longer needed, the graph display can be cleared by pressing 7 without closing the program. On the left hand side you can change the **Measurement time** and **pts for averaging** to adjust for the optimal graphical display. Short time/low number of pts = noisy but fast; long time/high number of pts = smooth but slow. Default settings are good enough generally.

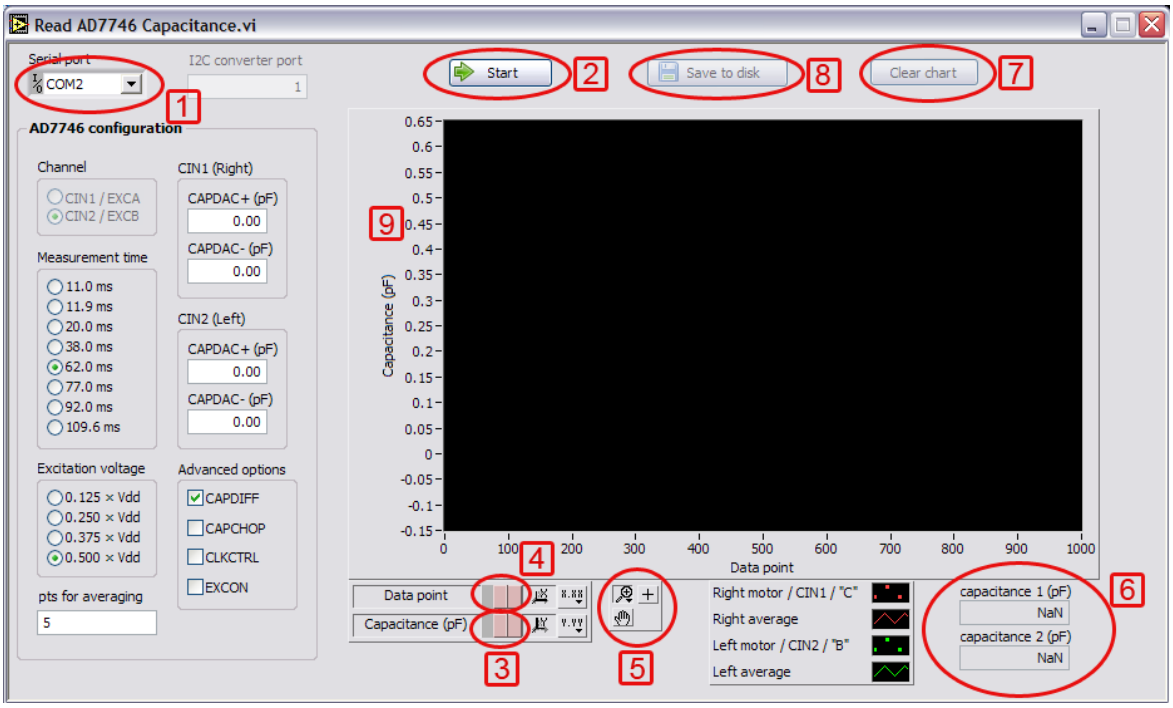

Important things to remember:

1. Forward moving of chopsticks correspond to clockwise turning of knobs (B is right motor and C is left motor).
2. Back position is capacitance +2.5 to +3 (< 27.5 mm from yellow plastic cap to end of chopsticks). This is extremely important for loading the stage. DO NOT move motors more than + or -3 pF.
3. Zero-position = 22.5 mm from yellow plastic cap to center of puck. This is the position directly under the beam. Calibrate zero-position by making encoders go to zero values by turning B and C knobs, then physically move puck to the zero-position.